2-3-2014

Solution Processed Semiconductor Nanostructures and Nanocomposites for Dye Sensitized Solar Cells

Venkata Manthina
University of Connecticut - Storrs, venkata.manthina@uconn.edu

Solution Processed Semiconductor Nanostructures and Nanocomposites for Dye Sensitized Solar Cells

Venkata Manthina, PhD

University of Connecticut, 2014

Dye sensitized solar cells (DSSC) are low cost alternatives to silicon solar cells. The conventional DSSC consists of two sandwiched pieces of conducting glass, one of them coated with mesoporous layer of nanoparticulate TiO_2 with a self-assembled monolayer of chemisorbed dye molecules, filled with an electrolyte for dye regeneration. Conventional dye sensitized solar cells use TiO_2 nanoparticles as electron transport material. Electron transport is critical for the performance of the dye sensitized solar cells, as they recombine with the electrolyte if they are not collected fast. Using nanoparticles introduce high surface area, but slows down the electron transport and prevent electron collection. We synthesized novel hybrid nanostructures with fast electron transport and high surface. Tested the new hybrid structures with different electrolytes and compared with conventional photoanodes. The band alignment of the nanocomposites is studied. The band edge engineering of the nanocomposites is studied for improved electron transport. The recombination in the DSSC is studied and blocking layers synthesized using ALD and $TiCl_4$ treatment are compared and the properties resulting to improved efficiencies in DSSC are studied. The photocurrent of the large ZnO nanorods based DSSC are improved from 0.4 mA/cm^2 to 4.4 mA/cm^2 using the above techniques.

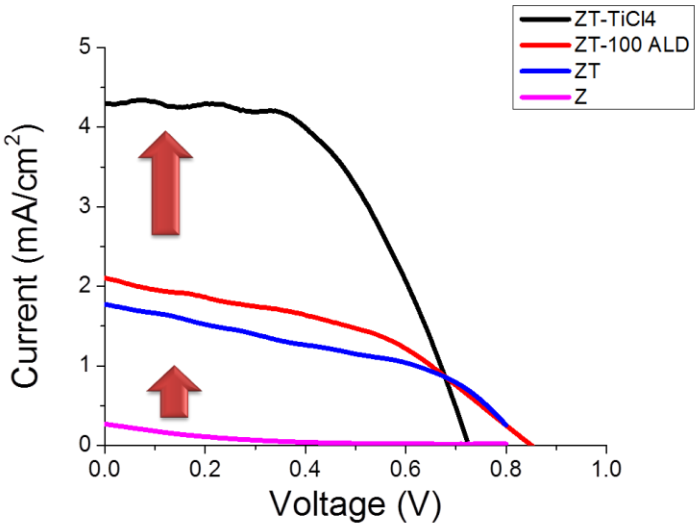

Solution Processed Semiconductor Nanostructures and Nanocomposites for Dye Sensitized Solar Cells

Venkata Manthina
B.Tech Jawharlal Nehru Technological University [2006]
MS Cleveland State University [2008]

A Dissertation
Submitted in Partial Fulfillment of the
Requirements for the Degree of Doctor of Philosophy
at the
University of Connecticut

[2014]

2014

APPROVAL PAGE

Doctor of Philosophy Dissertation

Solution Processed Semiconductor Nanostructures and Nanocomposites for Dye Sensitized Solar Cells

Presented by

VENKATA MANTHINA, MS, EIT

Major Advisor _____

Dr. Alexander Agrios

Associate Advisor _____

Dr. Prabhakar Singh

Associate Advisor _____

Dr. Puxian Gao

Associate Advisor _____

Dr. Helena Sliva

Associate Advisor _____

Dr. Baikun Li

Associate Advisor _____

Dr. Ioulia Valla

University of Connecticut

2014

Acknowledgement

- I want to thank my advisor **Dr. Alexander Agrios** for patiently providing the vision, encouragement and advice necessary for me to proceed through the doctoral program.
- I want to thank **Dr. Prabhakar Singh** for all his support and fruitful discussions.
- I want to thank **Dr. Baikun Li, Dr. Puxian Gao, Dr. Ioulia (Julia) Valla and Dr. Helena Silva** for kindly accepting my request for being in my PhD committee and giving valuable suggestions for my PhD work.
- I want to thank Dr. **Ali Gokirmak** and **Dr. Helena Silva** for the help with electron transport and lifetime measurements.
- I want to thank **Dr. Manoj Mahapatra** for the help with XRD and support.
- I want to thank my group members for all the support : **Perry, Juan Pablo, Avinash, Bowen, Tulsi(REU) , John(REU).**
- I want to thank **Yong-Tao Meng** and **Dave Kriz (Dr. Suibs Group)** for Diffuse Reflectence measurements and Atomic Layer Deposition.
- I want to thank **Michael Luciano (Dr. Brukner Group)** for Cobalt Electrolyte Synthesis.
- I want to thank **Prof. Papadimitrakopoulos** for help in Photoluminescence measurements.
- I want to thank **Pete, Gary, Mark, Sheila, Amy and Terry** for all the support
- I want to thank all my colleagues at Center for Clean Energy Engineering for all the support and help
- I want to thank National Science Foundation (NSF) and **Uconn foundation** for providing the funding for my research.
- I want to thank my parents **Nagamani** and **Lakshmana Rao** for supporting me and encouraging me with their best wishes.
- Finally I would like to thank my wife **Devaki** for cheering me up and stood by me throughout, without her my accomplishments are nowhere near as satisfying.

Table of Contents

Chapter 1
Introduction

1.1 Solar Energy and Market

Solar energy is the most abundant form of renewable energy on the planet. The solar resource is more than 200 times larger than all the others forms of energy combined.[1] It is the long-term sustainable source of energy. Even though solar electricity generation is growing, it still occupies less than 1% of the market share.[2] The total renewable energy generation has increased 3.1% per year and it is expected to grow from 19% in 2008 to 23% in 2035. Solar energy is the fastest growing technology in renewable energy sources and is expected to grow 22.8% annually until 2035. The predicted total installed photovoltaic (PV) capacity in the world in 2015 is between 131 and 196 GW; 100 GW milestone has been reached in 2013.[3] In today's market the commercially available silicon solar cells efficiency stand at 16 percent for Crystalline Silicon PV module, 11 percent for Thin-film PV module, 29 percent for Concentrator PV module.[4, 5] Due to manufacturing cost of the silicon solar cells put to electricity generation, the cost of the power would be 2-3 times higher than the fossil fuels.[6] As of 2011 the cost of solar power is less than for nuclear power production.[7] The price of photovoltaic modules fell 19% from $1.96 in 2010 to $1.59 per watt hour in 2011.[4] In order to make the electricity cheaper than fossil fuels, manufacturing costs has to be reduced by using earth abundant and low purity materials.[8]

A large number of systems are designed to benefit the solar energy apart from photovoltaics like solar concentrators, solar hot water and passive solar systems. All of these systems are under development. Photovoltaic systems convert the light energy into electricity; well know to everyone from applications in calculators and watches. Solar concentrators track the sun to

produce high optical intensities using mobile mirrors. The disadvantages are mobile mirrors employed are often very expensive, the focal point of the mirror has to be cooled and lot of space is required to prevent shadowing of the concentrators.[9] Solar hot water is widely used as roof top system and stored in well insulated tanks. It is easy to set up system on roof with a set of tubes and transparent cover. Passive solar systems are based on the direct entry of the solar radiation into heated environment through south side of the house. Low cost, simplicity and high thermal efficiency are the advantages of these systems.[10]

1.2 Photovoltaic Systems

In 1901, the solar distribution of the solar spectrum is explained by Max Planck by his famous Planck's law.[11] In 1905, Einstein explained the photoelectric effect[12] for which he received the Nobel Prize in 1921. This photoelectric effect explained the theoretical basis for all the photovoltaic devices and semiconductors that photons excite electrons from the valance band to the conduction band where they are collected and transported to the outer circuit. In 1914 Goldman and Brodsky confirmed the barrier at the semiconductor-metal interface[13], later studied in detail by Walter Schottky and Neville Mott in 1930s called the Mott-Schottky barrier.[14]

In 1918, Jan Czochralski, a Polish scientist, developed a way to measure crystallization rate of metals.[15] This technique was later adapted by Bell Labs to grow single crystals of suitable semiconductors in the 1950s.

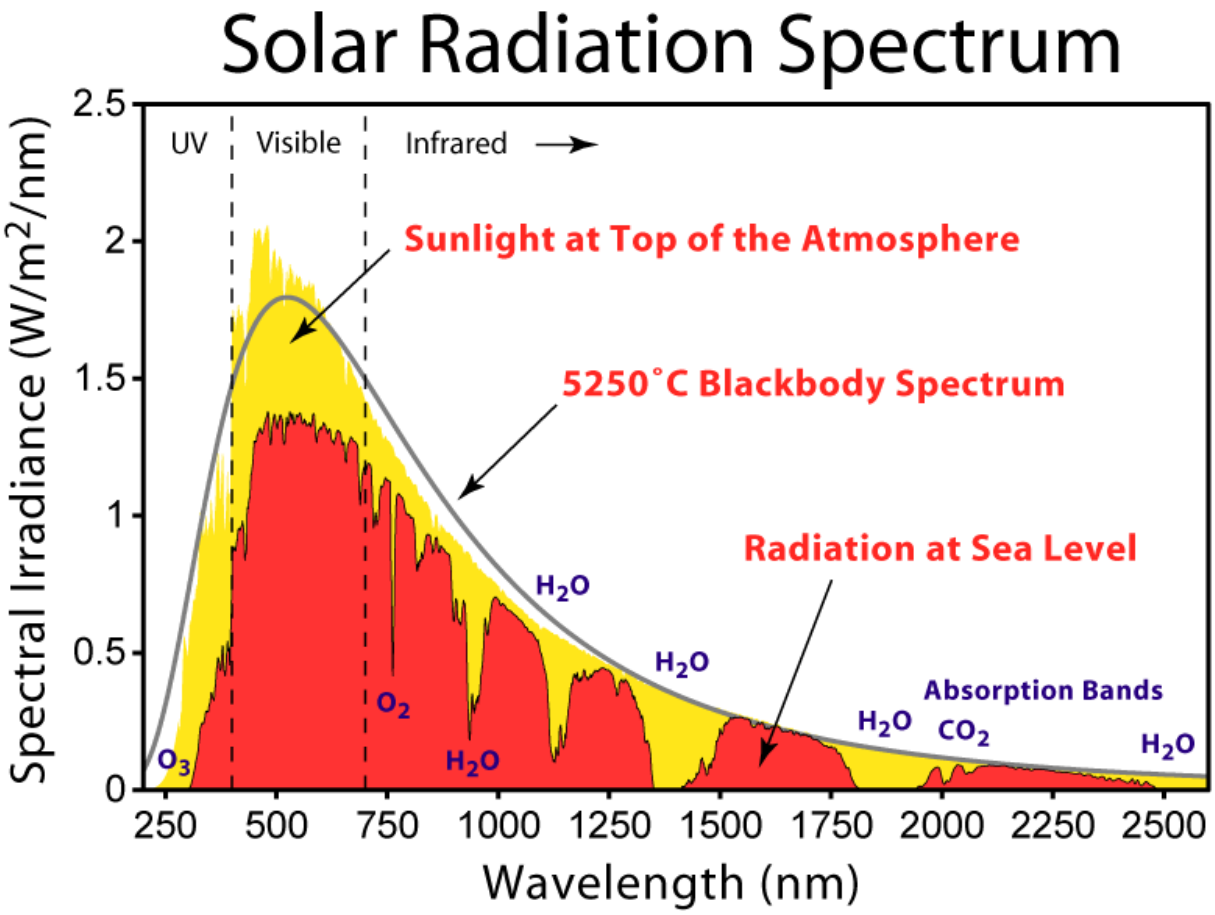

Figure1. 1 Solar spectrum

The photovoltaic effect in cadmium sulfide (CdS) was discovered by Audubert and Stora in 1932, opening up a way to II-VI solar cells.[16] In 1953 Bell chemist Fuller made near surface p-n junctions by treating n-type silicon wafers with boron trichloride.[17] In 1954 Chapin achieved 6% conversion efficiency, 50 times more efficient than the solar cells in 1930s.[18] In the later years *p-n* junctions with CdS, GaAs, InP and CdTe were studied for a higher efficiency, accelerated by theoretical calculations. During that time the cost of the solar power is very expensive making it viable only for space applications. In the early 1970 the cost of the solar power is 20$/watt the lowest during that time.[19]

In the 1970s during the energy crisis the interest and funding for alternative sources of energy increased. During this period the second generation of photovoltaic's emerged, such as polycrystalline and amorphous silicon, thin-film deposited silicon, CdTe, CuInSe2, (CIS) and Cu(In,Ga)Se2 (CIGS), as well as multijuntion cell technology. The cost of processing of the silicon solar cells is high due to high purity of the silicon required for the fabrication.

In the 1990s the third generation of solar cells emerged and is different from the traditional p-n junction solar cells. The charge separation still takes place at a junction. The technologies that include are dye-sensitized solar cells, polymer solar cells and nanocrystalline solar cells. Due to low cost and ease of fabrication these technologies are expected to takeover significant share of the market in the coming years. From 2000 to 2005 the global yearly solar production increased from 300MW to 2000MW.[20] The best research cells efficiencies are shown in Figure1. 2.

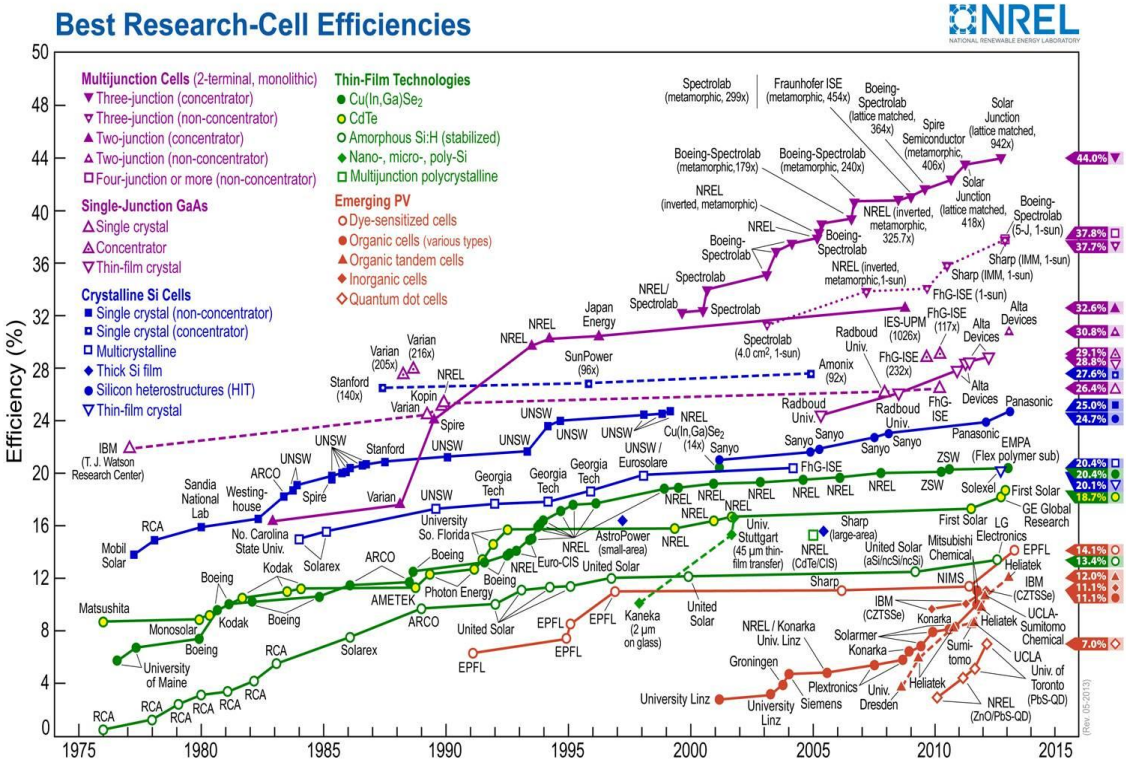

Figure1. 2 Research Cell Efficiencies

1.3 Dye-Sensitized Solar Cell

1.3.1 History and Background

In 1873 German photochemist, Vogel, via the dye sensitization of silver halide emulsions, leads to an extended photo response into the red and even infrared regions and the first panchromatic film rendering a realistic black and white picture.[21] In 1887, Moser observed the first case of dye-sensitized semiconductor electrode when using the dye erythrosin on silver halide electrodes. [22] In the 1960s Namba and Hishiki, Tributsch and Gerischer studied the electron injection from a photo-excited state of the dye molecules into the conduction band of the n-type semiconductor substrates using ZnO. [23, 24] These dye-sensitized cells were characterized with poor dye anchorage on semiconductor surface and low conversion efficiencies restricted by the limited, weak light absorption (in the order of 1 to 2%) of the dye monolayer on the planar surface. Semiconductors such as CdS, CdSe, GaP and Si underwent serious photocorrosion thus a stable, wide band-gap semiconductor, TiO_2, became the material of choice, following the successful demonstration of direct photolysis of water with TiO_2.[25]

Dye sensitized solar cells (DSSCs)[26] are developed as low-cost alternatives to silicon photovoltaics due to easy fabrication and production. In 1991 the development of efficient sensitizer and rough TiO_2 led to photoelectrochemical devices with conversion efficiency of 7.9% in simulated day light and 12% in diffuse daylight.[26] The discovery of the N3 and black dyes lead to photo conversion efficiency of 10% due to increased absorption of light.[27, 28] The efficiencies of DSSCs have increased considerably in the last 20 years, with the confirmed

record now standing at 12.3%.[29, 30] Increased efforts to increase the stability, lifetime and robustness were carried in parallel for commercialization of the technology. The global DSSC production in 2009 is 5MW and predicted to grow to 200MW in 2012. [31] The market share of DSSC is 1% of the PV market with 2012 production capacity, with companies' moving from pilot scale to manufacturing the cost of production will get lower.[32]

1.3.2 Operating Principle

The conventional DSSC consists of two sandwiched pieces of conducting glass, one of them coated with mesoporous layer of nanoparticulate TiO_2 with a self-assembled monolayer of chemisorbed dye molecules, filled with an electrolyte for dye regeneration. The dye is a transition metal complex or organic chromophore that harvests sunlight by absorbing strongly in visible region of the solar spectrum. Solar energy is harvested by the dye molecules adsorbed on the TiO_2 nanoparticulate film. When the photons from the sunlight hit the dye, it gets photo-excited and injects electrons into the conduction band of the TiO_2. Electrons are transported to the flourine doped tin oxide (FTO) front electrode and to the external circuit. A redox couple reduces the oxidized dye to neutral state and gets reduced by electrons from the platinized counter electrode. The principal photovoltaic losses in the DSSCs are due to incomplete light harvesting, recombination of the photoinjected electrons with the electrolyte and the overpotential required for dye regeneration.

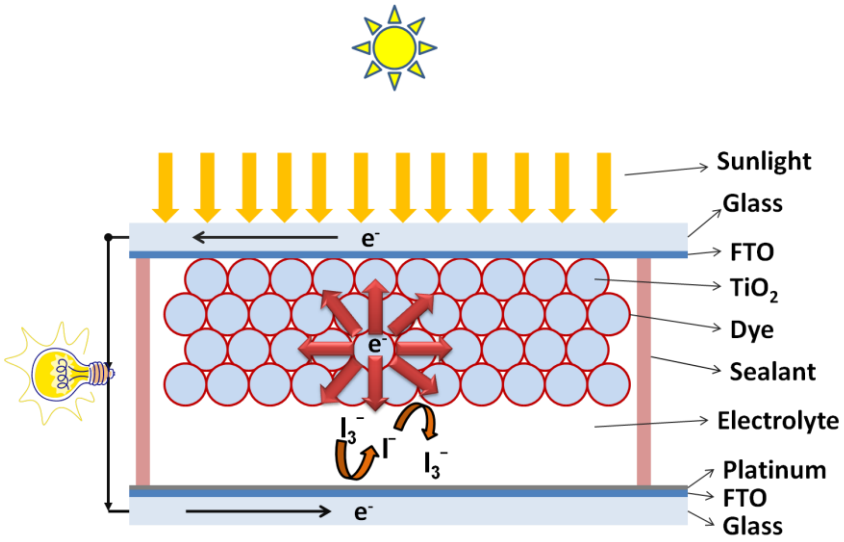

Figure1.3 Schematic of Conventional Dye Sensitized Solar Cell

1.3.3 Electron Transfer Processes

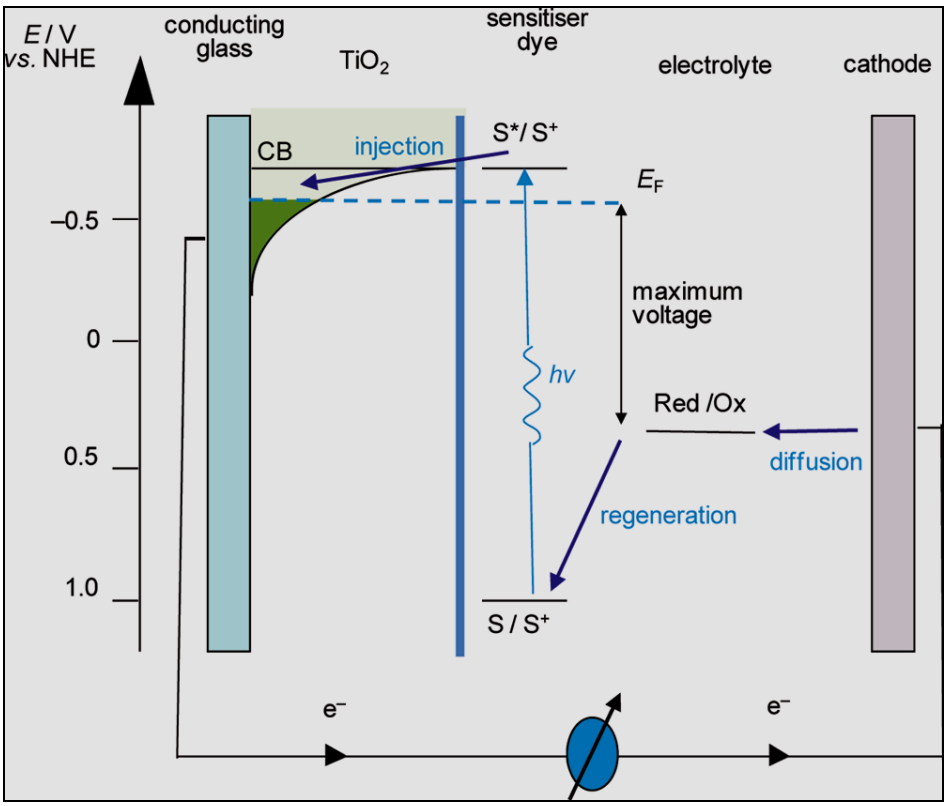

Figure1. 4 Energetics of Dye sensitized Solar Cells

The kinetics of different electron-transfer processes are summarized in Figure1. 5. The kinetic competition between the forward processes and the loss pathways determines the charge collection and separation processes, determining the efficiency of the DSSC. The electron injection from the sensitizer into the TiO_2 conduction band is taken place in 100 ps.[33, 34] The electron injection depends on the difference between the energy of the TiO_2 conduction band relative to the dye excited state oxidation potential. The presence of acidic ions can determine the energy level of conduction band. The presence of 0.1M Li^+ in electrolyte increase the injection rate 7 times.[35] If the density of accessible states is lower, it results in slower electron injection resulting in lower photocurrent.[36, 37, 38]

The decay of excited state of the dye to the ground state, which is the excited state lifetime of the dye is typically 10 ns for N719 and 20-60 ns for other Ru-based dyes.[39] The excited state lifetime of dye is also dependent on the potential determining ions. [40] The 10 ns lifetime of the N719 triplet state is sufficient to achieve an electron injection quantum yield of 90%.[41]

Dye regeneration is process of regeneration of the oxidized dyes by the redox couple in the electrolyte. In N719 iodide/iodine redox couple, most estimates of the interfacial energetics indicate that around 600 meV are lost in driving this regeneration reaction.[42, 43] This is the largest loss pathway critical for improving the efficiency of the DSSC. New electrolytes like Fc/Fc^{+}[44], Co^{2+}/ Co^{3+}[30], Cu^{+1}/Cu^{+2} [45] can reduce the high overpotential loss during the dye regeneration. The regeneration dynamics by iodide is around the time scale of 1 μs. Fast regeneration in the presence of cations like Li^+ and Mg^+ adsorbed on the TiO_2 surface due to higher local iodide concentration.[46]

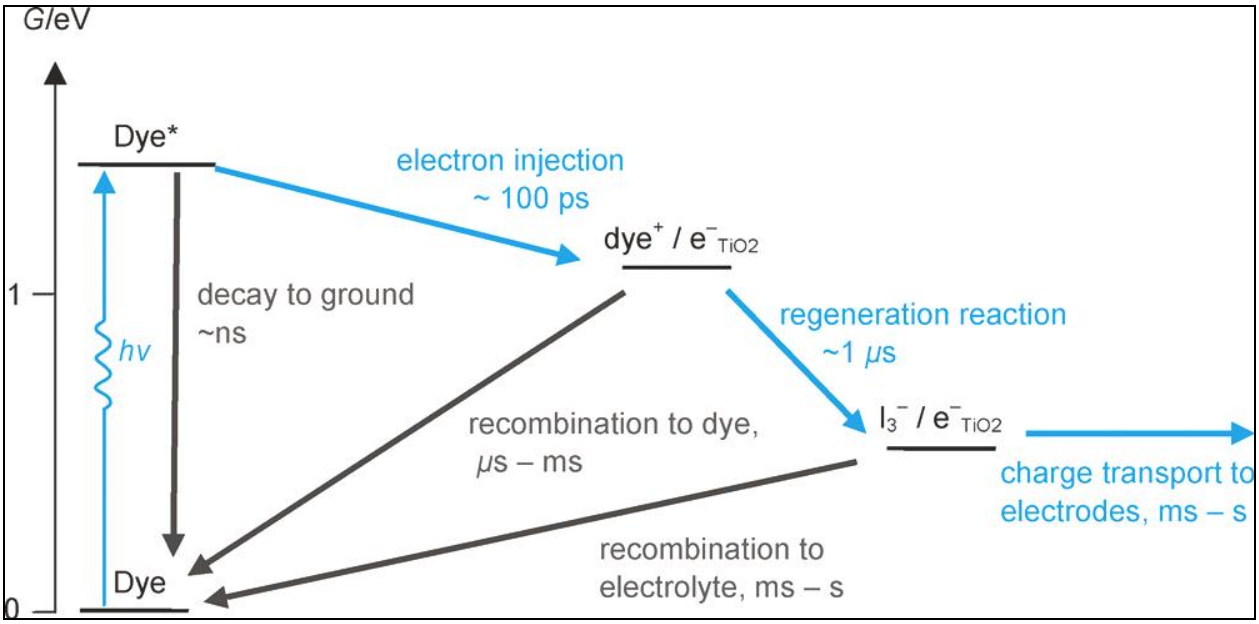

Figure1. 5 Schematic representation of the kinetics of DSSC. Forward processes of light absorption, electron injection, dye regeneration, and charge transport are indicated by blue arrows. The competing loss pathways of excited-state decay to ground and electron recombination with dye cations and oxidized redox couple are shown in gray. [41]

Recombination of the electrons to the dye is process in which the oxidized dye is reduced by recombination with the electrons in the conduction band of the semiconductor. The kinetics of this recombination reaction is dependent on the density of the trap states in the conduction band with time scale of μs-ms.

Recombination to the electrolyte is the process in which photoinjected electrons react with the oxidized electrolyte species. This recombination is a major loss path decreasing the efficiency of the DSSC. Intrinsic semiconductor defects trap states and intermediate states for electron transfer to the oxidized electrolyte are the cause of to this recombination. The kinetics of this recombination reaction is dependent on the density of the trap states in the conduction band with time scale of ms-s. There are various studies related to interfacial engineering of the electrolyte

and the semiconductor. Barrier layers are deposited with MgO[47], $CaCO_3$[48], Al_2O_3[49], Nb_2O_5[50, 51], TiO_2[52], In_2O_3[53], ZrO_2[54] and ZnO[51] recombination with the electrolyte.

The charge transport in the conventional TiO_2 films is slower when compared to 1D nanostructure like nanorods and nanowires, but 1-D structures have low surface area. The kinetics of charge transport is dependent on the defect states, electrical conductivity and electron mobility of semiconductor used with time scale of ms-s.

1.3.4 Charge Collection Efficiency

The charge collection efficiency is is a measure of the percent of photoinjected electrons that reach the electron collector without recombining with either the oxidized dye or oxidized component in the redox electrolyte. The time constant for electron transport to the collection electrode must be faster than charge recombination of injected electrons with electrolyte for efficient charge collection. The charge collection efficiency determines the efficiency of the DSSC.

The expression for charge collection efficiency is given by:[55]

$$\eta_{\text{collection}} = 1 - \frac{\tau_{\text{tr}}}{\tau_{\text{R}}}$$

Where τ_{tr} the transport is time and τ_R is recombination time

Measure of $\eta_{\text{collection}}$ is the electron diffusion length $L_n (L_n = (D\tau_R)^{1/2}$,where D and τ_R are the respective electron diffusion coefficient and recombination time constant or equivalent the electron lifetime.

IPCE which is the incident photon to electron conversion efficiency is given by:

$$IPCE = \eta_{\text{LHE}} \times \eta_{\text{inj}} \times \eta_{\text{collection}}$$

where η_{LHE} is the light harvesting efficiency, η_{inj} is the charge injection efficiency and $\eta_{\text{collection}}$ is the charge collection efficiency. With the high efficiency DSSC the η_{LHE} and η_{inj} are close to 1. Therefore the major strategy to increase the DSSC efficiency is to design photoanodes with fast electron transport and decrease the recombination.

1.3.5 Cost of Production

The availability of materials at cheaper rate decreases the cost of production. Based on the studies by Desilvestro et al[56] the cost of production of DSSC panel is 55\$/m^2 or 0.78\$/W$_p$ assuming the efficiency of panel at only 7%. There are no limitations on the availability of the materials used in DSSC.

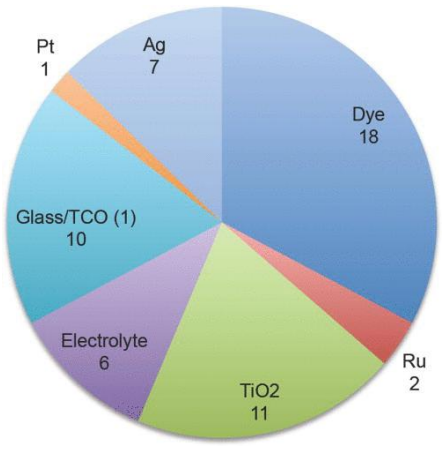

Figure1. 6 Chart showing predicted breakdown of material costs in \$/m^2 for different DSSC components. Data taken from the middle of the range suggested by Desilvestro et al.[56] based on 100,000 m^2 annual production.[57]

From the Figure1. 6 the expensive components in DSSCs are the dye, TiO_2, and glass/TCO substrate. Ruthenium is only 10% of the total dye cost, but the synthesis and attachment of ligands and subsequent purification are quite expensive. The amount of Ru used is relatively low quantity 0.1 g/m ^{2}. Manufacturing dyes of kilogram compared to gram volumes reduces price from $700/g to $70/g.[57] TiO_2 is abundant and cheap, but hydrothermal synthesis of TiO_2 colloids makes it expensive. Techniques such as flame pyrolysis can make it cheaper but controlling the particle size is relatively hard. Pt used in counter electrode is expensive but is used in extremely small quantities 0.02 g/m ^{2}. Cost of electrolytes based on organic solvents is not problematic, although ionic liquids used to improve stability are still more expensive than desired. Ag used for better electrical contacts and interconnects imparts a significant cost of DSSC. TCO-coated glass FTO or ITO is expensive. The cost of glass per module area doubles for sandwich cells compared to monolithic modules. It is expected that scaling will lower the cost of glass to acceptable levels when produced at high volumes.

In addition to research and development changing the design of the DSSC module and process integration can reduce the cost of DSSC.

1.4 Proposed Hybrid Dye-Sensitized Solar Cell

Our approach is to utilize novel semiconductor structures to attain fast electron transport in order to improve charge collection efficiency in DSSCs.

Electron transport in DSSCs is slow due to trapping of the electrons in the grain boundaries and the relatively long and tortuous path of the electron to the FTO.[58, 59] In a 10 µm thick film an electron visits about 10^6 nanoparticles on average before reaching the FTO surface. [60] The resulting slow transport is adequate in the presence of iodide/triiodide, since its recombination

kinetics are slow, but inadequate when using an alternative redox couple with faster recombination. The slow electron transport is responsible for the limited research on the discovery of alternate redox shuttles for DSSCs. Improving the electron transport will allow the use of other fast recombining electrolytes successfully.

In DSSCs, the I^-/ I_3^- redox couple limits the overall efficiency due to the high overpotential (ca. 0.5 V) for dye regeneration by I^-. This is believed to be due to the complex multielectron mechanism of the I^-/ I_3^- redox couple involving the radicals diiodide ($I_2^{-\cdot}$) and atomic iodine ($I^\cdot$). [42] The effect is that the dye HOMO level must be about 0.5 V more positive than the I^-/ I_3^- redox level. Since the voltage output of the cell is the difference between the redox level and the quasi-Fermi level in the semiconductor, this 0.5 V is lost. An alternative redox electrolyte that could regenerate the sensitizer from a potential closer to its HOMO would result in higher cell voltage and efficiency, if all else were held equal. Unfortunately, alternatives (such as iron or cobalt complexes) tend to recombine rapidly with conduction-band electrons, reducing the quasi-Fermi level and resulting in no benefit. The use of I^-/I_3^- is a hindrance for the commercialization of the DSSCs due to corrosion of the silver current collectors and platinum counter electrode and absorption of the light at 430 nm by the triodide in the electrolyte.[61]

Fast electron transport can be achieved by developing 1-D nanostructures like nanotubes, nanorods and nanowires of metal oxides. ZnO is a highly favorable material for application in DSSCs since it can be grown in monocrystalline nanorods using facile methods, its electron mobility is high,[62], and its band edge energies are very close to those of TiO_2.[63] ZnO is the metal oxide with the second highest efficiency achieved in DSSCs.[64, 65, 66] ZnO nanorods can be

synthesized on the substrate in-situ through various procedures, such as chemical bath deposition [67, 68], electrodeposition,[69, 70, 71] and chemical vapor deposition.[72, 73] However, the main disadvantage of nanorods is a lower surface area than a nanoparticle film for adsorption of light-harvesting molecules. In addition, the dye performance tends to be worse on ZnO than on TiO_2. Among all the methods chemical bath deposition is low temperature, low cost, and large area processing suitable for industrial applications. It offers the advantages such as in-situ doping, catalyst free growth and environmentally favorable process. Chemical bath deposition also allows the development of the flexible devices. Therefore we used chemical bath deposition for the synthesis of the ZnO nanorods

To create a structure with both fast electron transport and high surface area, we developed a hybrid photoanode consisting of ZnO nanorods coated with TiO_2 nanoparticles using facile wet-chemical methods.

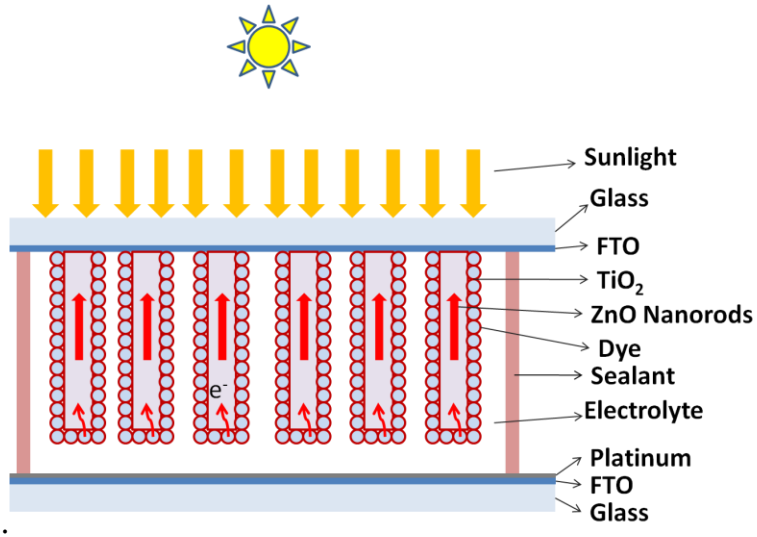

.

Figure1. 7 Schematic of Novel ZnO-TiO_2 Hybrid Dye Sensitized Solar Cell

1.5 References

1. R. a. M. P. Perez, "A fundamental look at energy reserves for the planet," pp. 2-3. in, Vol. 50. The IEA SHC Solar Update, 2009.
2. "Short-Term Energy Outlook (STEO) ". in. U.S. Energy Information Administration, Washington D.C, 2013.
3. J. Ciesielska, " Global market outlook for photovolatics until 2015." in. European Photovoltaic Industry Association, 2011.
4. "Solar Photovoltaic Cell/Module Shipments Report 2011." in. U.S. Energy Information Administration Washington D.C, 2012.
5. "Solar America Initiative: A Plan for the Integrated Research, Development, and Market Transformation of Solar Energy Technologies.." in. Edited by D. U. S. D. o. Energy). Office of Energy Efficiency and Renewable Energy Solar Energy Technologies Program., Washington, D.C.: DOE, 2007.
6. " Annual Energy Outlook 2012." in. U.S. Energy Information Administration Washington D.C, 2012.
7. J. Quiggin, "The End of the Nuclear Renaissance." in National Interest. 2012.
8. N. S. Lewis, "Toward Cost-Effective Solar Energy Use," *Science*, 315[5813] 798-801 (2007).
9. M. J. Currie, J. K. Mapel, T. D. Heidel, S. Goffri, and M. A. Baldo, "High-Efficiency Organic Solar Concentrators for Photovoltaics," *Science*, 321[5886] 226-28 (2008).
10. N. Susheela and M. Sharp, "Heat Pipe Augmented Passive Solar System for Heating of Buildings," *Journal of Energy Engineering*, 127[1] 18-36 (2001).

11. M. Planck, "On the Law of the Energy Distribution in the Normal Spectrum," *Annalen der Physik IV,* 4 553 (1901).

12. A. Einstein, "Über einen die Erzeugung und Verwandlung des Lichtes betreffenden heuristischen Gesichtspunkt," *Annalen der Physik* 17 (1905).

13. A. B. Goldmann, J. , *Annalen der Physik* 44 (1914).

14. W. Schottky, *Physik. Z.,* 31 (1930).

15. J. Z. Czochralski, "Ein neues Verfahren zur Messung des Kristallisationsgeschwindigkeit der Metalle," *Phys. Chem.,* 92 (1917).

16. R. S. Audubert, C. , "Photovoltaic Effect of Cadmium Sulfide.," *Comptes Rendus,* 194 (1932).

17. C. Fuller, "Book #24863.″ AT&T Archives: Warren, NJ, (10-7-53).

18. D. Chapin, " Loc. 124-11-02.″ AT&T Archives: Warren, NJ, (1-26-54 & 2-23-54).

19. "Sunlight Converted to Electricity." in Sunday Globe. Boston, 1973.

20. A. Luque. in IEEE International Symposium on Industrial Electronics. 2007.

21. W. West, "First hundred years of spectral sensitization. Proc. Vogel Cent. Symp.," *Photogr. Sci. Eng.,* 18 (1974).

22. J. Moser., "Notiz uber die Versta rkung photoelektrischer Strome.," *Monatsch. Chem.,* 8 (1887).

23. S. H. Namba, Y. , "Color sensitization of zinc oxide with cyanide dyes.," *J. Phys. Chem.,* 69 774-79 (1965).

24. H. T. Gerischer, H., "Electrochemische Untersuchungen zur spectraleu sensibilisierung von ZnO-Einkristallen.," *Ber. Bunsenges. Phys. Chem.,* 72 437-45.

25. A. Fujishima and K. Honda, "Electrochemical Photolysis of Water at a Semiconductor Electrode," *Nature,* 238[5358] 37-38 (1972).

26. B. O'Regan and M. Gratzel, "A low-cost, high-efficiency solar cell based on dye-sensitized colloidal TiO_2 films," *Nature,* 353[6346] 737-40 (1991).

27. M. K. Nazeeruddin, A. Kay, I. Rodicio, R. Humphry-Baker, E. Mueller, P. Liska, N. Vlachopoulos, and M. Graetzel, "Conversion of light to electricity by cis-X2bis(2,2'-bipyridyl-4,4'-dicarboxylate)ruthenium(II) charge-transfer sensitizers (X = Cl-, Br-, I-, CN-, and SCN-) on nanocrystalline titanium dioxide electrodes," *Journal of the American Chemical Society,* 115[14] 6382-90 (1993).

28. M. K. Nazeeruddin, P. Péchy, and M. Grätzel, "Efficient panchromatic sensitization of nanocrystalline TiO_2 films by a black dye based on a trithiocyanato-ruthenium complex," *Chemical Communications*[18] 1705-06 (1997).

29. M. A. Green, K. Emery, Y. Hishikawa, and W. Warta, "Solar cell efficiency tables (version 37)," *Progress in Photovoltaics: Research and Applications,* 19[1] 84-92 (2011).

30. A. Yella, H.-W. Lee, H. N. Tsao, C. Yi, A. K. Chandiran, M. K. Nazeeruddin, E. W.-G. Diau, C.-Y. Yeh, S. M. Zakeeruddin, and M. Grätzel, "Porphyrin-Sensitized Solar Cells with Cobalt (II/III)–Based Redox Electrolyte Exceed 12 Percent Efficiency," *Science,* 334[6056] 629-34 (2011).

31. S. Villarroya-Lidon. in 4th International Conference on the Industrialisation of DSC. Colorado Springs, 2010.

32. K. Kalyanasundaram, "Dye-sensitized solar cells.″ CRC press: Lausanne, (2010).

33. S. Ardo and G. J. Meyer, "Photodriven heterogeneous charge transfer with transition-metal compounds anchored to TiO_2 semiconductor surfaces," *Chemical Society Reviews,* 38[1] 115-64 (2009).

34. N. A. Anderson and T. Lian, "Ultrafast electron transfer at the molecule-semiconductor nanoparticle interface," *Annual Review of Physical Chemistry,* 56[1] 491-519 (2005).

35. Y. Tachibana, S. A. Haque, I. P. Mercer, J. E. Moser, D. R. Klug, and J. R. Durrant, "Modulation of the Rate of Electron Injection in Dye-Sensitized Nanocrystalline TiO_2 Films by Externally Applied Bias," *The Journal of Physical Chemistry B,* 105[31] 7424-31 (2001).

36. S. A. Haque, E. Palomares, B. M. Cho, A. N. M. Green, N. Hirata, D. R. Klug, and J. R. Durrant, "Charge Separation versus Recombination in Dye-Sensitized Nanocrystalline Solar Cells: the Minimization of Kinetic Redundancy," *Journal of the American Chemical Society,* 127[10] 3456-62 (2005).

37. C. A. Kelly, F. Farzad, D. W. Thompson, J. M. Stipkala, and G. J. Meyer, "Cation-Controlled Interfacial Charge Injection in Sensitized Nanocrystalline TiO_2," *Langmuir,* 15[20] 7047-54 (1999).

38. D. F. Watson and G. J. Meyer, "Cation effects in nanocrystalline solar cells," *Coordination Chemistry Reviews,* 248[13–14] 1391-406 (2004).

39. A. Hagfeldt and M. Grätzel, "Molecular Photovoltaics," *Accounts of Chemical Research,* 33[5] 269-77 (2000).

40. I. J. McNeil, L. Alibabaei, D. L. Ashford, and C. J. Fecko, "Investigation of Factors That Affect Excited-State Lifetime Distribution of Dye-Sensitized Nanoparticle Films," *The Journal of Physical Chemistry C,* 117[34] 17412-20 (2013).

41. A. Listorti, B. O'Regan, and J. R. Durrant, "Electron Transfer Dynamics in Dye-Sensitized Solar Cells," *Chemistry of Materials,* 23[15] 3381-99 (2011).

42. G. Boschloo and A. Hagfeldt, "Characteristics of the Iodide/Triiodide Redox Mediator in Dye-Sensitized Solar Cells," *Accounts of Chemical Research,* 42[11] 1819-26 (2009).

43. B. C. O'Regan and J. R. Durrant, "Kinetic and Energetic Paradigms for Dye-Sensitized Solar Cells: Moving from the Ideal to the Real," *Accounts of Chemical Research,* 42[11] 1799-808 (2009).

44. T. Daeneke, T.-H. Kwon, A. B. Holmes, N. W. Duffy, U. Bach, and L. Spiccia, "High-efficiency dye-sensitized solar cells with ferrocene-based electrolytes," *Nat Chem,* 3[3] 211-15 (2011).

45. M. Brugnati, S. Caramori, S. Cazzanti, L. Marchini, R. Argazzi, and C. A. Bignozzi, "Electron Transfer Mediators for Photoelectrochemical Cells Based on Cu(I) Metal Complexes," *International Journal of Photoenergy,* 2007 (2007).

46. S. Pelet, J.-E. Moser, and M. Grätzel, "Cooperative Effect of Adsorbed Cations and Iodide on the Interception of Back Electron Transfer in the Dye Sensitization of Nanocrystalline TiO_2," *The Journal of Physical Chemistry B,* 104[8] 1791-95 (2000).

47. L. Grinis, S. Kotlyar, S. Rühle, J. Grinblat, and A. Zaban, "Conformal Nano-Sized Inorganic Coatings on Mesoporous TiO_2 Films for Low-Temperature Dye-Sensitized Solar Cell Fabrication," *Advanced Functional Materials,* 20[2] 282-88 (2010).

48. N. Okada, S. Karuppuchamy, and M. Kurihara, "An Efficient Dye-sensitized Photoelectrochemical Solar Cell Made from $CaCO_3$ coated TiO_2 Nanoporous Film," *Chemistry Letters,* 34[1] 16-17 (2005).

49. E. Palomares, J. N. Clifford, S. A. Haque, T. Lutz, and J. R. Durrant, "Control of Charge Recombination Dynamics in Dye Sensitized Solar Cells by the Use of Conformally Deposited Metal Oxide Blocking Layers," *Journal of the American Chemical Society,* 125[2] 475-82 (2002).

50. A. Zaban, S. G. Chen, S. Chappel, and B. A. Gregg, "Bilayer nanoporous electrodes for dye sensitized solar cells," *Chemical Communications*[22] 2231-32 (2000).

51. E. Guillén, E. Azaceta, A. Vega-Poot, J. Idígoras, J. Echeberría, J. A. Anta, and R. Tena-Zaera, "ZnO/ZnO Core–Shell Nanowire Array Electrodes: Blocking of Recombination and Impressive Enhancement of Photovoltage in Dye-Sensitized Solar Cells," *The Journal of Physical Chemistry C,* 117[26] 13365-73 (2013).

52. J.-H. Kim, K.-J. Lee, J.-H. Roh, S.-W. Song, J.-H. Park, I.-H. Yer, and B.-M. Moon, "Ga-doped ZnO transparent electrodes with TiO_2 blocking layer/nanoparticles for dye-sensitized solar cells," *Nanoscale Res Lett,* 7[1] 1-4 (2012).

53. T. P. Brennan, J. T. Tanskanen, K. E. Roelofs, J. W. F. To, W. H. Nguyen, J. R. Bakke, I. K. Ding, B. E. Hardin, A. Sellinger, M. D. McGehee, and S. F. Bent, "TiO_2 Conduction Band Modulation with In2O3 Recombination Barrier Layers in Solid-State Dye-Sensitized Solar Cells," *The Journal of Physical Chemistry C,* 117[46] 24138-49 (2013).

54. T. C. Li, M. r. S. Góes, F. Fabregat-Santiago, J. Bisquert, P. R. Bueno, C. Prasittichai, J. T. Hupp, and T. J. Marks, "Surface Passivation of Nanoporous TiO_2 via Atomic Layer Deposition of ZrO_2 for Solid-State Dye-Sensitized Solar Cell Applications," *The Journal of Physical Chemistry C,* 113[42] 18385-90 (2009).

55. G. Schlichthörl, N. G. Park, and A. J. Frank, "Evaluation of the Charge-Collection Efficiency of Dye-Sensitized Nanocrystalline TiO_2 Solar Cells," *The Journal of Physical Chemistry B,* 103[5] 782-91 (1999).

56. K. Kalyanasundaram, "Dye-sensitized Solar Cells." in "Packaging, Scale-up, and Commercialization of Dye Solar Cells**.** Edited by M. B. H. Desilvestro, S. Tulloch, and G. E. Tulloch. CRC Press, Lusanne, 2010.

57. J. B. Baxter, "Commercialization of dye sensitized solar cells: Present status and future research needs to improve efficiency, stability, and manufacturing," *Journal of Vacuum Science & Technology A,* 30[2] - (2012).

58. J. Bisquert, D. Cahen, G. Hodes, S. Rühle, and A. Zaban, "Physical Chemical Principles of Photovoltaic Conversion with Nanoparticulate, Mesoporous Dye-Sensitized Solar Cells," *The Journal of Physical Chemistry B,* 108[24] 8106-18 (2004).

59. J. Nissfolk, K. Fredin, A. Hagfeldt, and G. Boschloo, "Recombination and Transport Processes in Dye-Sensitized Solar Cells Investigated under Working Conditions," *The Journal of Physical Chemistry B,* 110[36] 17715-18 (2006).

60. N. Kopidakis, K. D. Benkstein, J. van de Lagemaat, and A. J. Frank, "Transport-Limited Recombination of Photocarriers in Dye-Sensitized Nanocrystalline TiO_2 Solar Cells," *The Journal of Physical Chemistry B,* 107[41] 11307-15 (2003).

61. S. Yanagida, Y. Yu, and K. Manseki, "Iodine/Iodide-Free Dye-Sensitized Solar Cells," *Accounts of Chemical Research,* 42[11] 1827-38 (2009).

62. M. Quintana, T. Edvinsson, A. Hagfeldt, and G. Boschloo, "Comparison of Dye-Sensitized ZnO and TiO_2 Solar Cells: Studies of Charge Transport and Carrier Lifetime," *The Journal of Physical Chemistry C,* 111[2] 1035-41 (2006).

63. K. Keis, C. Bauer, G. Boschloo, A. Hagfeldt, K. Westermark, H. Rensmo, and H. Siegbahn, "Nanostructured ZnO electrodes for dye-sensitized solar cell applications," *Journal of Photochemistry and Photobiology A: Chemistry,* 148[1-3] 57-64 (2002).

64. F. Xu and L. Sun, "Solution-derived ZnO nanostructures for photoanodes of dye-sensitized solar cells," *Energy & Environmental Science,* 4[3] 818-41 (2011).

65. K. Keis, E. Magnusson, H. Lindström, S.-E. Lindquist, and A. Hagfeldt, "A 5% efficient photoelectrochemical solar cell based on nanostructured ZnO electrodes," *Solar Energy Materials and Solar Cells,* 73[1] 51-58 (2002).

66. M. Saito and S. Fujihara, "Large photocurrent generation in dye-sensitized ZnO solar cells," *Energy & Environmental Science,* 1[2] 280-83 (2008).

67. P. O'Brien, T. Saeed, and J. Knowles, "Speciation and the nature of ZnO thin films from chemical bath deposition," *Journal of Materials Chemistry,* 6[7] 1135-39 (1996).

68. L. Vayssieres, K. Keis, A. Hagfeldt, and S.-E. Lindquist, "Three-Dimensional Array of Highly Oriented Crystalline ZnO Microtubes," *Chemistry of Materials,* 13[12] 4395-98 (2001).

69. T. Yoshida, M. Tochimoto, D. Schlettwein, D. Wöhrle, T. Sugiura, and H. Minoura, "Self-Assembly of Zinc Oxide Thin Films Modified with Tetrasulfonated Metallophthalocyanines by One-Step Electrodeposition," *Chemistry of Materials,* 11[10] 2657-67 (1999).

70. B. O'Regan, V. Sklover, and M. Gratzel, "Electrochemical Deposition of Smooth and Homogeneously Mesoporous ZnO Films from Propylene Carbonate Electrolytes," *Journal of The Electrochemical Society,* 148[7] C498-C505 (2001).

71. L. Xu, Q. Chen, and D. Xu, "Hierarchical ZnO Nanostructures Obtained by Electrodeposition," *The Journal of Physical Chemistry C,* 111[31] 11560-65 (2007).

72. R. R. Bacsa, J. Dexpert-Ghys, M. Verelst, A. Falqui, B. Machado, W. S. Bacsa, P. Chen, S. M. Zakeeruddin, M. Graetzel, and P. Serp, "Synthesis and Structure–Property Correlation in Shape-Controlled ZnO Nanoparticles Prepared by Chemical Vapor Synthesis and their Application in Dye-Sensitized Solar Cells," *Advanced Functional Materials,* 19[6] 875-86 (2009).

73. M. H. Huang, Y. Wu, H. Feick, N. Tran, E. Weber, and P. Yang, "Catalytic Growth of Zinc Oxide Nanowires by Vapor Transport," *Advanced Materials,* 13[2] 113-16 (2001).

Chapter 2
Experimental

2.1 Materials

2.1.1 Substrates.

The substrate of the photoelectrode serves as collector for the photogenerated current and has therefore to be well conducting. It must also form an ohmic contact with the dye sensitized semiconductor layer, but should show a large overvoltage for reduction of the redox electrolyte in order to minimize the dark current. In this work fluorine-doped tin oxide (FTO) 300 nm is used as transparent conducting oxide (TCO) deposited on glass plate 2.2 mm thick, having parameters FTO, transmission >80% in the visible spectrum; sheet resistance 8Ω/□ was purchased from Hartford Glass Co(USA)

2.1.1 Colloidal TiO_2 particles synthesis.

The TiO_2 (20 nm) paste was made by adding acetic acid into titanium iso-propoxide and stirred to achieve a complete hydrolysis reaction. A white precipitate formed during reaction was heated and peptized in a presence of nitric acid, then kept stirring in a hot titanium autoclave for colloid to grow hydrothermally. The colloid was then redispersed by sonication and cencentrated by rotary-evaporator. Detailed preparation of 20nm particle size TiO_2 is described elsewhere.[1]

2.1.3 Preparation of counter electrode

Counter electrodes were prepared by thermal decomposition of platinum precursor on conducting glass TEC 8. A little hole was drilled through the glass using dremel 200 with diamond drill bit in order to fill in the electrolyte during the assembly step. A few drops of 5-10

M hexachloroplatinic (IV) acid hexahydrate (H2PtCl6) in anhydrous isopropanol was spread onto the conducting glass surface, dried in air, and heated at 400ºC for 20 min.

2.1.4 Sensitizers

Two dyes are used in the study N719 obtained from Dyesol (Australia) and D149 obtained from Sigma-Aldrich (USA). The structures of the Dyes are given below

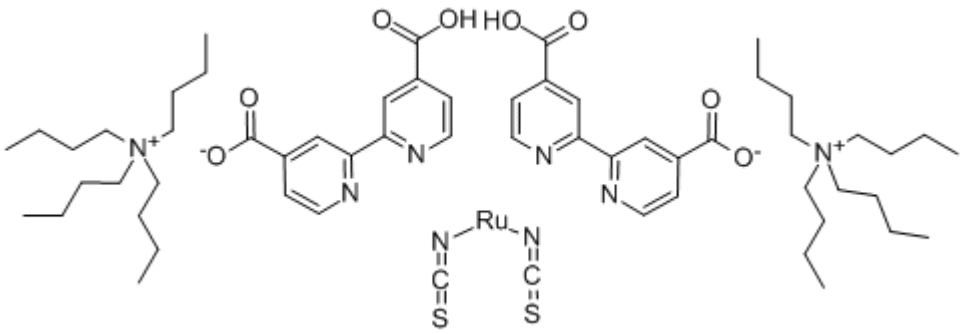

Figure 2. 1 Molecular structure of N719.

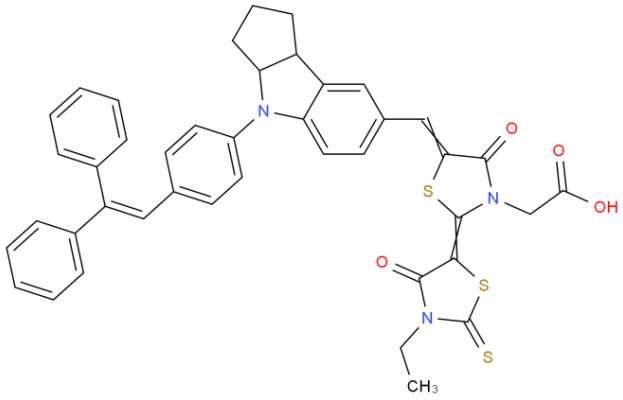

Figure 2. 2 Molecular structure of D149.

The D149 dye solution (0.5 mM) is prepared in a mixed solvent of acetonitrile and tert-butyl alcohol (volume ratio 1:1). N719 dye solution (3mM) is prepared using ethanol as solvent. The dyeing time is maintained at 12 hours for all the samples.

2.1.5 Electrolytes

Fundamental electrolytes were prepared by dissolving/mixing different components in the solvent. Minimal electrolyte recipes were used to exclude complications due to interactions with the various additives that are commonly used. Iodide/triiodide (I^-/I_3^-) electrolyte was prepared with 0.5 M tetrabutylammonium iodide and 0.05 M iodine (I_2) in 3-methoxypropionitrile. The ferrocene/ferrocenium (Fc/Fc^+) electrolyte contained 0.1 M ferrocene and 0.05 M ferrocenium hexafluorophosphate (Aldrich) in 3-methoxypropionitrile. The Fc/Fc^+ electrolyte was deoxygenated by bubbling, nitrogen 10 minutes prior to cell fabrication to minimize reaction of ferreocene with oxygen.[2] [3]

2.1.6 Device Fabrication

To fabricate the DSSC test device, the sensitized photoanode was rinsed with acetonitrile and then assembled with the counter electrode. Both glasses were separated by a 25µm-thick Surlyn hot melt (Solaronix, Switzerland) and sealed by heating on hot plate at 100°C. The internal space was filled with electrolyte. The hole was subsequently sealed by a Surlyn sheet and covered by a thin glass to avoid the leakage of the electrolyte.

Finally, copper tape (3M, USA) was applied on each side of the FTO electrodes to reduce the series resistance of the device and ensure a good electrical contact with measurement cables. In general, up to 3 devices were fabricated for each experimental variable change in order to make the deviation statistics

2.2 Solar cell Characterization

2.2.1 J-V Characteristics

Current-Voltage measurement is a simple technique to evaluate solar cells under illumination and dark conditions. The rate of photo generated current (J) is the sum of rate of electrons transported and rate of electrons recombining with redox electrolyte.

In the dark the applied voltage bias generates a dark current that flows in the direction opposite to the photocurrent under illumination.

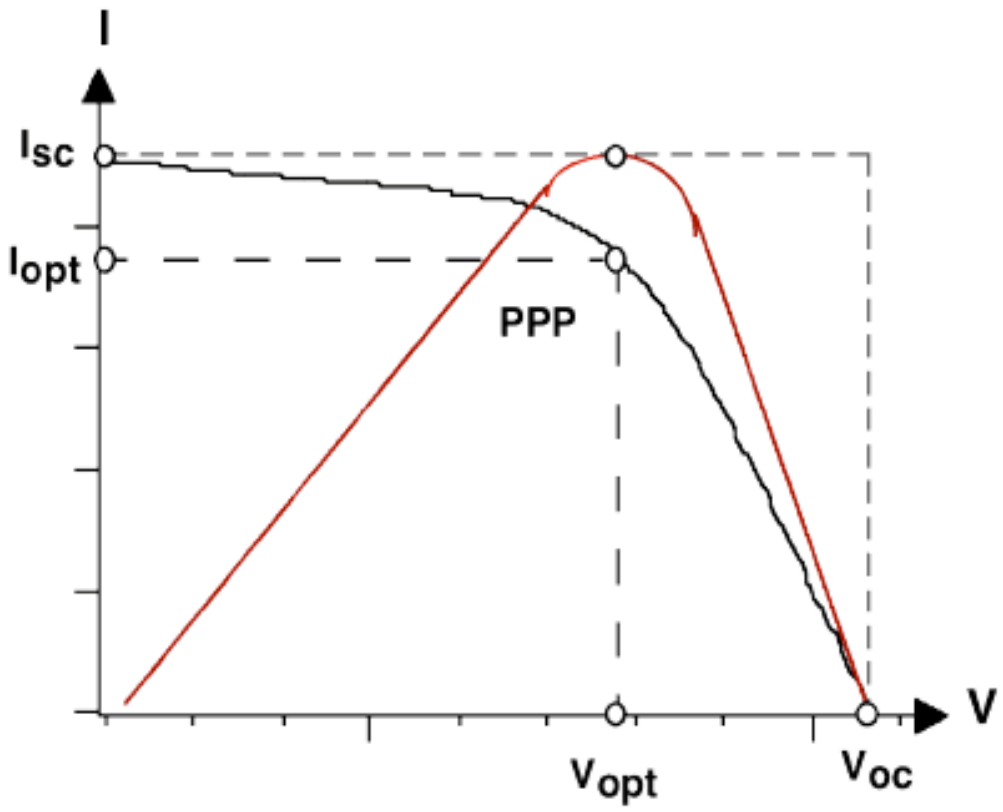

Figure 2.3 A representative of I-V curve of solar cell under illumination.

For an ideal diode the relation between the dark current and voltage is given by equation

$$I_{\text{dark}} = I_{\text{s}}\left(e^{\frac{qV}{k_{\text{B}}T}} - 1 \right) \qquad (2.\ 1)$$

I_s is saturation current of diode

q is the elementary charge

V is the applied voltage on the terminals of the cell

Under illumination the current-voltage characteristics follow

$$I = I_{\text{ph}} - I_{\text{dark}} = I_{\text{ph}} - I_{\text{s}}(e^{(qV/k_{\text{B}}T)} - 1) \quad (2.\ 2)$$

where I_{ph} is the photocurrent that depends on irradiation intensity and VT is often referred to as the thermal voltage that equals k_BT/q

For non-ideal devices, an ideality factor, m, is used to describe the weaker dependence of dark current on voltage.

$$I = I_{\text{ph}} - I_{\text{s}}(e^{(V/mVT)} - 1) \quad (2.3)$$

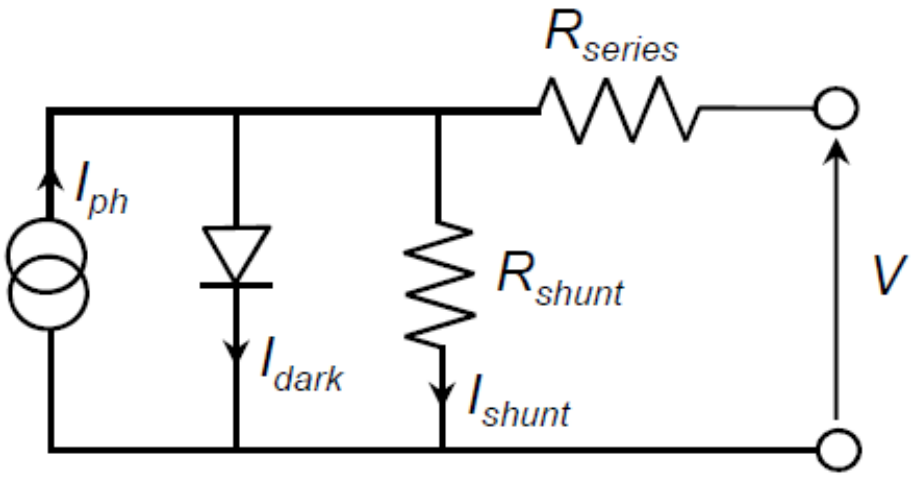

Figure 2.4 Schematic of circuit equivalent to solar cell.

From Figure 2.4 a shunt resistance R_{shunt} may arise from charge recombination in the photoactive layer and induce a shunting current I_{shunt} . The series resistance R_{series} includes sum of resistance at interface of electrodes, bulk resistance and sheet resistance of the transparent electrodes.

The total current measured is

$$I = I_{ph} - I_{dark} - I_{shunt} \quad (2.4)$$

2.2.2 Open Circuit Photo voltage (V_{OC})

Open-circuit voltage (V_{OC}) is measured when the circuit is broken or no external load is connected. Under this condition, there is no external current flows between the two terminals i.e. I = 0 and V = V_{OC}.

$$V_{oc} = \frac{mK_B T}{q} \ln\left(\frac{I_{ph}}{I_s} + 1\right) at\ I = 0 \quad (2.5)$$

V_{oc} increases logarithmically with photocurrent and light intensity.

2.2.3 Short-circuit current (I_{SC})

Short-circuit current (Isc) is measured under condition when the applied voltage is zero.

$$I_{sc} = I_{ph}\ at\ V = 0 \quad (2.6)$$

I_{sc} increases linearly with light intensity.

2.2.3 Solar to electric power conversion efficiency(η)

The performance of a solar cell device, is the percentage of power converted from absorbed light to electrical energy and collected, when DSSC device is connected to an electrical circuit. The fill factor (FF) is defined as

$$FF = \frac{V_m J_m}{J_{sc} V_{oc}} \quad (2.7)$$

where J_{SC} is the integral photocurrent density and V_{OC} is the open-circuit photovoltage.

Fill factor of DSC ranges from 0.6 to 0.8 subject to a device.

The solar to electric power conversion efficiency (η) is calculated from the ratio of the maximum extractable power point $P_m = V_m J_m$ to the incident solar power (P_{in}),

$$\eta = \frac{P_m}{P_{in}} = \frac{V_m I_m}{P_{in}} = \frac{J_{sc} V_{oc} FF}{P_{in}} \quad (2.8)$$

2.2.4 Measurement Set-up

The DSC device was measured at standard test condition with the incident light given by a solar simulator (100 mW/cm^2) using 450W Xenon lamp (LOT Oriel, USA) which is matched to the AM 1.5G sunlight irradiation. The spectral output of the Xenon lamp was calibrated with a

reference silicon photodiode equipped with an IR cut-off filter (PV Measurements Inc, USA) to reduce the mismatch in the region of 350- 750 nm between the simulated and the natural solar spectrum. The current and voltage were measured and controlled by a Keithley 2400 digital source meter (Keithley, USA). The DSSC active area was 1 cm^2.

2.3 Photoluminescence (PL)

Photoluminescence is non destructive spectroscopic technique used to study intrinsic and extrinsic properties of semiconductor nanostructures. [4] The band structure of semiconductor consists of the conduction band and valence band. The difference between the valence band and conduction band is called band gap energy (E_g). There can be sub bands in the band gap depending on the surface states and surface defects. There are four main photo-physical processes that occur in the semiconductor when excited by light with energy greater than the band gap of the semiconductor. Process 1 is the process in which electrons are excited from the valence band to the conduction band with simultaneous generation of holes (h^+) in the valence band under irradiation. The excited electrons (e^-) in the conduction band drop back to the valence band and recombine with the holes in a few nanoseconds. During the recombination process chemical energy is released and transformed to heat or light energy.[5] The light energy released is dissipated results in the luminescence emission of the semiconductor material called photoluminescence phenomena (PL). Process 2 is the band-band electron transition from conduction band bottom to valence band top releasing light as radiation where the photon energy is equal to band gap energy.

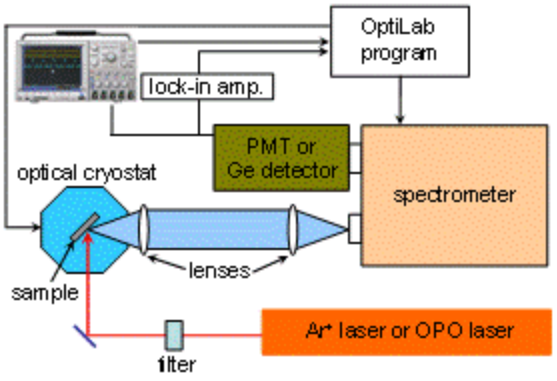

Figure 2. 5 Schematic of Photoluminescence Spectroscopy.

PL is used to analyze band discontinuities in the doped ZnO and TiO_2.

2.4 UV-Vis Spectroscopy

Many molecules absorb ultraviolet or visible light. The absorbance of a solution increases as attenuation of the beam increases. Absorbance is directly proportional to the path length, *b*, and the concentration, C, of the absorbing species. *Beer's Law* states that

$$A = \varepsilon bC$$

where ε the extinction coefficient of the dye in solution, C is the dye concentration on the sensitized film, and b is the path length.

UV-visible absorption spectra of solutions were measured in a 1 cm path length quartz cell on a Cary 5 spectrophotometer. The absorbance of sensitized TiO_2 films was measured by attaching the samples with double-sided tape to a sample holder with an aperture of 0.2 cm^2. The beam was then incident from the glass side. The dye loading, the amount of dye on the mesoporous films, was calculated from the absorbance of the sensitized film.

UV-Vis spectroscopy is used to calculate the amount of dye adsorbed on the ZnO, ZnO-TiO_2 and TiO_2 films.

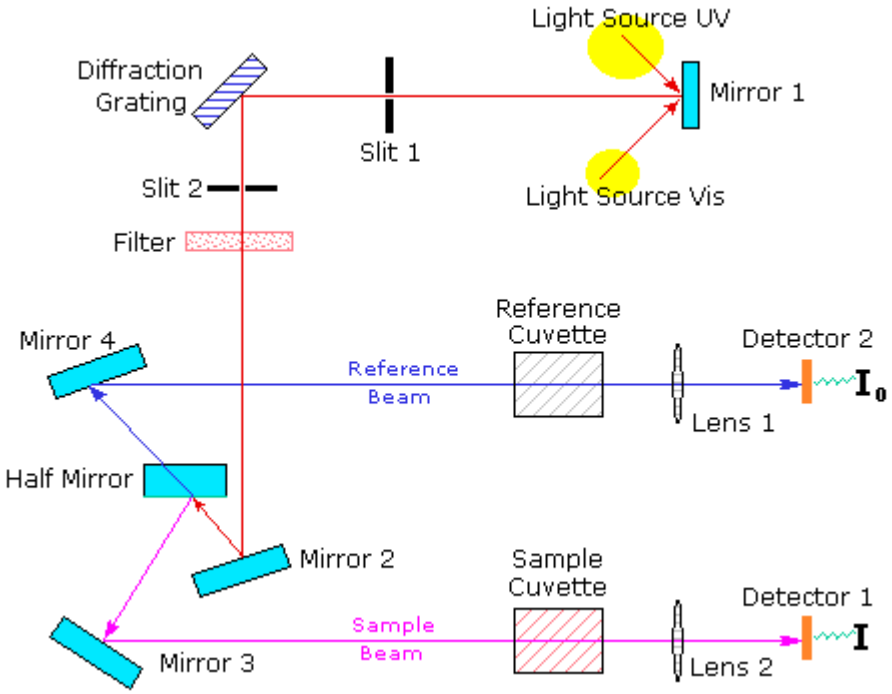

Figure 2. 6 Schematic of UV-Vis Spectroscopy.

2.5 Diffuse Reflectance

The band gap of semiconductor determines the application in photovoltaic, photoelectrochemical and optoelectronic devices. When light shines onto a powder sample, it is reflected in all directions, as shown in Figure 2. 7. Some of the light undergoes specular reflection at the powder surface. Due to the variety of powder shapes, it is reflected in many directions, unlike light reflected from a mirror. The remainder of the light is refracted as it enters the powder, where it is scattered due to internal reflection, reflection from the surfaces of other powder grains, or repeated refraction entry into the powder. Some of this scattered light is emitted back into the air.

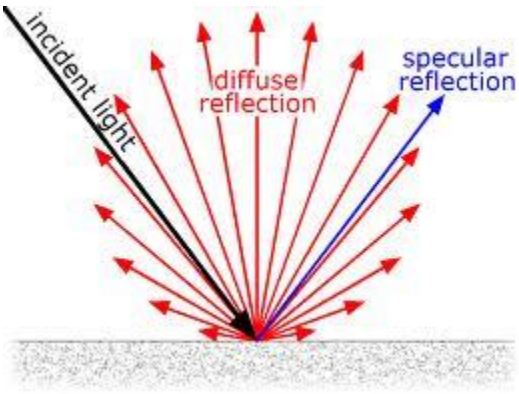

Figure 2. 7 Illustration of diffuse and specular reflection.

As the diffuse reflected light[6] is reflected or passed through the powder, light becomes weaker if absorption by the powder occurs. This results in a diffuse reflected spectrum. However, in regions where the powder exhibits strong absorption, most of the diffuse reflected light in long light path is absorbed, such that only the diffuse reflected light from short light path is emitted back into the air. Conversely, in bands of weak absorption, some light is not absorbed even in long light path and this diffuse reflected light is emitted to the air, resulting in stronger peaks than the transmission spectrum. In such a diffuse reflectance spectrum, the absorbed wavenumber positions are the same as the transmission spectrum. However, the relative intensity between peaks differs from the transmission spectrum because the weak peaks in the transmission spectrum become comparatively stronger in the diffuse reflectance spectrum. The Kubelka-Munk is used for comparison to transmission spectra or quantitative analysis.

The Kubelka-Munk model is used for the analysis of the band gap of the doped and undoped TiO_2 and ZnO. Kubelka –Munk[7] model is given by equation:

$$F(R) = (1-R)^2 / 2R$$

where R is the reflectance and F(R) is proportional to excitation coefficient(α)

Modified Kubelka–Munk function can be obtained by multiplying the F(R) function by hv, using the corresponding coefficient (n) associated with an electronic transition as follows

$$(F(R)\times \mathrm{h}\nu)^n$$

By ploting the above function as a function of eV, the band gap of the semiconductor is obtained. This technique is used due to high light scattering materials and absorbing nature of the nanorods.

Light emitted into the air from the powder contains specular reflection light, as well as diffuse reflected light. The specular reflection light must be reduced to obtain a more accurate diffuse reflectance spectrum. To achieve this, the particle size must be reduced. Reducing the particle size to a size equivalent to the wavelength is said to decrease the proportion of specular reflection light and maximize the scattering efficiency. The particle shape and packing status are other important factors, in addition to the particle size.

2.6 Transient photocurrent and photovoltage decay measurements

The DSSC efficiency is based on the competition between charge transport and recombination. Photoexcitation and charge separation ie electron injection and dye regeneration generates photocurrent, but recombination decreases the photocurrent by nullifying the charge carriers which increases with increasing electron density. Threfore recombination plays crucial role in the operation of the DSSC. The important kinetic factor called lifetime reflects the kinetics of recombination when cell is in operation. There are different techniques that can be used to analyze the electronic properties of the DSSC like impedance spectroscopy[8, 9], photovoltage decay[10, 11] and small amplitude step time transient decay[12, 13].

We adapted photovoltage decay and transient photocurrent measurements as they are easily performed when compared to impedance spectroscopy.

The photovoltage decay follows pseudo single exponential decay; the recombination rate constant is extracted from the sloped of the semi-logarithmic plot. As the recombination reaction follows first order reaction the electron lifetime is given by

$$K_{\mathrm{rec}} = 1/\tau_{\mathrm{e}}$$

Where K_{rec} the recombination is rate constant and τ_e is the electron lifetime.

The sample of the plot is shown in

Figure 2. 8 with the results.

Model	ExpDecay1		
Equation	y = y0 + A1*exp (-(x-x0)/t1)		
Reduced Chi-Sqr	2.83062E-7		
Adj. R-Square	0.96582		
		Value	Standard Error
C	y0	0.08455	4.97252E-6
C	x0	0.002	0
C	A1	0.37378	0.00408
C	t1	0.03422	1.11184E-4

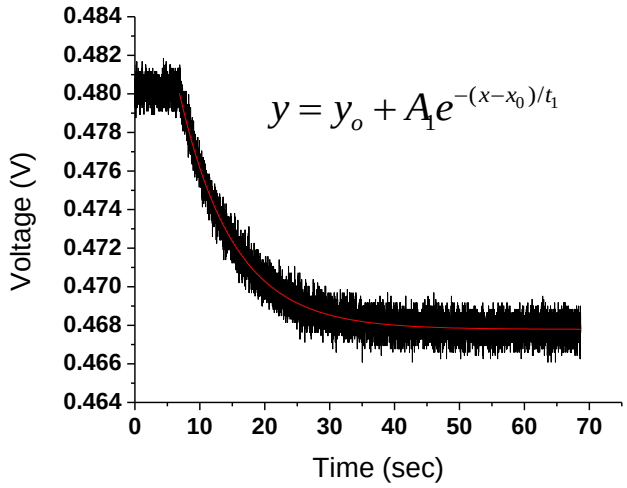

Figure 2. 8 Photovoltage decay plot.

The experiments can be done in short circuit condition monitoring the photocurrent decay and the time constant extracted is the electron transport time (τ_r). The photocurrent decay transport process is very fast compared to photo voltage decay.

The electron diffusion coefficient D_n can be obtained the electron transport time τ_r by three dimensional diffusion model given by equation.[14]

$$D_{\mathrm{n}} = d^2 / 2.77\tau_{\mathrm{r}}$$

where d is the thickness of the semiconductor film.

The average diffusion length L_{n} the average distance an electron travels before nullifying by recombination is given by the below equation. [9]

$$L_{\mathrm{n}} = \sqrt{D_{\mathrm{n}}}\tau_{\mathrm{e}}$$

If L_{n} is greater than thickness of the film good efficiencies can be obtained in DSSC.

The experimental set-up consist of the white bias light is illuminated on the device for a certain time to a steady voltage and then turned off. At the same time, the open-circuit voltage decay of the device is recorded. Typically, the interval of the measurement is set in a logarithmic scale, ranging from 100 μs to seconds. The decay data is fitted by a quadruple exponential model and then differentiated against time. Oscilloscope is used due to rapid decay faster than 0.1 ms. Voltage change about the V_{oc} of the cell under the white bias light produced by using a white light emitting diode and measuring the voltage decay process. The solid state fast switch is used for pulsing the light at fixed intervals.

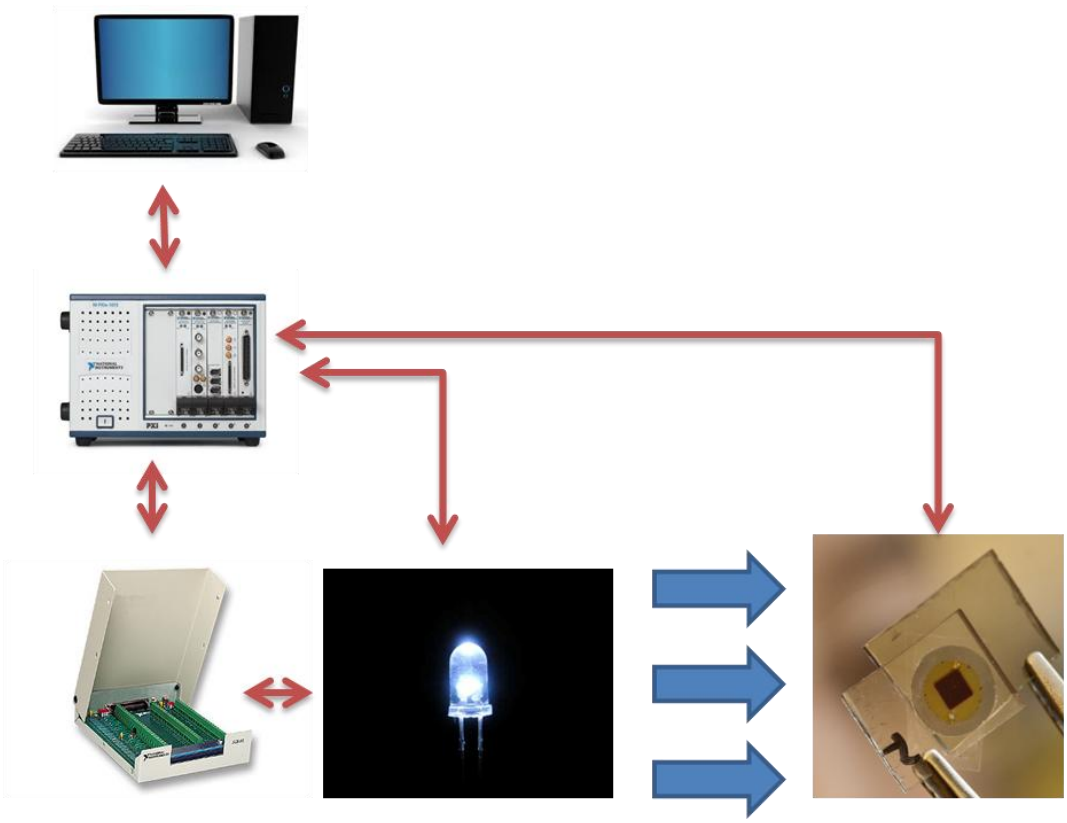

Figure 2. 9 Schematic of the set-up for photo voltage decay measurements.

2.7 SEM

In scanning electron microscopy (SEM), an electron beam is used to map the surface of a specimen. An electron beam with energy of some keV is emitted by a cathode (gun) and focused by condenser lenses. The beam is used to scan a rectangular area of the specimen line-by-line. The electrons interact with the atoms at or near the sample surface depending on the acceleration voltage. Back-scattered or secondary electrons are detected by specialized detectors. This signal is amplified and yields a magnified black and white image of the sample surface with resolutions in the nm range and below. Different grey scale values in the SEM image arise from differences in the electron densities of the materials. Elements of higher atomic number appear brighter than those of lower atomic number.

2.8 XRD

X-ray diffraction (XRD) is one of the most important non-destructive tools to analyze all kinds of matter—ranging from fluids, to powders and crystals. XRD is an indispensable method for materials characterization and quality control. XRD is used to characterize the phase composition and percent crystallinity in doped and undoped materials.

Brags Law $n\lambda = 2d\sin\theta$

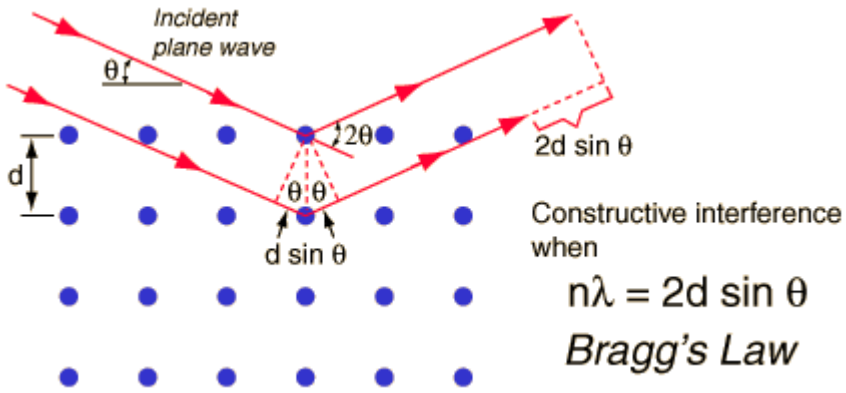

Figure 2. 10 Schematic of X-ray diffraction

Scherrer equation is used to obtain the crystal size. [15]

$$D = 0.89\lambda / B\cos\theta$$

where D is the crystallite size is the wavelength of the X-ray and θ is the diffraction angle.

2.9 ICP-MS

Inductively Coupled Plasma Mass Spectrometry or ICP-MS is an analytical technique used for elemental determinations. It offers the advantage of multi element detection, high sample throughput and isotropic analysis. ICP has a high temperature atomizing ion source which provides temperature of 5500°C which no material can withstand. The data acquired from the plasma source corresponds to total amount of element in the sample. The elemental response is unaffected by the presence of multi-element species. Mass spectra in mass/charge is obtained, using argon as the transport gas provides the highest collision rate available due to high ion density of Ar^+ and e^-.[16] The sample is dissolved in HNO_3 due to solvent tolerance as presence of salts can clog and contaminate the instrument.[17] The standard of the instrument is set by using standard addition to matrix like volatile acid. ICP-MS is used for the analysis of the ZnO seed loading on the FTO substrate.

2.10 Atomic Layer Deposition

Atomic layer deposition provides uniform conformal coating on high aspect ratio nanostructures. ALD works on alternative pulsing of the precursor gases and vapors on the substrate surface and successive chemisorption and surface reaction of the precursors.[18] The reactor is purged with inert gases between pulses. The growth is stable and thickness of each deposition cycle is constant. ALD has the advantage of growing thin films with precise thickness and for large area industrial applications.[19] ALD also has the advantage of depositing different multilayers on the same substrate. Precursors play an important role in ALD, as must chemisorb on the surface or react rapidly with the surface groups and react aggressively with each other.[20] The aggressive reaction can lead to saturation in short time, giving reasonable growth rate. Large negative ΔG values are favaorable for ALD. ALD is widely used in electronics industry for the manufacturing

integrated circuits.[21] ALD layers of TiO_2 are deposited on ZT films as barrier layers to prevent recombination in DSSC, due complete coverage of the barrier layer.

2.11 References

1. P. Wang, S. M. Zakeeruddin, P. Comte, R. Charvet, R. Humphry-Baker, and M. Grätzel, "Enhance the Performance of Dye-Sensitized Solar Cells by Co-grafting Amphiphilic Sensitizer and Hexadecylmalonic Acid on TiO_2 Nanocrystals," *The Journal of Physical Chemistry B,* 107[51] 14336-41 (2003).
2. V. Manthina, J. P. Correa Baena, G. Liu, and A. G. Agrios, "ZnO–TiO_2 Nanocomposite Films for High Light Harvesting Efficiency and Fast Electron Transport in Dye-Sensitized Solar Cells," *The Journal of Physical Chemistry C,* 116[45] 23864-70 (2012).
3. T. W. Hamann, O. K. Farha, and J. T. Hupp, "Outer-Sphere Redox Couples as Shuttles in Dye-Sensitized Solar Cells. Performance Enhancement Based on Photoelectrode Modification via Atomic Layer Deposition," *The Journal of Physical Chemistry C,* 112[49] 19756-64 (2008).
4. J. Liqiang, Q. Yichun, W. Baiqi, L. Shudan, J. Baojiang, Y. Libin, F. Wei, F. Honggang, and S. Jiazhong, "Review of photoluminescence performance of nano-sized semiconductor materials and its relationships with photocatalytic activity," *Solar Energy Materials and Solar Cells,* 90[12] 1773-87 (2006).
5. M. I. Litter, "Heterogeneous photocatalysis: Transition metal ions in photocatalytic systems," *Applied Catalysis B: Environmental,* 23[2–3] 89-114 (1999).
6. G. Kortüm, W. Braun, and G. Herzog, "Principles and Techniques of Diffuse-Reflectance Spectroscopy," *Angewandte Chemie International Edition in English,* 2[7] 333-41 (1963).
7. M. F. Kubelka P *Ein Beitrag zur Optik der Farbanstriche Z. Tech. Phys.,* 12 (1931).

8. F. Fabregat-Santiago, J. Bisquert, E. Palomares, S. A. Haque, and J. R. Durrant, "Impedance spectroscopy study of dye-sensitized solar cells with undoped spiro-OMeTAD as hole conductor," *Journal of Applied Physics,* 100[3] - (2006).

9. J. Bisquert, F. Fabregat-Santiago, I. n. Mora-Seró, G. Garcia-Belmonte, and S. Giménez, "Electron Lifetime in Dye-Sensitized Solar Cells: Theory and Interpretation of Measurements," *The Journal of Physical Chemistry C,* 113[40] 17278-90 (2009).

10. A. Zaban, M. Greenshtein, and J. Bisquert, "Determination of the Electron Lifetime in Nanocrystalline Dye Solar Cells by Open-Circuit Voltage Decay Measurements," *ChemPhysChem,* 4[8] 859-64 (2003).

11. S. Ito, R. Humphry-Baker, P. Liska, P. Comte, #233, P. chy, M. K. Nazeeruddin, Gr, #228, and M. tzel, "Electron-Density and Electron-Lifetime Profile in Nanocrystalline-TiO_2 Electrode of Dye-Sensitized Solar Cells Analysed by Voltage Decay and Charge Extraction," *ISRN Nanotechnology,* 2011 5 (2011).

12. J. Nissfolk, K. Fredin, J. Simiyu, L. Häggman, A. Hagfeldt, and G. Boschloo, "Interpretation of small-modulation photocurrent transients in dye-sensitized solar cells – A film thickness study," *Journal of Electroanalytical Chemistry,* 646[1–2] 91-99 (2010).

13. S. Nakade, T. Kanzaki, Y. Wada, and S. Yanagida, "Stepped light-induced transient measurements of photocurrent and voltage in dye-sensitized solar cells: Application for highly viscous electrolyte systems," *Langmuir,* 21[23] 10803-07 (2005).

14. S. H. Kang, S. H. Choi, M. S. Kang, J. Y. Kim, H. S. Kim, T. Hyeon, and Y. E. Sung, "Nanorod-Based Dye-Sensitized Solar Cells with Improved Charge Collection Efficiency," *Advanced Materials,* 20[1] 54-58 (2008).

15. A. L. Patterson, "The Scherrer Formula for X-Ray Particle Size Determination," *Physical Review,* 56[10] 978-82 (1939).

16. S. J. Ray, F. Andrade, G. Gamez, D. McClenathan, D. Rogers, G. Schilling, W. Wetzel, and G. M. Hieftje, "Plasma-source mass spectrometry for speciation analysis: state-of-the-art," *Journal of Chromatography A*, 1050[1] 3-34 (2004).

17. A. A. Ammann, "Inductively coupled plasma mass spectrometry (ICP MS): a versatile tool," *Journal of Mass Spectrometry*, 42[4] 419-27 (2007).

18. T. Suntola, "Atomic layer epitaxy," *Materials Science Reports*, 4[5] 261-312 (1989).

19. M. Ritala, M. Leskelä, J. P. Dekker, C. Mutsaers, P. J. Soininen, and J. Skarp, "Perfectly conformal TiN and Al2O3 films deposited by atomic layer deposition," *Chemical Vapor Deposition*, 5[1] 7-9 (1999).

20. M. Leskelä and M. Ritala, "Atomic layer deposition (ALD): from precursors to thin film structures," *Thin Solid Films*, 409[1] 138-46 (2002).

21. M. Ritala, K. Kukli, A. Rahtu, P. I. Räisänen, M. Leskelä, T. Sajavaara, and J. Keinonen, "Atomic layer deposition of oxide thin films with metal alkoxides as oxygen sources," *Science*, 288[5464] 319-21 (2000).

Chapter 3
Number Density and Diameter Control of Chemical Bath Deposition of ZnO Nanorods on FTO by Forced Hydrolysis of Seed Crystals

Abstract

ZnO nanorods have been studied extensively due to facile synthesis and useful optoelectronic properties for applications in nanoscale devices. In a common two-step procedure, an ethanolic Zn^{2+} precursor solution is used to deposit ZnO seed crystals on a substrate, which is then immersed in an aqueous Zn^{2+} precursor solution to grow the nanorods. Here, a forced hydrolysis technique was employed based on additions of water and heat to the seed precursor solution before depositing the seeds on commercial FTO/glass substrates. ZnO nanorods were then grown from these seeds by chemical bath deposition. Analyses showed that the forced hydrolysis resulted in an increase in seed crystallite size and a decrease in the number of seeds deposited. With increasing seed size, the number density of nanorods decreased, while the length and diameter of each rod increased. These findings offer a simple method for exerting control over the number density of ZnO nanorods that is compatible with the rough FTO surface, unlike other methods that require smoother substrates.

3.1 Introduction

ZnO is a functional material with many applications due to its electrical,[1] photochemical,[2] thermoelectric,[3] piezoelectric[4, 5] and optical[6] properties. ZnO can be grown into wide variety of nanostructures like nanoparticles, nanorods, nanowires, nanobelts, nanotubes and so forth due to its anisotropic growth and ease of crystallization. One-dimensional growth of ZnO is studied extensively due to its potential use in solar cells[7, 8], chemical sensors,[9] field effect transistors,[10] light emitting diodes,[11] piezoelectric nanogenerators,[12] and laser diodes.[13]

Many useful properties of ZnO nanorods are dependent on the rod diameter, length and number density. The surface band bending of the ZnO nanorods is dependent on the diameter of the ZnO nanorods.[14, 15] The performance of the photoelectrochemical cells for water splitting and photovoltaics depends on the rod morphology.[3, 16] In hybrid solar cells, a low density of ZnO nanorods on the photoanode is needed to provide void space for P3HT:PCBM infiltration.[17] For applications in surface acoustic wave devices growth along the *a*-axis is required.[18] In the fabrication of composite nanostructures such as nanoparticle-coated ZnO nanorods, tuning the density of the nanorods is required for balancing total surface area against effective coverage of the nanoparticles throughout the length of the nanorod.[19, 20, 21] The optoelectronic and gas sensing properties of the ZnO is dependent on the shape of nanostructures.[22]

ZnO nanorods can be grown in situ from a variety of substrates through procedures such as chemical bath deposition,[23, 24] electrodeposition,[25, 26, 27] chemical vapor deposition,[28, 29] thermal deposition[30] and pulse laser deposition.[31] Among these chemical bath deposition (CBD) has the advantage of being low temperature, low cost, suitable for large area processing for industrial applications, and environmentally benign. CBD is a two-step process, beginning with the deposition of a "seed layer" of ZnO nanocrystals on the substrate, from which nanorods are subsequently grown in the "chemical bath", an aqueous solution of a zinc precursor with additives to modify the growth.

In CBD, increasing the concentrations of precursors in the chemical bath increases both nanorod diameter and length, but has little effect on the number density of the rods. As precursor concentrations are

increased, this results in the rods fusing together. To obtain larger rods while maintaining space between them, control over the number density is required. Some density control has been achieved by controlling the thickness of seed layers made by physical methods such as sputtering.[32] Other methods have been devised that work on smooth surfaces like ITO,[33] glass, and Si substrates,[32] but we have found them ineffective on the rougher surface of FTO, which is preferred to ITO in applications requiring tolerance of high temperatures. Here, we show how the deposition of seed crystals on FTO from an ethanolic precursor solution can be modified by low-temperature thermal treatment combined with controlled additions of water to yield control over the number density of the resulting ZnO nanorods.

3.2 Experimental Procedure

Reagents and Materials. Zinc nitrate hexahydrate, hexamethylenetetramine (HMTA), polyethyleneimine and ethanol were purchased from Sigma-Aldrich (USA) and were ACS grade. N719 was purchased from Dyesol (Australia). SnO_2: F glass (FTO, transmission> 80% in the visible spectrum; sheet resistance 8 Ω /□) was purchased from Hartford Tec Glass (USA).

ZnO Seed Crystal Preparation. The formation of ZnO seeds began with the dissolution of 5 mM zinc acetate dihydrate in ethanol by stirring for 3 hours at room temperature.[34] Varying amounts of deionized water were added. The solution was stirred for another 3.5 hours and then transferred into preheated oven at 80˚C for 12 hours. After cooling to room temperature, this finished seed precursor solution was drop-cast on a precleaned FTO substrate, which was allowed to dry for 30 seconds and then rinsed with ethanol. The substrate was then heated on a titanium hot plate at 350°C for 20 minutes to form the ZnO seed layer. The procedure was repeated two additional times to increase the number of seeds on the substrate.

ZnO Seed Crystal aging. In this experiment, the seed precursor solution was allowed to stand for 24 hours to see the effect of aging on the resulting seeds and nanorods. Then the seed solution is deposited

on a precleaned FTO substrate and heated on a titanium hot plate at 350°C for 20 minutes to form a ZnO seed layer.

ZnO Nanorod Synthesis. Nanorods were grown from the ZnO seeds by chemical bath deposition. The seeded FTO substrates were placed in 100 mL of an aqueous solution of 50 mM zinc nitrate hexahydrate and hexamethylenetetramine and 6mM polyethyleneimine in a 100-ml glass bottle at 90°C for 24 hours.

Characterization. The morphology of ZnO seed crystals and nanorods was investigated by scanning electron microscopy (FEI Quanta FEG250 SEM in High vacuum mode) and characterized by X-ray powder diffraction (XRD) using a Bruker D8 Advance X-ray diffractometer using Cu K_radiation (λ = 0.154178 nm) at a scanning rate of 0.04˚ s^{-1} in the 2θ range from 10˚ to 90˚. The data were analyzed using the Debye-Scherrer equation to determine the ZnO seed particle size. Photoluminescence measurements were performed using a Horbia Jobin Yvon Fluorolog-3 spectroflourometer with an excitation wavelength of 350 nm and a scan rate of 1 nm/s.

Zn Quantification. ZnO-seeded FTO substrates were etched for 6 h with 1% HNO_3(aq) to dissolve the zinc. No seeds could be seen by SEM after this etching step. The etched zinc solution was kept in polypropylene vials (Corning Centristar) and analyzed by inductively coupled plasma–mass spectrometry (ICP–MS) using an Agilent Technologies 7700 series instrument run in He mode and in a matrix of 1% HNO_3(aq).

3.3 Results

3.3.1 Forced Hydrolysis of ZnO seeds.

Typical chemical bath deposition of ZnO nanorods begins with the formation of small (2 to 3 nm) seed crystals of ZnO by distributing a zinc(II) salt on a substrate, then heating it in air. We increased the size of the seeds by forced hydrolysis: the addition of controlled amounts of water to the ethanolic solution of zinc(II) acetate dihydrate followed by heating.[35]

Hydrolysis forms zinc hydroxides by the following stoichiometry:[36]

$Zn(CH_3COO)_2 + 2H_2O \rightarrow HO—Zn—OH + 2CH_3COOH$

Crystal growth of ZnO can be visualized as $Zn(OH^-)_4^{2-}$ ions gathering into zinc oxyhydroxy clusters.[37]

In this work, the concentration of water added to the seed precursor solution, $[H_2O]_{SPS}$, was varied from 0 M to 1 M. It should be noted that even without added water, some water is always present from the zinc acetate dihydrate salt.

SEM images of ZnO seed crystals deposited on FTO are shown in Figure 3. 1. It can be seen that as $[H_2O]_{SPS}$ was increased from 0 M to 1 M, the size of the seeds increased while the number of seeds decreased. Note that the larger-scale features in the SEM images are from the roughness of the FTO surface. From Figure 3. 1 c and d we can see the seeds in the circles, where the density of the seeds decreased with the increase of concentration.

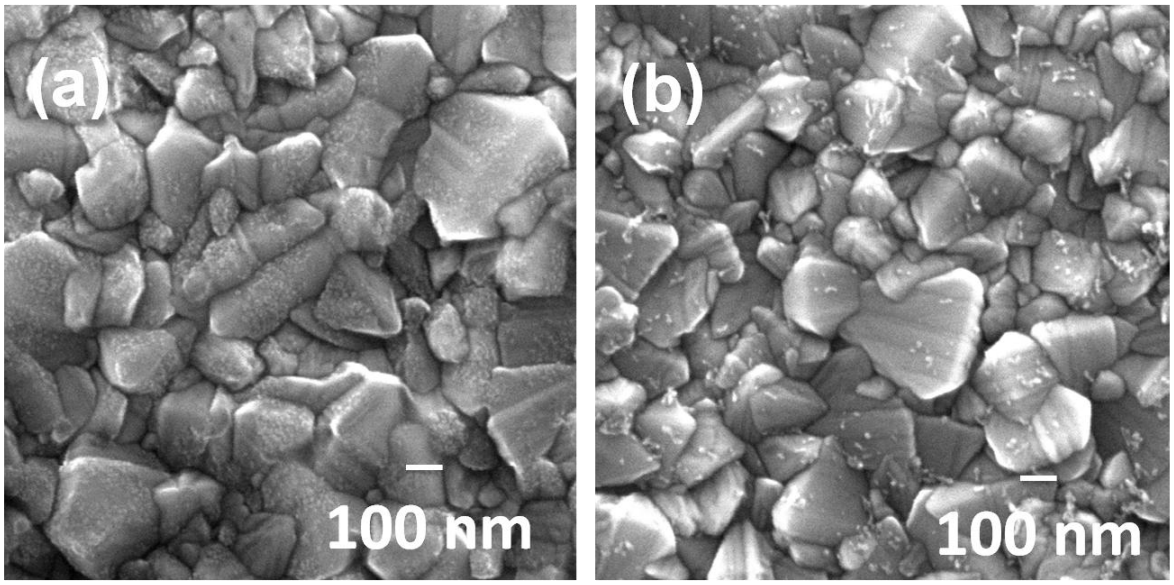

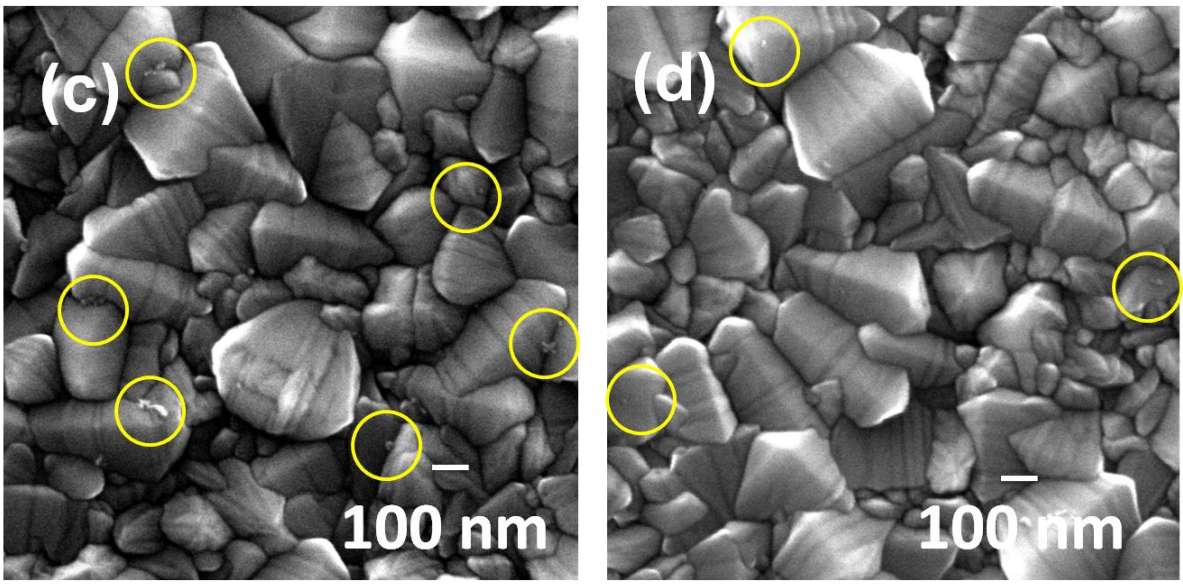

Figure 3. 1 SEM Image of ZnO seeds on the FTO substrate with different concentrations of water (a) 0 M, (b) 0.5 M, (c) 0.8 M and (d) 1 M.

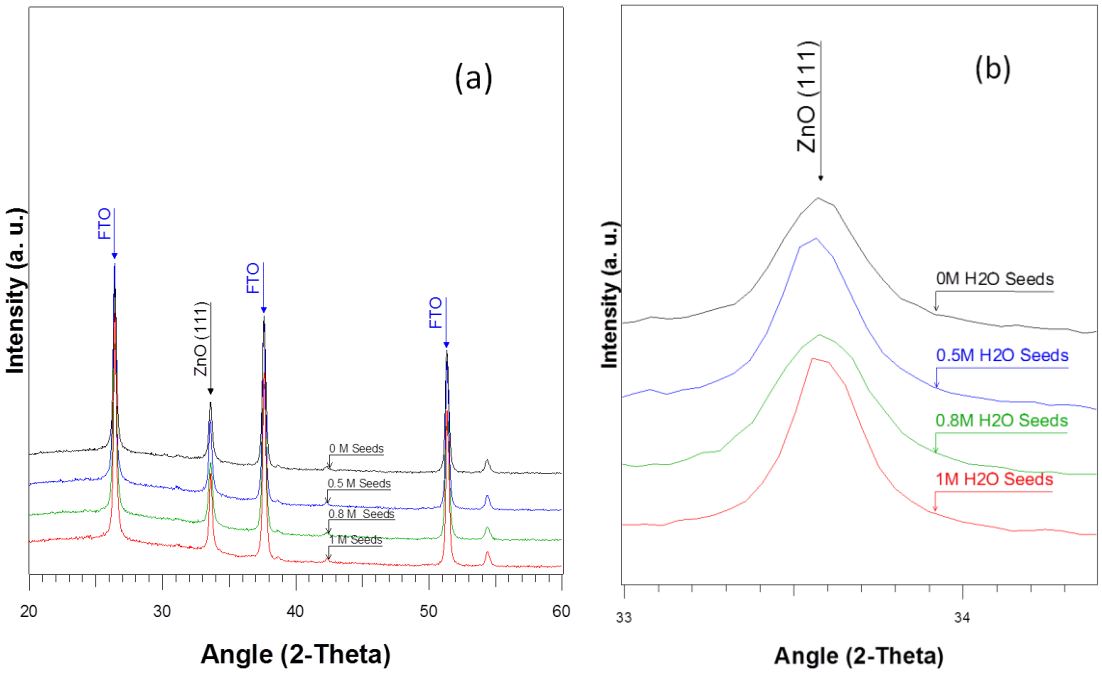

Figure 3. 2. (*top*) X-ray diffraction pattern of ZnO nanoseeds on fluorine doped tin oxide (FTO) substrate, (*bottom*) X-ray diffraction pattern of ZnO (111) peak.

The properties of the seeds were examined by powder X-ray diffraction data, presented in Figure 3. 2. All diffraction peaks can be attributed either to the FTO substrate or to crystalline ZnO (space group: P63*mc*(186); a=0.3249 nm, c=0.5206 nm), in agreement with the standard pattern for ZnO (JCPDS 065-2880). For seeds made using increasing amounts of water, the degree of peak broadening decreases, indicating larger crystallite sizes.

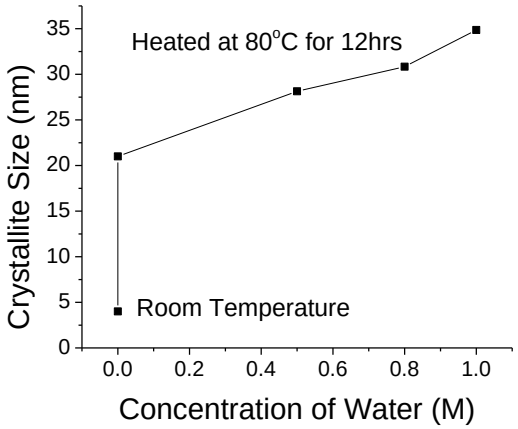

Figure 3. 3 Change in the crystal size (by XRD) with the concentration of the water.

We calculated crystallite size based on the full width at half maximum (FWHM) of the XRD peak for ZnO(111) using the Scherrer equation, with the results shown in Figure 3. 3. When seeds were prepared with neither added water nor heat treatment, the resulting size of the seeds was 4-5 nm. Heating the seed solution in an 80 °C oven for 12 h increased the seed size to 25 nm. Addition of water further increased the seed size to as much as 35 nm for a seed precursor solution with 1 M water.

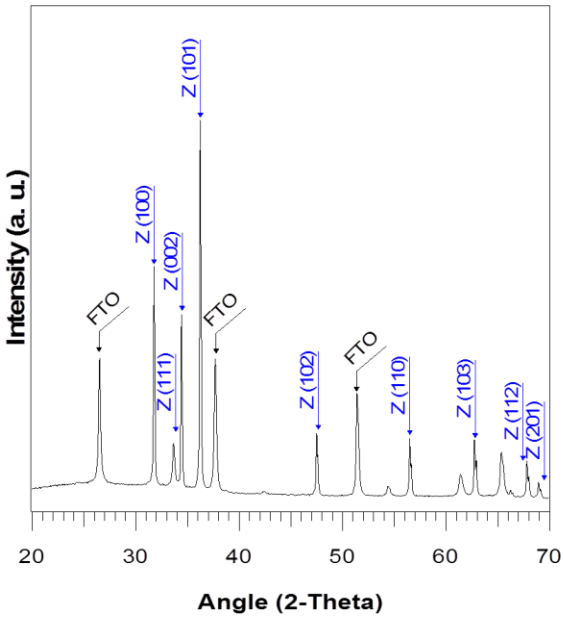

Figure 3. 4 X-ray diffraction pattern of ZnO nanorods on fluorine doped tin oxide (FTO) substrate.

ZnO nanorods were grown on the ZnO-seeded FTO substrates described in the preceding section by immersing them in an aqueous chemical bath for 24 h at 90 °C. XRD data for the nanorods on FTO are shown in Figure 3. 4. All diffraction peaks can be attributed to FTO or to wurtzite ZnO, in agreement with the standard pattern for 1-D ZnO (JCPDS 070-8070). The intensity of the peak assigned to the (002) plane indicates that ZnO nanorods were formed through elongation along the *c*-axis perpendicularly to the substrate.

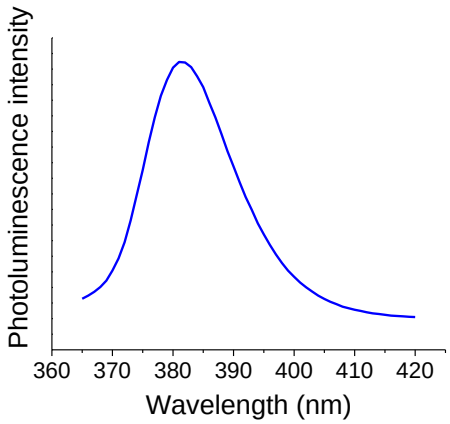

Figure 3. 5 Room temperature Photoluminescence of ZnO nanorods.

Optical characterization by photoluminescence spectroscopy (see Figure 3. 5 Room temperature Photoluminescence of ZnO nanorods.)indicates bandgap excitation similar to bulk ZnO at 380 nm, indicating no quantum confinement effects. The atom ratio of Zn:O (0.99:1), analyzed by energy dispersive X-ray spectroscopy, equals the stoichiometric ZnO ratio.

SEM images (Figure 3. 6) of the samples produced by chemical bath deposition confirm that the ZnO grew grown in nanorod morphology under all tested concentrations of water in the seed precursor solution, in agreement with the XRD data. The diameter, length, and number density of the nanorods were determined from these images. Both the diameter (Fig. 7(a)) and length (Fig. 7(b)) of the nanorods increased monotonically with increasing water concentration in the seed precursor solution (i.e., with larger ZnO seeds), while the number of nanorods per unit area decreased.

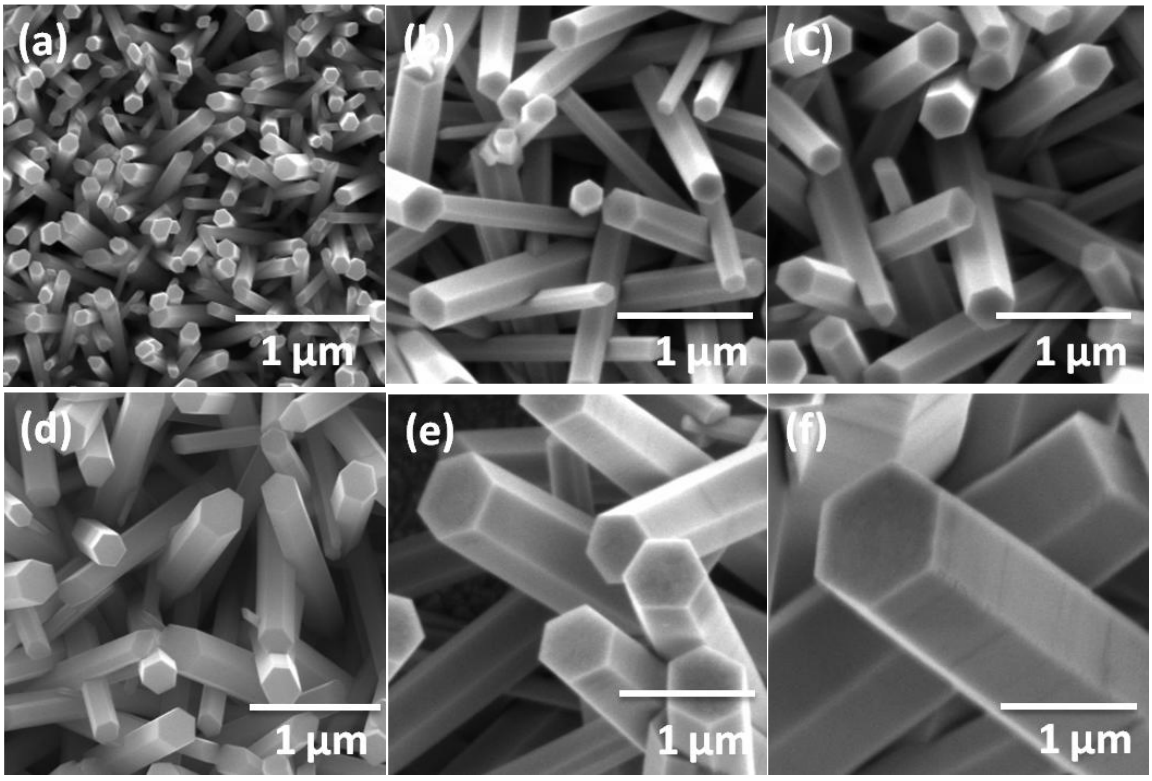

Figure 3. 6 SEM Images of ZnO nanorods grown on FTO substrate with different concentrations of water in seed solution (a) 0 M (b) 0.5M, (c) 0.6M, (d) 0.7M, (e) 0.8M, (f) 0.9M .

3.3.2 ZnO Seed Quantification

The amount of zinc on ZnO-seeded FTO substrates was quantified by dissolving the zinc as Zn^{2+} in water with 1% nitric acid and analyzing the zinc by ICP–MS. Although equal amounts of seed solution are drop-cast on each substrate, the subsequent ethanol rinse means that the amount of Zn remaining on the substrate can vary. Assuming that all Zn came from ZnO seed crystals, taking the XRD crystallite size as the amount of Zn etched from each seeded sample decreased with increasing amounts of water in the seed precursor solution. Seed size increases along the same trend, and the net result is a decreasing number density of seed crystals as water is added to the precursor solution. The typical seed crystal size, and assuming spherical crystals, we estimated the number density of seed crystals on each substrate. Our analyses showed that the amount of Zn etched from each seeded sample decreased with increasing amounts of water in the seed precursor solution. Seed size increases along the same trend, and the net result is a decreasing number density of seed crystals as water is added to the precursor solution. The results are shown in Table 1. For comparison, the number density of nanorods grown from a given seed layer preparation is also given. Clearly, each seed does not become a nanorod, but the number of nanorods correlates to the number of seeds.

Table 3.1 Density of seeds with different water concentrations in seed solution.

Concentration of water added to seed solution (M)	Amount of ZnO loaded ($\mu g/cm^2$)	Density of seeds (μm^{-2})	Density of nanorods (μm^{-2})
0	1.64 ± 0.11	651 ± 45	20.1
0.5	0.97 ± 0.20	210 ± 44	3.21
0.8	0.42 ± 0.03	65.3 ± 4.1	1.01
1.0	0.30 ± 0.03	29.4 ± 3.2	0.203

3.4 Discussion

3.4.1Density of ZnO nanorods

Seeds are used before the crystal growth of the nanorod to promote heterogeneous nucleation as homogenous nucleation requires a high activation energy barrier. Thus seeds allow crystal growth to take place at a low saturation ratio.[38] The seed layer is of crucial importance in determining the type of morphology and the dimensions of ZnO nanostructures grown by chemical bath deposition.[39] In this work, the seeds were altered by the addition of varying amounts of water in the ethanolic seed precursor solution. The seed size increases as more water is added, presumably by accelerating the hydrolysis of zinc acetate to form ZnO. In addition, the addition of water increases the polarity of the precursor solution, which is known to affect the morphology of crystals formed by homogeneous nucleation.[40]

The number density of the nanorods is obtained from the corresponding SEM images (Figure 3. 6). The number density decreased sharply with the addition of 0.5 M H_2O to the ethanolic seed precursor solution, compared to a sample made with no added water. Further additions of water resulted in modest reductions in the rod number density. Water leads to a smaller number density of seed crystals, which could be expected to result in a lower number of nanorods. Notably, however, the seeds greatly outnumber the rods as was shown in Table 1. According to the nucleation theory, ZnO nanorods nucleate at the seed/solution interface. The nucleation process occurs on the free surface or the grain boundary in between the ZnO seed nanoparticles.[32, 41, 42, 43, 44] The nucleation process depends on the diameter and orientation of the ZnO seed nanoparticles.[42] Our results conclude that grain boundary nucleation between two ZnO grains in the ZnO seed layer is the mechanism for the growth of the ZnO nanorods in agreement with previous reports.[45]

Reports on ZnO nanorods grown from sputtered seed layers have given contradictory results.[46] Ghayour et al indicated a decrease in nanorod number density with increasing thickness of the seed layer.[47] Liu et al, on the other hand, found sharply increasing rod density with seed layer thickness for thin seed layers (< 3.5 nm).[29] Using solution-processed seed layers, Ma et al. could alter the nanorod density by adjusting

the concentration of the seed precursor solution and the rotational speed of spin-coating used to deposit it.[33] We are not aware of any prior work using forced hydrolysis of the seeds to adjust nanorod density.

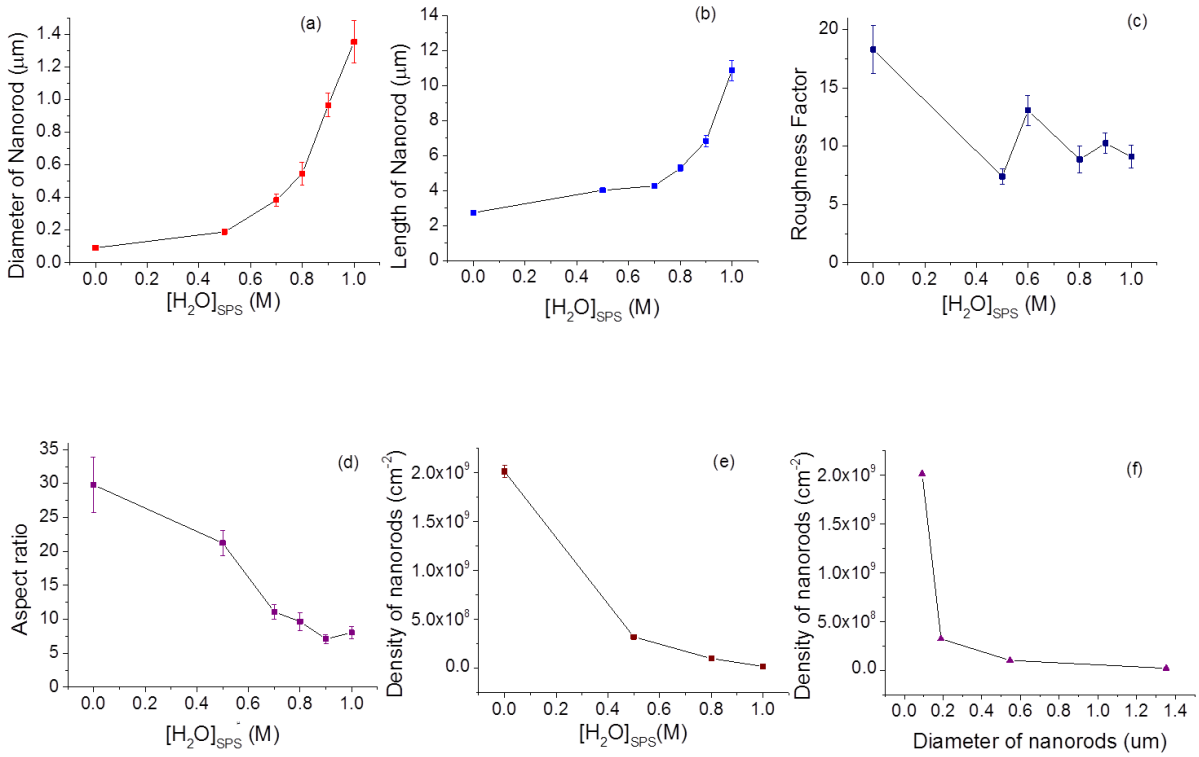

Figure 3. 7 Variation of (a) diameter, (b) length, (c) roughness factor and (d) aspect ratio (e) density of ZnO nanorods versus water concentration in the seed precursor solution; (f) correlation between the density and the diameter of the ZnO nanorods

3.4.2 Nanorod morphology

In chemical bath deposition ZnO nanorod growth is limited by mass transport of the ions in the precursor solution.[48] The average diameter and length and of the nanorods obtained from the corresponding SEM images are plotted in Figure 3. 7(a,b). We have seen an increase in the diameter and length with decreasing density of the ZnO nanorods (see Fig. 7). Our results are in agreement with previous reports that diameter of the nanorod increases with increasing seed size[49] and decreasing seed density.[49, 50]

From the SEM images of the ZnO nanorods we can see how the size of the seed can change the nature of the nucleation by introducing completely different dimensions of the nanorods. The larger size of the nucleus with well formed crystal orientation can induce faster growth rate. Thus in our analysis we can see the increase in length and diameter of the ZnO nanorods for ZnO seeds with larger diameter in agreement with previous report.[51]

This trend has been explained by theoretical modeling. In the work of Boercker et al.,[48] when seeds were deposited over a defined rectangular area, rods that grew at the edge of the rectangle were much longer and wider than those at the center. This was explained by modeling based on nanorod growth being limited by mass transport of Zn^{2+} from the bulk solution, with the diffusion layer much larger than the rod length. Rods in the center of the rectangle grew in an area of depressed precursor concentration, while those at the edge had close access to bulk solution. In the present results, a high density of growing nanorods depresses the steady-state concentration of Zn^{2+} at the location of the rods, while a lower density of nanorods results in higher local $[Zn^{2+}]$ and higher growth rates at each rod.

Figure 3. 7 c and d show how the roughness factor (surface area per projected area, calculated from the nanorod dimensions and number density) and aspect ratio (length divided by diameter) change as a function of $[H_2O]_{SPS}$, the concentration of water added to the seed precursor solution. The changes in nanorod diameter and length are not proportional to each other, as the aspect ratio decreases monotonically with increasing $[H_2O]_{SPS}$. However, the roughness factor, after decreasing by a about a factor of two for 0.5 M water versus no added water in the seed precursor solution, stays roughly constant with $[H_2O]_{SPS}$ for $0.5\ M \leq [H_2O]_{SPS} \leq 1.0\ M$. This is to say that with further additions of water beyond 0.5 M to the seed precursor solution, the resulting increase in rod size approximately compensates for the decrease in rod number density to maintain about the same surface area of ZnO nanorods per area of substrate. The decrease in the density of the ZnO nanorods with the increase in the size of the seeds is due to decrease in the density of the grain boundaries with the increase in the size of the particle.

3.4.3 The effect of ZnO Seed Solution aging on the ZnO nanorod growth

After 24 h of aging the seeds aggregated to form spherical particles about 800 nm in diameter (see Figure 3. 8(a)). This can be attributed to collision coalescence of ZnO crystallites forming misoriented attachments that fail to re-orient themselves due to the low driving force at room temperature.[52] Instead of a single large crystal, the result is a large agglomeration of crystallites. The many different exposed facets on the exterior of this seed provide multiple nucleation sites, resulting in radial growth of nanorods. Growth of ZnO from these seeds by the usual chemical bath deposition produced starburst (Figure 3. 8(b)) and ball (Figure 3. 8(c)) shapes. Thus, heating and addition of water accelerate the growth of ZnO nanoseeds and result in separate nanorods with reduced density, whereas extended aging at room temperature instead produces agglomerates that result in 3-D nanorod arrays. Each seed will have multiple nucleation sites resulting in 3-D array of nanorods. Ball shaped 3-D structures as shown in Figure 3. 8(c) are reported previously on sputtered seeds using Al^{3+} as additive.[53] The average diameter of the 3-D ball shaped structures is 20 µm. These 3-D ball structures can be widely applied in optoelectronics due to the optical properties.[54] 3-D nanoballs are used in applications like UV lasers and LED for their emission.[55] This technique induces low cost easy fabrication of the sensors, lasers and LED. [56, 57]

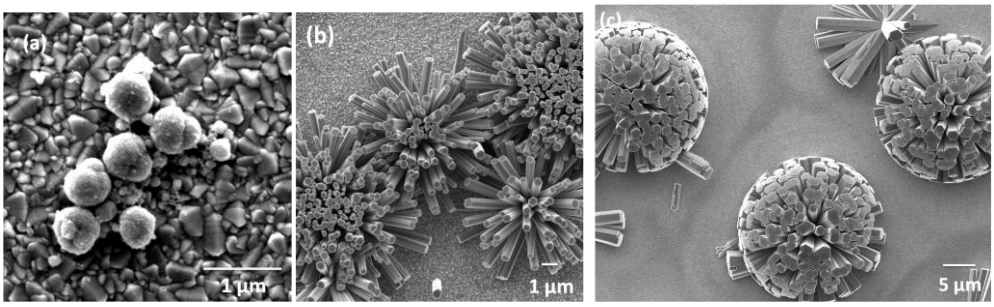

Figure 3. 8 SEM Images of (a) accumulated ZnO seeds deposited on an FTO substrate and (b, c) ZnO nanorods grown from the seeds in (a).

3.5 Conclusion

This work has demonstrated the use of forced hydrolysis for exerting control over the number density of ZnO nanorods grown by solution-based methods compatible with rough FTO substrates. Addition of water to and gentle heating of the ethanolic ZnO seed precursor solution results in increased size of ZnO crystallites that are deposited at a lower number density on the substrate. Chemical bath deposition on these seeds results in an array of nanorods that have lower number density but larger dimensions (diameter and length). With increased water addition, the aspect ratio declines monotonically, but the total nanorod surface area (and, therefore, the roughness factor) remains nearly constant as the effects of increased rod size and decreased number roughly cancel. By contrast, aging the seed precursor solution at room temperature results in agglomerated clusters that result in radial growth of nanorods giving "starburst" shapes. The forced-hydrolysis method enables large-scale and low-cost fabrication of ZnO nanorod arrays with controlled number density, even on rough FTO substrates.

3.6 References

1. I. Beinik, M. Kratzer, A. Wachauer, L. Wang, R. T. Lechner, C. Teichert, C. Motz, W. Anwand, G. Brauer, X. Y. Chen, X. Y. Hsu, and A. B. Djurisic, "Electrical properties of ZnO nanorods studied by conductive atomic force microscopy," *Journal of Applied Physics*, 110[5] 052005-7 (2011).
2. G. V. Elmore and H. A. Tanner, "The Photochemical Properties of Zinc Oxide," *The Journal of Physical Chemistry*, 60[9] 1328-29 (1956).
3. Y. Kinemuchi, M. Mikami, K. Kobayashi, K. Watari, and Y. Hotta, "Thermoelectric Properties of Nanograined ZnO," *Journal of Electronic Materials*, 39[9] 2059-63 (2010).

4. M. Li, Y. J. Su, W. Y. Chu, L. J. Qiao, A. A. Volinsky, and G. Kravchenko, "Local piezoelectric effect on single crystal ZnO microbelt transverse I-V characteristics," *Applied Physics Letters,* 98[8] 082105-3 (2011).

5. J. G. I K Bdikin, R Ayouchi, R Schwarz and A L Kholkin, "Local piezoelectric properties of ZnO thin films prepared by RF-plasma-assisted pulsed-laser deposition method," *Nanotechnology,* 21[23] 235703 (2010).

6. N. Gopalakrishnan, L. Balakrishnan, K. Latha, and S. Gowrishankar, "Influence of substrate and film thickness on structural, optical and electrical properties of ZnO thin films," *Crystal Research and Technology,* 46[4] 361-67 (2011).

7. M. Law, L. E. Greene, A. Radenovic, T. Kuykendall, J. Liphardt, and P. Yang, "ZnO−Al2O3 and ZnO−TiO_2 Core−Shell Nanowire Dye-Sensitized Solar Cells," *The Journal of Physical Chemistry B,* 110[45] 22652-63 (2006).

8. D. Wu, Z. Gao, F. Xu, J. Chang, W. Tao, J. He, S. Gao, and K. Jiang, "Hierarchical ZnO aggregates assembled by orderly aligned nanorods for dye-sensitized solar cells," *CrystEngComm,* 15[6] 1210-17 (2013).

9. K. S. Weißenrieder and J. Müller, "Conductivity model for sputtered ZnO-thin film gas sensors," *Thin Solid Films,* 300[1–2] 30-41 (1997).

10. S.-W. Chung, J.-Y. Yu, and J. R. Heath, "Silicon nanowire devices," *Applied Physics Letters,* 76[15] 2068-70 (2000).

11. P. Yang, H. Yan, S. Mao, R. Russo, J. Johnson, R. Saykally, N. Morris, J. Pham, R. He, and H. J. Choi, "Controlled Growth of ZnO Nanowires and Their Optical Properties," *Advanced Functional Materials,* 12[5] 323-31 (2002).

12. Z. L. Wang and J. Song, "Piezoelectric Nanogenerators Based on Zinc Oxide Nanowire Arrays," *Science*, 312[5771] 242-46 (2006).

13. A. B. Djurišić, A. M. C. Ng, and X. Y. Chen, "ZnO nanostructures for optoelectronics: Material properties and device applications," *Progress in Quantum Electronics*, 34[4] 191-259 (2010).

14. C.-Y. Chen, J. R. D. Retamal, I. W. Wu, D.-H. Lien, M.-W. Chen, Y. Ding, Y.-L. Chueh, C.-I. Wu, and J.-H. He, "Probing Surface Band Bending of Surface-Engineered Metal Oxide Nanowires," *ACS Nano*, 6[11] 9366-72 (2012).

15. B. Wei, K. Zheng, Y. Ji, Y. Zhang, Z. Zhang, and X. Han, "Size-Dependent Bandgap Modulation of ZnO Nanowires by Tensile Strain," *Nano Lett.*, 12[9] 4595-99 (2012).

16. S. A. Vanalakar, S. S. Mali, R. C. Pawar, N. L. Tarwal, A. V. Moholkar, J. H. Kim, and P. S. Patil, "Photoelectrochemical properties of CdS sensitized ZnO nanorod arrays: Effect of nanorod length," *Journal of Applied Physics*, 112[4] 044302-7 (2012).

17. D. Q. Yun, X. Y. Xia, S. Zhang, Z. Q. Bian, R. H. Liu, and C. H. Huang, "ZnO nanorod arrays with different densities in hybrid photovoltaic devices: Fabrication and the density effect on performance," *Chem. Phys. Lett.*, 516[1-3] 92-95 (2011).

18. J. S. Wang and K. M. Lakin, "c-axis inclined ZnO piezoelectric shear wave films," *Appl. Phys. Lett.*, 42[4] 352-54 (1983).

19. V. Manthina, J. P. Correa Baena, G. Liu, and A. G. Agrios, "ZnO–TiO_2 Nanocomposite Films for High Light Harvesting Efficiency and Fast Electron Transport in Dye-Sensitized Solar Cells," *J. Phys. Chem. C* (2012).

20. Y. Cui, A. Yu, H. Pan, X. Zhou, and W. Ding, "Catalytic outgrowth of SnO_2 nanorods from ZnO-SnO_2 nanoparticles microsphere core: combustion synthesis and gas-sensing properties," *CrystEngComm,* 14[21] 7355-59 (2012).

21. V. Manthina, J. P. Correa Baena, G. Liu, and A. G. Agrios, "ZnO–TiO_2 Nanocomposite Films for High Light Harvesting Efficiency and Fast Electron Transport in Dye-Sensitized Solar Cells," *The Journal of Physical Chemistry C,* 116[45] 23864-70 (2012).

22. S.-H. Yu, L. R. MacGillivray, and C. Janiak, "Nanocrystals," *CrystEngComm,* 14[22] 7531-34 (2012).

23. P. O'Brien, T. Saeed, and J. Knowles, "Speciation and the nature of ZnO thin films from chemical bath deposition," *Journal of Materials Chemistry,* 6[7] (1996).

24. L. Vayssieres, K. Keis, A. Hagfeldt, and S.-E. Lindquist, "Three-Dimensional Array of Highly Oriented Crystalline ZnO Microtubes," *Chemistry of Materials,* 13[12] 4395-98 (2001).

25. T. Yoshida, M. Tochimoto, D. Schlettwein, D. Wöhrle, T. Sugiura, and H. Minoura, "Self-Assembly of Zinc Oxide Thin Films Modified with Tetrasulfonated Metallophthalocyanines by One-Step Electrodeposition," *Chemistry of Materials,* 11[10] 2657-67 (1999).

26. B. O'Regan, V. Sklover, and M. Gratzel, "Electrochemical Deposition of Smooth and Homogeneously Mesoporous ZnO Films from Propylene Carbonate Electrolytes," *Journal of The Electrochemical Society,* 148[7] C498-C505 (2001).

27. L. Xu, Q. Liao, J. Zhang, X. Ai, and D. Xu, "Single-Crystalline ZnO Nanotube Arrays on Conductive Glass Substrates by Selective Disolution of Electrodeposited ZnO Nanorods," *The Journal of Physical Chemistry C,* 111[12] 4549-52 (2007).

28. M. H. Huang, Y. Wu, H. Feick, N. Tran, E. Weber, and P. Yang, "Catalytic Growth of Zinc Oxide Nanowires by Vapor Transport," *Advanced Materials,* 13[2] 113-16 (2001).

29. R. R. Bacsa, J. Dexpert-Ghys, M. Verelst, A. Falqui, B. Machado, W. S. Bacsa, P. Chen, S. M. Zakeeruddin, M. Graetzel, and P. Serp, "Synthesis and Structure–Property Correlation in Shape-Controlled ZnO Nanoparticles Prepared by Chemical Vapor Synthesis and their Application in Dye-Sensitized Solar Cells," *Advanced Functional Materials,* 19[6] 875-86 (2009).

30. J. Jie, G. Wang, Y. Chen, X. Han, Q. Wang, B. Xu, and J. G. Hou, "Synthesis and optical properties of well-aligned ZnO nanorod array on an undoped ZnO film," *Applied Physics Letters,* 86[3] 031909-3 (2005).

31. D. Bekermann, A. Gasparotto, D. Barreca, L. Bovo, A. Devi, R. A. Fischer, O. I. Lebedev, C. Maccato, E. Tondello, and G. Van Tendeloo, "Highly Oriented ZnO Nanorod Arrays by a Novel Plasma Chemical Vapor Deposition Process," *Crystal Growth & Design,* 10[4] 2011-18 (2010).

32. J. Liu, J. She, S. Deng, J. Chen, and N. Xu, "Ultrathin Seed-Layer for Tuning Density of ZnO Nanowire Arrays and Their Field Emission Characteristics," *The Journal of Physical Chemistry C,* 112[31] 11685-90 (2008).

33. T. Ma, M. Guo, M. Zhang, Y. Zhang, and X. Wang, "Density-controlled hydrothermal growth of well-aligned ZnO nanorod arrays," *Nanotechnology,* 18[3] 035605 (2007).

34. L. Spanhel and M. A. Anderson, "Semiconductor clusters in the sol-gel process: quantized aggregation, gelation, and crystal growth in concentrated zinc oxide colloids," *Journal of the American Chemical Society,* 113[8] 2826-33 (1991).

35. E. H. Otal, M. Granada, H. E. Troiani, H. Cánepa, and N. E. Walsöe de Reca, "Nanostructured Colloidal Crystals from Forced Hydrolysis Methods," *Langmuir,* 25[16] 9051-56 (2009).

36. Y. Hu and H.-J. Chen, "Preparation and characterization of nanocrystalline ZnO particles from a hydrothermal process," *Journal of Nanoparticle Research,* 10[3] 401-07 (2008).

37. W.-J. Li, E.-W. Shi, W.-Z. Zhong, and Z.-W. Yin, "Growth mechanism and growth habit of oxide crystals," *Journal of Crystal Growth,* 203[1–2] 186-96 (1999).

38. L. Vayssieres, K. Keis, S.-E. Lindquist, and A. Hagfeldt, "Purpose-Built Anisotropic Metal Oxide Material: 3D Highly Oriented Microrod Array of ZnO," *J. Phys. Chem. B,* 105[17] 3350-52 (2001).

39. A. M. Lockett, P. J. Thomas, and P. O'Brien, "Influence of Seeding Layers on the Morphology, Density, and Critical Dimensions of ZnO Nanostructures Grown by Chemical Bath Deposition," *The Journal of Physical Chemistry C,* 116[14] 8089-94 (2012).

40. H. L. Q. Cao, X. F.; Gong, Q.; Du, W. M.; Ma, X. D.; Zhu, Z. K, "Shape- and size-controlled synthesis of nanometer ZnO from a simple solution route at room temperature.," *Nanotechnology,* 17 (2006).

41. W. Wu, G. Hu, S. Cui, Y. Zhou, and H. Wu, "Epitaxy of Vertical ZnO Nanorod Arrays on Highly (001)-Oriented ZnO Seed Monolayer by a Hydrothermal Route," *Crystal Growth & Design,* 8[11] 4014-20 (2008).

42. S.-C. Liou, C.-S. Hsiao, and S.-Y. Chen, "Growth behavior and microstructure evolution of ZnO nanorods grown on Si in aqueous solution," *Journal of Crystal Growth,* 274[3–4] 438-46 (2005).

43. S.-W. Chen and J.-M. Wu, "Nucleation mechanisms and their influences on characteristics of ZnO nanorod arrays prepared by a hydrothermal method," *Acta Materialia,* 59[2] 841-47 (2011).

44. C.-C. Lin, S.-Y. Chen, and S.-Y. Cheng, "Nucleation and growth behavior of well-aligned ZnO nanorods on organic substrates in aqueous solutions," *Journal of Crystal Growth,* 283[1–2] 141-46 (2005).

45. C.-S. Hsiao, C.-H. Peng, S.-Y. Chen, and S.-C. Liou, "Tunable growth of ZnO nanorods synthesized in aqueous solutions at low temperatures," *Journal of Vacuum Science & Technology B: Microelectronics and Nanometer Structures,* 24[1] 288-91 (2006).

46. S. Xu and Z. Wang, "One-dimensional ZnO nanostructures: Solution growth and functional properties," *Nano Research,* 4[11] 1013-98 (2011).

47. H. Ghayour, H. R. Rezaie, S. Mirdamadi, and A. A. Nourbakhsh, "The effect of seed layer thickness on alignment and morphology of ZnO nanorods," *Vacuum,* 86[1] 101-05 (2011).

48. J. E. Boercker, J. B. Schmidt, and E. S. Aydil, "Transport Limited Growth of Zinc Oxide Nanowires," *Cryst. Growth Des.,* 9[6] 2783-89 (2009).

49. W.-Y. Wu, C.-C. Yeh, and J.-M. Ting, "Effects of Seed Layer Characteristics on the Synthesis of ZnO Nanowires," *J. Amer. Ceram. Soc.,* 92[11] 2718-23 (2009).

50. W. Liang, B. D. Yuhas, and P. Yang, "Magnetotransport in Co-Doped ZnO Nanowires," *Nano Letters,* 9[2] 892-96 (2009).

51. D. Singh, A. A. Narasimulu, L. Garcia-Gancedo, Y. Q. Fu, N. Soin, G. Shao, and J. K. Luo, "Novel ZnO nanorod films by chemical solution deposition for planar device applications," *Nanotechnology,* 24[27] 275601 (2013).

52. H. Zeng, P. Liu, W. Cai, X. Cao, and S. Yang, "Aging-Induced Self-Assembly of Zn/ZnO Treelike Nanostructures from Nanoparticles and Enhanced Visible Emission," *Cryst. Growth Des.,* 7[6] 1092-97 (2007).

53. X. Yan, Z. Li, C. Zou, S. Li, J. Yang, R. Chen, J. Han, and W. Gao, "Renucleation and Sequential Growth of ZnO Complex Nano/Microstructure: From Nano/Microrod to Ball-Shaped Cluster," *The Journal of Physical Chemistry C,* 114[3] 1436-43 (2010).

54. Y. F. Zhu, G. H. Zhou, H. Y. Ding, A. H. Liu, Y. B. Lin, and N. L. Li, "Controllable synthesis of hierarchical ZnO nanostructures via a chemical route," *Physica E: Low-dimensional Systems and Nanostructures,* 42[9] 2460-65 (2010).

55. S. Hong, J. Yeo, W. Manorotkul, G. Kim, J. Kwon, K. An, and S. H. Ko, "Low-Temperature Rapid Fabrication of ZnO Nanowire UV Sensor Array by Laser-Induced Local Hydrothermal Growth," *Journal of Nanomaterials,* 2013 7 (2013).

56. A. Menzel, K. Subannajui, F. Güder, D. Moser, O. Paul, and M. Zacharias, "Multifunctional ZnO-nanowire-based sensor," *Advanced Functional Materials,* 21[22] 4342-48 (2011).

57. Z. Hui, W. Jianbo, Z. Chuanxin, D. Ning, M. Xiangyang, and Y. Deren, "From ZnO nanorods to 3D hollow microhemispheres: solvothermal synthesis, photoluminescence and gas sensor properties," *Nanotechnology*, 18[45] 455604 (2007).

Chapter 4
ZnO-TiO_2 nanocomposite films for high light harvesting efficiency and fast electron transport in dye-sensitized solar cells

Abstract

Electron transport and recombination are the essential processes that determine the charge collection efficiency (η_{CC}) in dye sensitized solar cells (DSSC). While η_{CC} is close to unity in well-built ordinary DSSCs, its value can be sharply reduced by the use of redox couples other than iodide/triiodide due to fast electron recombination. To compensate, structures capable of fast electron transport are needed. Nanorod arrays that have this attribute tend to suffer from low surface area, resulting in low dye loading and reduced light harvesting efficiency (η_{LH}).We have therefore developed a novel nanocomposite structure consisting of zinc oxide (ZnO) nanorods coated with titanium dioxide (TiO_2) nanoparticles using an electrostatic layer-by-layer (LbL) deposition technique. The titanium dioxide nanoparticle coating can add an order of magnitude of surface area and is compatible with known high-performance dyes. This composite nanostructure has been designed to take advantage of the improved electron transport along the nanorods and surface area provided by the nanoparticles, yielding high η_{CC} and η_{LH}. In tests using ferrocene/ferrocenium as a model alternative redox couple with fast recombination, I-V measurements indicate that the ZnO-TiO_2 films have higher charge collection efficiency than conventional TiO_2 nanoparticulate films.

4.1 Introduction

Dye sensitized solar cells (DSSCs)[1] are low cost alternatives to expensive silicon photovoltaics. The conventional DSSCs consists of two sandwiched pieces of conducting glass, one of them coated with mesoporous layer of nanoparticulate TiO_2 with a self-assembled monolayer of chemisorbed dye molecules, filled with an electrolyte for dye regeneration. The dye is a transition metal complex or organic chromophore that harvests sunlight by absorbing strongly in visible region of the solar spectrum. The principal photovoltaic losses in the DSSCs are due to incomplete light harvesting, reombination of the photoinjected electrons with the electrolyte and the over potential required for dye regeneration. Ruthenium complex dyes like N719, N3 and the black dye exhibit high efficiency with the I^-/ I_3^- redox couple, but there is little room for improvement in light harvesting in the visible range.

In DSSCs, the I^-/ I_3^- redox couple limits the overall efficiency due to the high overpotential (ca. 0.5 V) for dye regeneration by I^-. This is believed to be due to the complex multielectron mechanism of the I^-/ I_3^- redox couple involving the radicals diiodide ($I_2^{-\cdot}$) and atomic iodine ($I^\cdot$). [2] The effect is that the dye HOMO level must be about 0.5 V more positive than the I^-/ I_3^- redox level. Since the voltage output of the cell is the difference between the redox level and the quasi-Fermi level in the semiconductor, this 0.5 V is lost. An alternative redox electrolyte that could regenerate the sensitizer from a potential closer to its HOMO would result in higher cell voltage and efficiency, if all else were held equal. Unfortunately, alternatives (such as iron or cobalt complexes) tend to recombine rapidly with conduction-band electrons, reducing the quasi-fermi level and resulting in no benefit.

There have been important recent advances in using specialized dyes to slow recombination with electrolytes based on ferreocene or cobalt bipyridyl complexes.{ Feldt and Hagfeldt; Udo Bach; Grätzel}Our approach is to utilize novel semiconductor structures to attain fast electron transport in order to improve charge collection efficiency. The combination of these approaches will maximize solar cell performance. In particular, by providing some tolerance of accelerated recombination, structures for fast electron transport enable the use of standard dyes such as N719, which are more facile products than the specialized dyes mentioned above, which tend to be large and difficult to synthesize.

Electron transport in DSSCs is slow due to trapping of the electrons in the grain boundaries and the relatively long and tortuous path of the electron to the FTO. [3, 4] In a 10 μm thick film an electron visits about 10^6 nanoparticles on average before reaching the FTO surface. [5] The resulting slow transport is adequate in the presence of iodide/triiodide, since its recombination kinetics are slow, but inadequate when using an alternative redox couple with faster recombination.

Fast electron transport can be achieved by developing 1-D nanostructures like nanotubes, nanorods and nanowires of metal oxides. ZnO is a highly favorable material for application in DSSCs since it can be grown in monocrystalline nanorods using facile methods, its electron mobility is high[6], and its band edge energies are very close to those of TiO_2.[7] ZnO is the metal oxide with the second highest efficiency achieved in DSSCs. [8, 9, 10] ZnO nanorods can be synthesized on the substrate in-situ through various procedures, such as chemical bath deposition [11, 12], electrodeposition[13, 14, 15], and chemical vapor deposition.[16, 17] However, the main

disadvantage of nanorods is a lower surface area than a nanoparticle film for adsorption of light-harvesting molecules. In addition, the dye performance tends to be worse on ZnO than on TiO_2.

To create a structure with both fast electron transport and high surface area, we developed a hybrid photoanode consisting of ZnO nanorods coated with TiO_2 nanoparticles using facile wet-chemical methods. ZnO nanorods were grown by chemical bath deposition (CBD), a low-temperature catalyst-free process suitable for industrial applications. TiO_2 nanoparticles were coated uniformly over the nanorods by electrostatic layer-by-layer (LbL) deposition. The LbL technique is based on exposing a substrate sequentially to cationic and anionic substances, which form successive bilayers by electrostatic attraction.

In this work we compared hybrid films to ZnO nanorod-only films and TiO_2 nanoparticle-only films in terms of dye loading and device performance. For the latter measure we compared DSSC devices using two different redox couples: iodide/triiodide (I^-/I_3^-) and ferrocene/ferrocenium (Fc/Fc^+). We have chosen the latter as a model alternative redox couple with fast recombination kinetics. After Tests with Fc/Fc^+ these hybrid photoanodes can collect more injected than a conventional TiO_2 nanoparticle film with equivalent dye loading .

4.2 Experimental

Reagents and Materials. Except where noted all chemicals were purchased from Sigma-Aldrich and were ACS grade or better. N719 was purchased from Dyesol (Australia). SnO_2: F glass (FTO, transmission> 80% in the visible spectrum; sheet resistance 8 Ω /□) was purchased from Hartford Glass Co (U.S.A).

Electrode Fabrication. ZnO nanorods were synthesized by a two-step chemical bath deposition (CBD) technique.[18]A modified seed solution was used for the growth of nanorods optimized for subsequent TiO_2 deposition. ZnO seeds were synthesized by dissolving 5mM Zinc acetate dihydrate in ethanol by stirring on hotplate for 3 hours at room temperature. After 3 hours of dissolving ZnO seeds were hydrolyzed by adding 0.8M of deionized water to the seed solution. The solution was stirred for 3 hours on the hotplate and then transferred into preheated oven at 80˚C for 12 hours. The modified seed layer solution and its effect on ZnO nanorod growth is explained in detail in our future publication. Slides of borosilicate glass with a conducting SnO_2:F (FTO) layer were cut into 25 x 50 mm pieces and cleaned by 10 min sonication in a detergent solution (5% RBS-25 in water) followed by ethanol. The seed solution was drop-coated on precleaned FTO. Immediately after ethanol visibly evaporated from the substrate, the substrate was rinsed with reagent ethanol and dried with nitrogen. The seed layer process was repeated twice. Subsequently, the seeded FTO glass was heated at 350°C on a titanium hot plate for 30 min. CBD followed by preparing an aqueous solution of 50 mM zinc nitrate hexahydrate, 50 mM hexamethylenetetramine and 6 mM polyethyleneimine in an ice bath. The seeded substrates were placed at an angle of 60° in a 100-mL glass bottle with the seeds facing the bottom of the bottle. The temperature of the oven was maintained at 90°C for 24-h. Finally the substrates were removed from the growth solution rinsed with ethanol, and dried with nitrogen. The length of the obtained ZnO nanorods was 5 µm and the diameter was 600 nm.

TiO_2 nanoparticles were synthesized by hydrolysis of titanium tetraisopropoxide [19] and deposited using the electrostatic layer-by-layer technique. [20] As previously described[20], TiO_2 nanoparticles (2 g/L colloidal TiO_2) were made through hydrolysis of titanium isopropoxide

followed by peptization. The colloidal solution was autoclaved for 12 h at 250°C and then dispersed with a 200 W ultrasonic titanium probe. The resulting colloidal solution was concentrated with a rotary-evaporator and was washed with pure water. The substrate was immersed in a cationic 1 g/L polymer solution (polydiallyldimethyl ammonium chloride (PDAC), 70 kDa, Aldrich) in water and then in an aqueous suspension of anionic TiO_2 particles with intermediate rinsing and drying steps. All solutions contained 5 mM triethylamine (resulting in a pH near 11) to maintain negative particle surface charge. For deposition on bare FTO, the dipping time in the TiO_2 suspension was 5 min. When coating nanorods, the dipping time was 30 min to allow penetration of the channels between the rods. The dipping cycles were carried out using an automated device (DR-3, Riegler & Kirstein GmbH). LbL was followed by sintering at 500°C to remove polymer layers.

Surface/Structure Characterization. The morphology of ZnO nanorods and TiO_2 nanoparticles was investigated by scanning electron microscopy (FEI Quanta FEG250 SEM in High vacuum mode). The ZnO nanorods and TiO_2 nanoparticles were additionally characterized by X-ray powder diffraction (XRD) using a Bruker D8 Advance X-ray diffractometer using Cu K_radiation (λ = 0.154178 nm) at a scanning rate of 0.04˚ s^{-1} in the 2θ range from 10˚ to 90˚. The XRD data were analyzed using the Debye-Scherrer equation to determine the TiO_2 particle size.

Sensitization. After sintering, films were allowed to cool to 100°C then immediately immersed in 0.3 mM N719 in ethanol. After 12 hours they were removed and rinsed in acetonitrile and dried in air.

Solar Cell Assembly. Each sensitized electrode was sealed against a counter electrode on hot plate at 120°C using a hot-melt plastic frame (Solaronix, Meltonix 1170, 25 µm thick) applying light pressure with a glass rod. The assembled cell was filled with electrolytes through two holes in the counter electrode. The holes were then sealed using hot-melt plastic and a thin glass cover slide. The exposed conducting glass leads of each electrode were coated with copper tape (3M) for improved electrical conductivity.

Dye Uptake. To measure the amount of N719 dye adsorbed by a film, a dyed and twice-rinsed 4.5 cm × 2.5 cm electrode was placed in 3 mL of 0.1 M NaOH in water. As the solvent volume was not sufficient to immerse the electrode, solvent was repeatedly pipetted over the electrode. After repetitions, the dye was visibly completely desorbed from electrode.

The spectrum of the desorbed dye was measured in a 1 cm quartz cuvette using a Varian Cary 50 spectrophotometer. The literature peak extinction coefficient of N719 (14,300 M^{-1} cm^{-1}) in ethanol [21] was used to obtain the corrected value in basified water. The molar extinction coefficient for N719 in water with 0.1 M NaOH was found to be 16,500 M^{-1} cm^{-1}. This value was used to quantify the amount of desorbed dye.

Electrolyte Composition.

Iodide/triiodide (I^-/I_3^-) electrolyte was prepared with 0.5 M tetrabutylammonium iodide and 0.05 M iodine (I_2) in 3-methoxypropionitrile. The ferrocene/ferrocenium (Fc/Fc^+) electrolyte contained 0.1 M ferrocene and 0.05 M ferrocenium hexafluorophosphate (Aldrich) in 3-methoxypropionitrile.

The Fc/Fc^+ electrolyte was deoxygenated by bubbling, nitrogen 10 minutes prior to cell fabrication to minimize reaction of ferreocene with oxygen.[22, 23]

Transient Measurements.

Measurements of electron transport time were made using a set of National Instruments components in a PXIe chassis capable of high-resolution analog voltage output and digitized input. A square-wave modulation was applied to a white-light LED that was used to illuminate a DSSC. The modulation amplitude produced a <10% change in DSSC current, which is linear with light intensity. The DSSC was operated in series with a 65-Ω resistor and the voltage across this resistor was measured. The current is determined by $I = V/R$. We refer to this as a "quasi-short-circuit" mode, as the small voltages measured (<20 mV) were close to the short-circuit condition, compared to open circuit voltages of hundreds of millivolts. At least 50 transients were averaged for noise reduction.

Solar Cell Characterization. Current –Voltage **(** J- V) measurements were made using Keithley 2400 source/meter controlled by a PC, while irradiating at 1000 W/m^2 with AM 1.5G simulated sunlight produced by a solar simulator (Newport 91160). The DSSCs photo current and photo voltage were measured with an active area of 1 cm^2.

4.3 Results and Discussion

4.3.1 ZnO nanorods

ZnO nanorods were fabricated on FTO. A typical example is shown in Figure 4. 1, having nanorod dimensions of about 5 μm length and 600 nm diameter, and a number density of 1.2×10^8 rods per cm^2 of FTO after 24 h deposition.

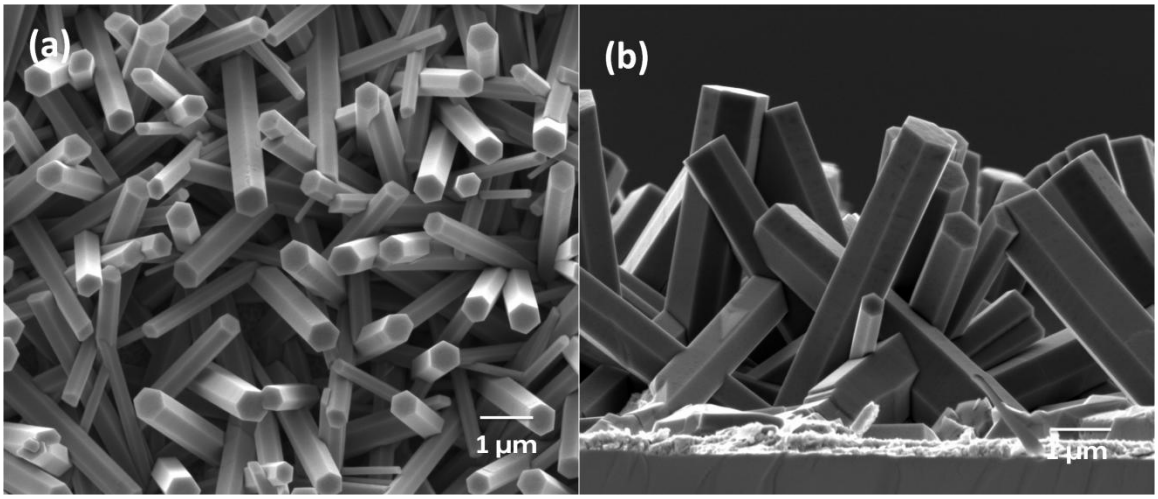

Figure 4. 1 SEM images of ZnO nanorods in top view (a) and cross section (b)

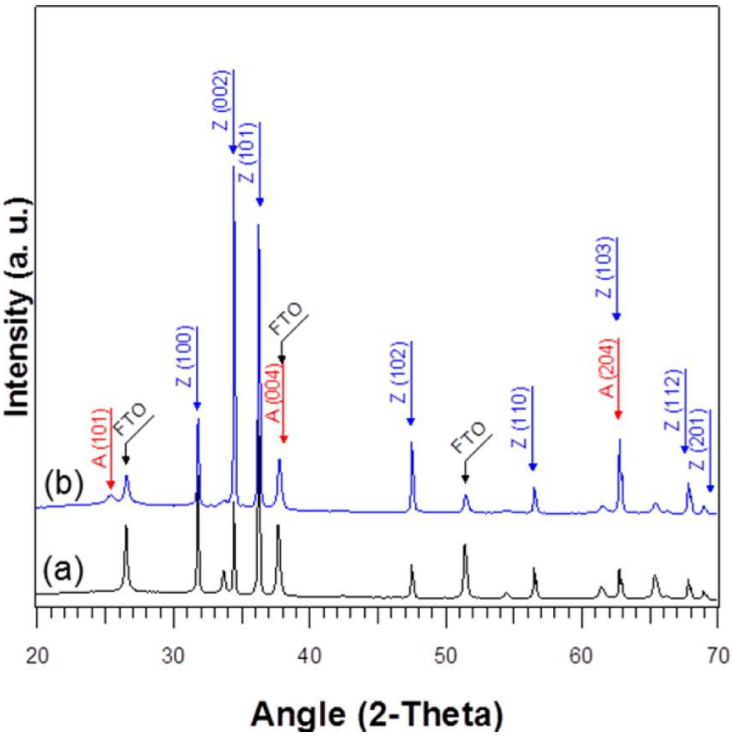

Figure 4. 2 X-ray diffraction pattern of (a) ZnO nanorods and (b) ZnO nanorods coated with TiO_2 nanoparticles, on a fluorine-doped tin oxide substrate. Z and A denote wurtzite ZnO and anatase TiO_2, respectively.

The XRD θ–2θ scan data show that, for well-aligned nanorods on FTO intensity of the peak assigned to the (002) plane of ZnO was clearly revealing that ZnO nanorods were formed through elongation along the *c*-axis perpendicularly to the substrate. Figure 4. 2 shows the XRD pattern of pure ZnO nanorods recorded in the range of 10-90° with a scanning step of 0.02°. All diffraction peaks can be attributed to crystalline ZnO with the hexagonal wurtzite structure (space group: P63*mc*(186); *a*) 0.3249 nm, *c*) 0.5206 nm). The data are in agreement with the Joint Committee on Powder Diffraction Standards (JCPDS) card for ZnO (JCPDS 070-8070).

4.3.2 ZnO-TiO_2 hybrid films

TiO_2 nanoparticles were synthesized by an autoclave hydrolysis method and ultimately dispersed in water. On the basis of a Scherrer analysis of the (010) peak at 26° of an X-ray powder diffraction pattern (not shown), the crystallite size of the TiO_2 nanoparticles was found to be 16 nm, and only the anatase phase was observed. Particle size is generally similar to crystallite size for this synthesis method.[24] LbL deposition was used to deposit these nanoparticles over ZnO nanorods. Initial trials used a TiO_2 deposition time of 5 min per LbL cycle. XRD spectra for these samples (Figure 4. 2 b) have added peaks indicating the anatase phase of TiO_2, while retaining the same ZnO wurtzite peaks, indicating that the ZnO nanorod crystal structures were not affected by the deposition and sintering.

Scanning electron micrographs showing the results of different numbers of LbL layers of TiO_2 are shown in Figure 4. 3. The first layer of TiO_2 coats the nanorods well, with successive layers increasing the TiO_2 film thickness while a conformal coating is maintained. However, cross-sectional images (not shown) revealed that the TiO_2 particles did not reach the bottom of the nanorods. We therefore lengthened the TiO_2 dipping time to 30 min in each LbL cycle. With this

modification, the TiO_2 nanoparticles completely penetrate the nanorod film and evenly coat all surfaces. An example using three layers is shown in top view and in cross section, in Figure 4. 4.

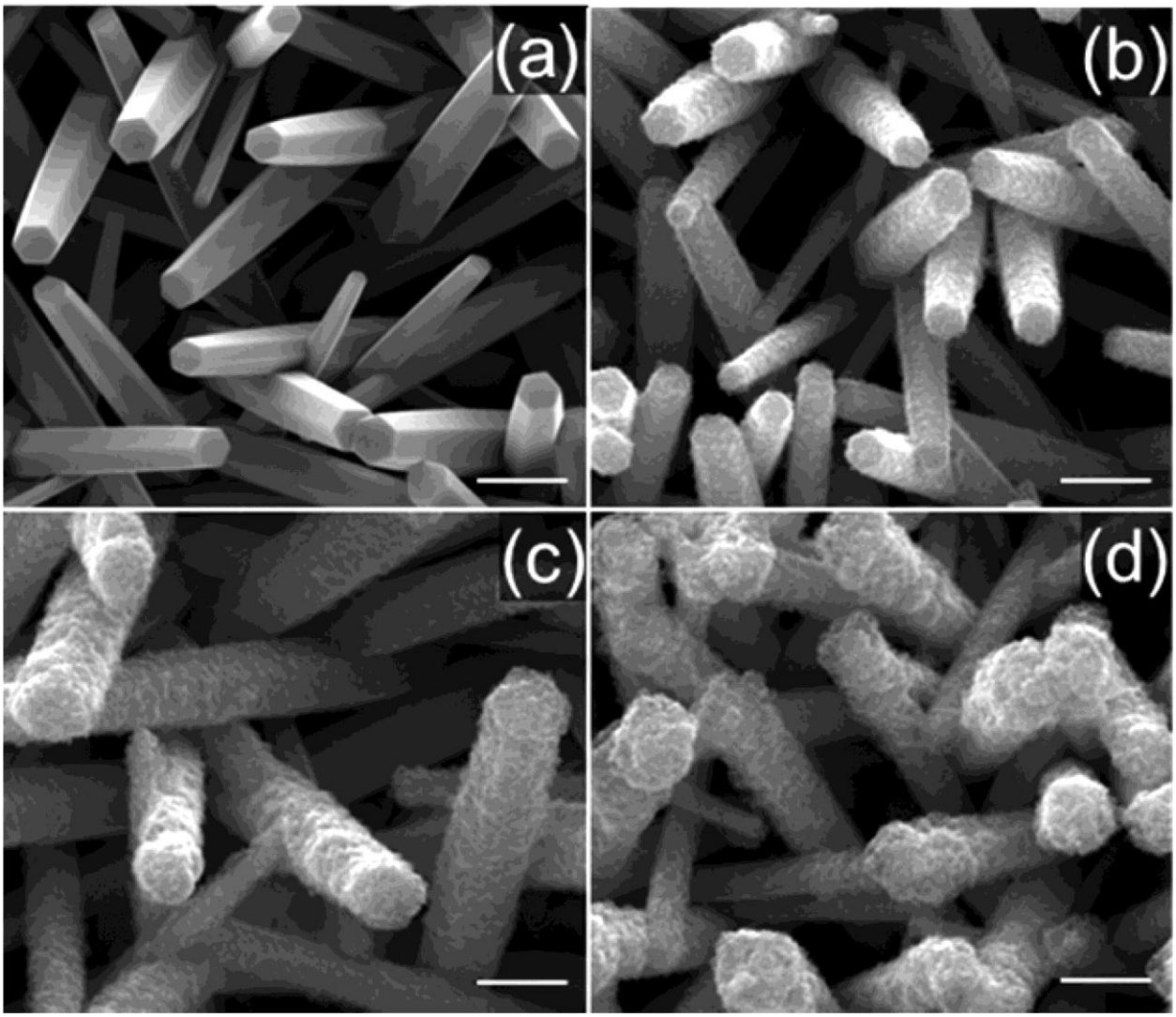

Figure 4. 3 SEM images of ZnO nanorods coated with zero (a), one (b), three (c), or five (d) layers of TiO_2 with 5-min immersion periods. Scale bar: 1 μm.

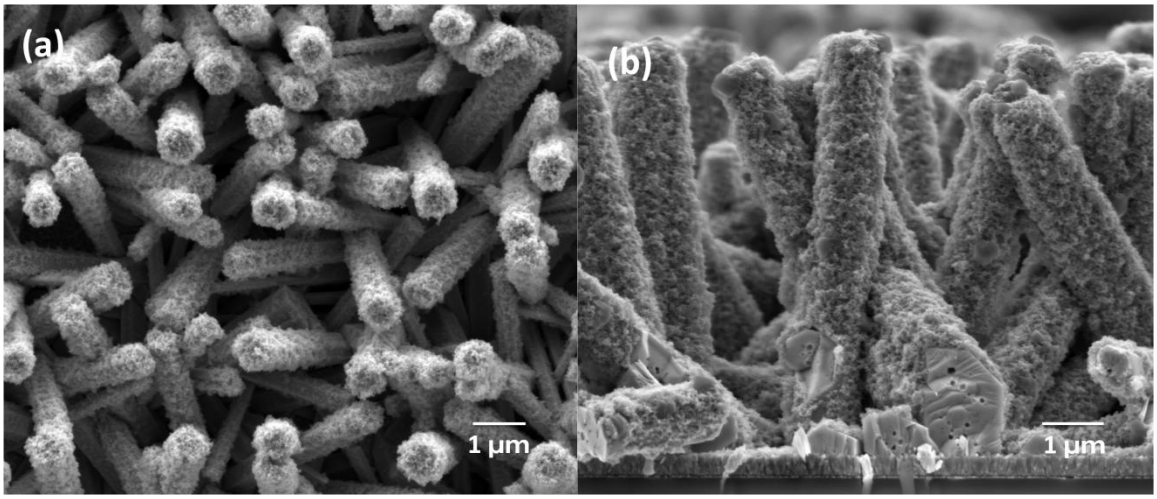

Figure 4. 4 ZnO nanorods coated with three layers of TiO_2 nanoparticles using 30-min dipping times shown in top view (a) and cross section (b).

4.3.3 Dye loading

If small spheres form a monolayer with simple square packing over a large cylinder of area *A* (not considering the end faces), the added area will be πA. This implies that three monolayers would increase the surface area by about an order of magnitude. Dye desorption measurements (Figure 4. 6) following sensitization with N719 showed that a ZnO nanorod array (Z) adsorbed 3.5 nmol of dye/cm^2 of geometric film area, whereas a nanorod array coated with three layers of TiO_2 nanoparticles (ZT) adsorbed 13.9 nmol/cm^2, for a difference of nearly a factor of 4. That this is less than the factor of ~10 calculated above is not surprising given the approximation of square packing and the fact that an LbL film has considerable porosity.[20] We found that 30 layers of TiO_2 deposited on a flat FTO substrate had a dye loading comparable to that of the ZT hybrid film. Therefore, 30-layer TiO_2 films (T) shown in Figure 4. 5 were used in the device performance experiments for comparison with the composite films. The thickness of the 30-layer TiO_2 film is approximately 0.6 µm as measured by scanning electron microscopy (not shown). LbL TiO_2 films have similar morphology to doctor-bladed TiO_2 films[20] and similar performance

in DSSCs when deposited at comparable thickness.[25] For reference, a dye loading for a typical 10-µm film would be ca. 100 nmol/cm^2.[26, 27, 28]

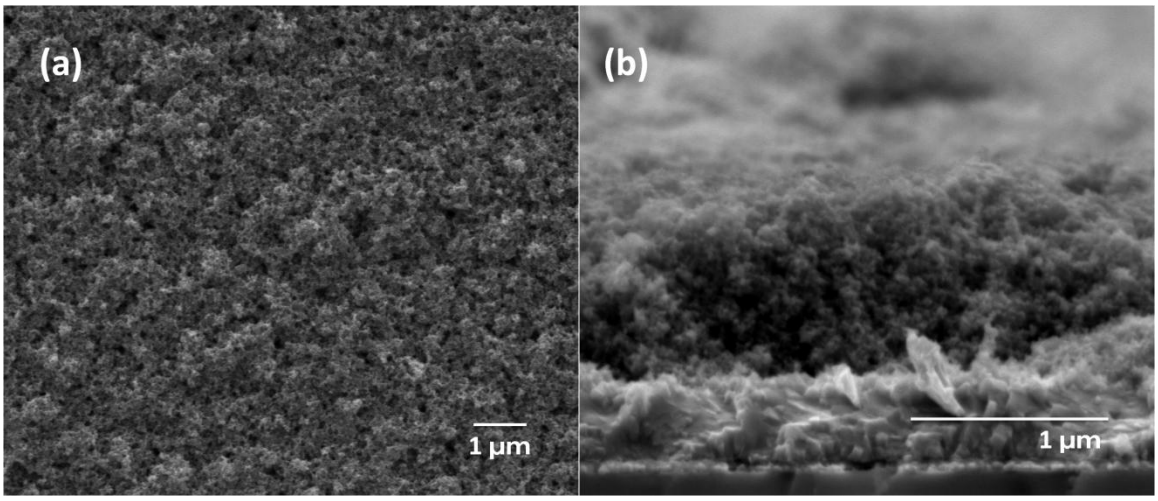

Figure 4. 5 SEM images of a 30-layer film of TiO_2 nanoparticles on FTO (a) top view (b) cross section.

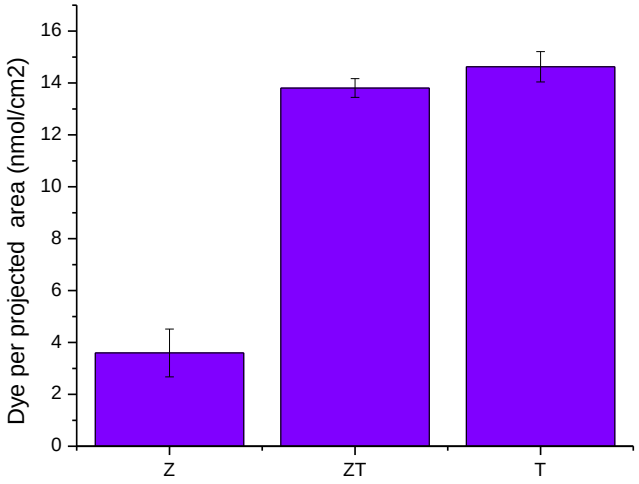

Figure 4. 6 Uptake of N719 by ZnO NR array (Z), a NR array coated with three layers of TiO_2 nanoparticles (ZT), and film of 30 layers of TiO_2 nanoparticles (T), all on FTO.

4.3.4 Electron Transport

Figure 4. 7a shows representative current transients at quasi-short-circuit conditions for Z, ZT, and T films. Each transient is well-fit by a single exponential decay of the form $y = y_0 + A \exp(-t/\tau_{tr})$, where τ_{tr} is the characteristic time for electron transport. The fitted time constants τ_{tr} over a range of light intensities are plotted against the corresponding short-circuit current density J_{SC} in Figure 4. 7 b. For TiO_2, the power-law decrease of τ_{tr} with increasing J_{SC} is typical of DSSCs and is well-described by a trapping–detrapping model.[28] Time constants for the other samples are relatively constant at about 0.29 ms for ZnO nanorods and 0.46 ms for ZnO nanorods coated with TiO_2 nanoparticles. The invariability of τ_{tr} with J_{SC} for the Z and ZT samples strongly suggests that a limit of the measurement has been reached, most likely due to an *RC* time based on the resistance of the cell and resistor connected in series and the capacitance of the semiconductor/electrolyte interface.[29] These time constants should therefore be taken as an upper limit on the electron transport time of the ZnO nanorod-based materials. Since the *RC* time may differ for different samples, the results shown in Figure 4. 7 b cannot differentiate between the τ_{tr} value of Z and ZT films, but they do demonstrate that electron transport in these samples is at least 2 orders of magnitude faster than transport through nanoparticulate TiO_2.

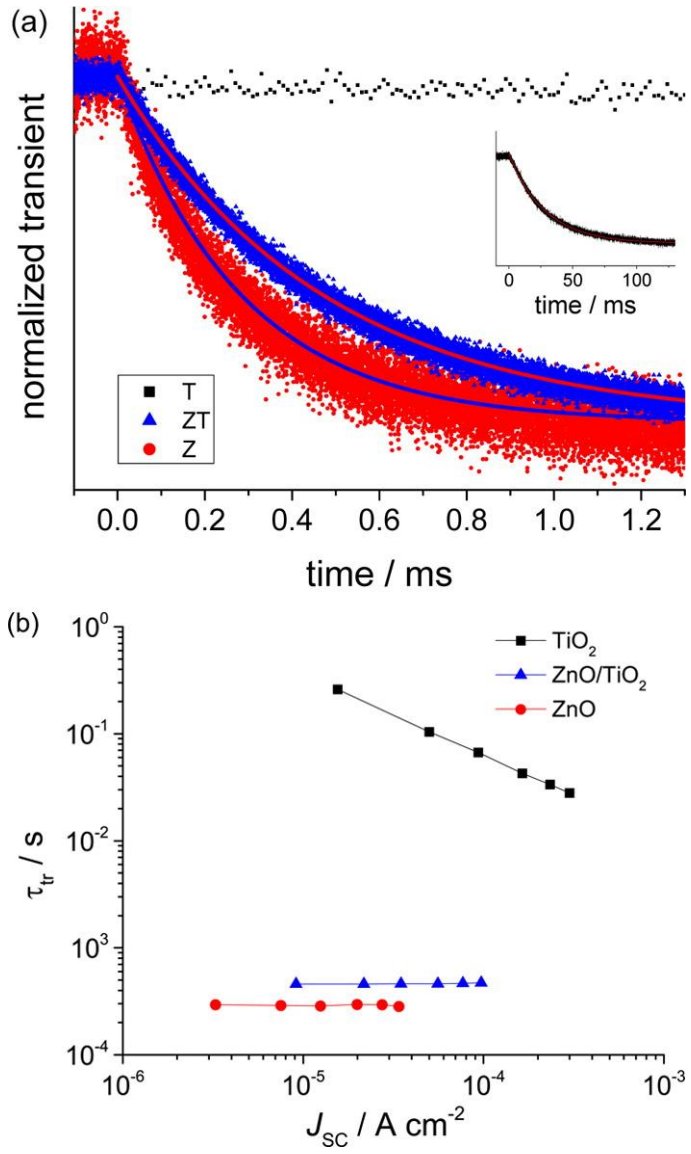

Figure 4. 7 (a) Transients for decay of quasi-short-circuit current in response to square-wave modulation of light intensity, with single-exponential fits. The inset shows TiO_2 transient at a longer time scale. (b) Fitted electron transport time constants versus versus quasi-short-circuit current for T, ZT, and Z films.

4.3.5 Device Performance

Figure 4. 8 a compares the current–voltage characteristics of the DSSCs made from the three different films in a conventional iodide/triiodide electrolyte. Each trace represents the mean of triplicate measurements, and the dotted lines indicate one standard deviation from the mean at

each voltage. The ZT hybrid film strongly outperforms the Z film, indicating that the higher surface area and dye loading of the ZT film translate into higher photocurrents. Under these conditions, the TiO_2-only film T outperforms both Z and ZT, which is to be expected since TiO_2 nanoparticles are known to give the best performance of any material when recombination rates are low.

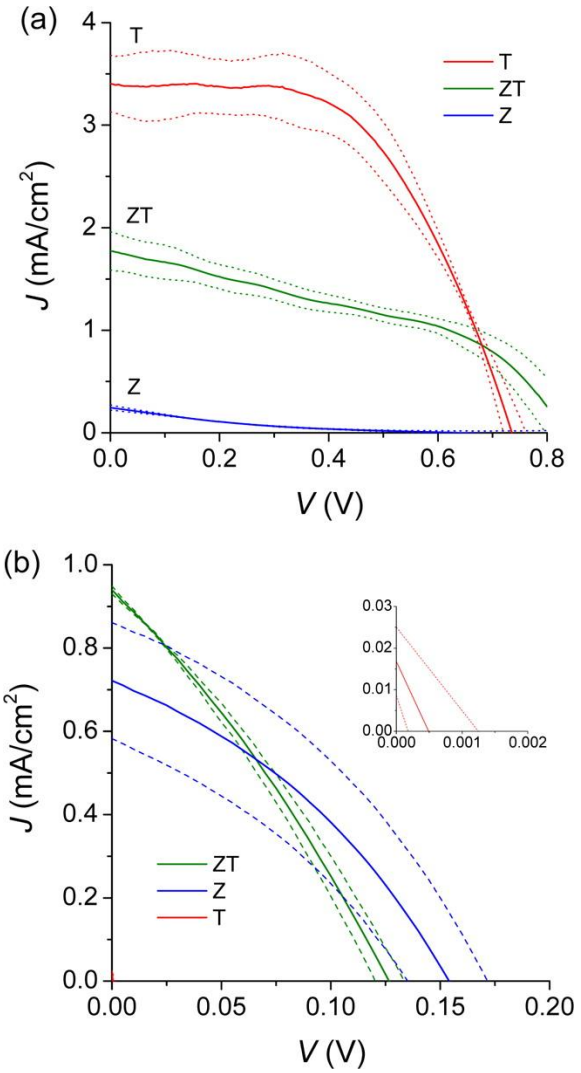

Figure 4. 8 Current–voltage (J–V) characteristics for solar cells using ZT, Z, and T films and electrolyte based on (a) I^-/I_3^- or (b) Fc/Fc^+, under illumination with 100 mW/cm^2 AM1.5G simulated sunlight. Solid and dotted lines show mean ± SD for triplicate samples. The inset in part b magnifies the T trace.

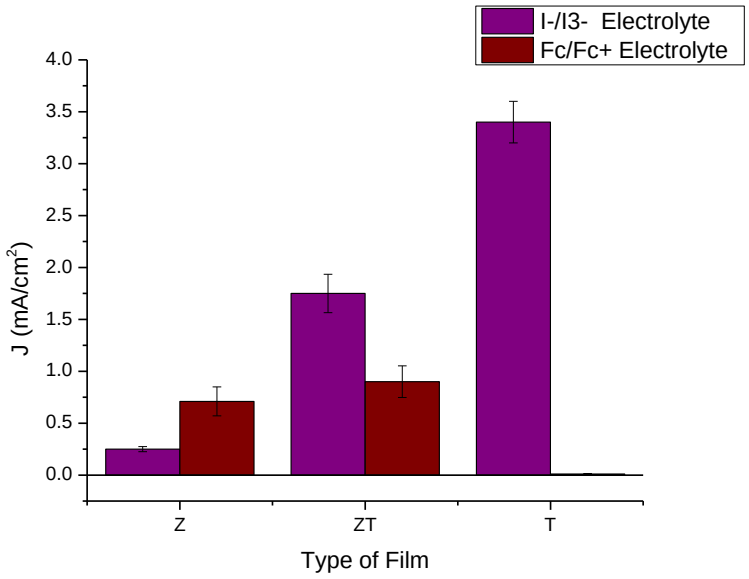

Figure 4. 9 Short circuit current of DSSCs constructed with I^-/I_3^- and Fc/Fc^+ electrolyte using Z , ZT hybrid and T films under illumination with 100 mW/cm^2 AM1.5G simulated sunlight.

The benefit of the hybrid structure is revealed when using ferrocene/ferrocenium as a model alternative redox couple with high recombination rates (Figure 4. 7 b). We focus here on the changes in the short circuit current (J_{SC}), as these report on the electron collection efficiency. We note that faster electron transport can improve J_{SC} due to higher electron collection efficiency, but it cannot improve the open-circuit voltage (V_{OC}) since no electron transport occurs at open circuit. Values of J_{SC} extracted from Figure 4. 8 are compared in Figure 4. 9. The rapid scavenging of conduction band electrons by Fc^+ almost completely short-circuits a cell with a conventional TiO_2 nanoparticulate film (T), resulting in a barely visible *J*–*V* trace with a short-circuit current of only 16 μA/cm^2. A ZnO nanorod film (Z) has much better performance, with J_{SC} = 0.72 mA/cm^2. The hybrid film ZT has the best short circuit current (0.93 mA/cm^2) due to its higher surface area and dye loading. The difference in performance here is smaller than with

I^-/I_3^-, which we attribute to (1) recombination of electrons from the TiO_2 with the Fc^+ during the time between electron injection and electron transfer from TiO_2 to the ZnO, and/or (2) impeded electron transfer from the TiO_2 into the ZnO, as will be discussed below. The surprising result that the Z film obtains a higher current in an Fc/Fc^+ electrolyte than in an I^-/I_3^- electrolyte may be the result of corrosion of ZnO by the latter electrolyte,[30] which we have observed in SEM images (not shown) of ZnO nanorods before and after exposure to I^-/I_3^-.

4.3.6 Energy Barrier

Transfer of electrons from the TiO_2 nanoparticles to the ZnO nanorods must be downhill in energy. Assuming that electron transfer occurs between the conduction bands of the two materials and that electrons are rapidly thermalized within the conduction bands, this requires that the conduction band minimum (CBM) of ZnO lie at a more positive potential than that of TiO_2. The conduction band edges of ZnO and TiO_2 would be expected to lie quite close to each other in energy, and the relative difference between the two is difficult to predict. As an indirect measure of this band edge offset, we measured current–voltage curves in the dark and in the absence of dye. The measured "dark current" is due entirely to recombination at the semiconductor/electrolyte interface.

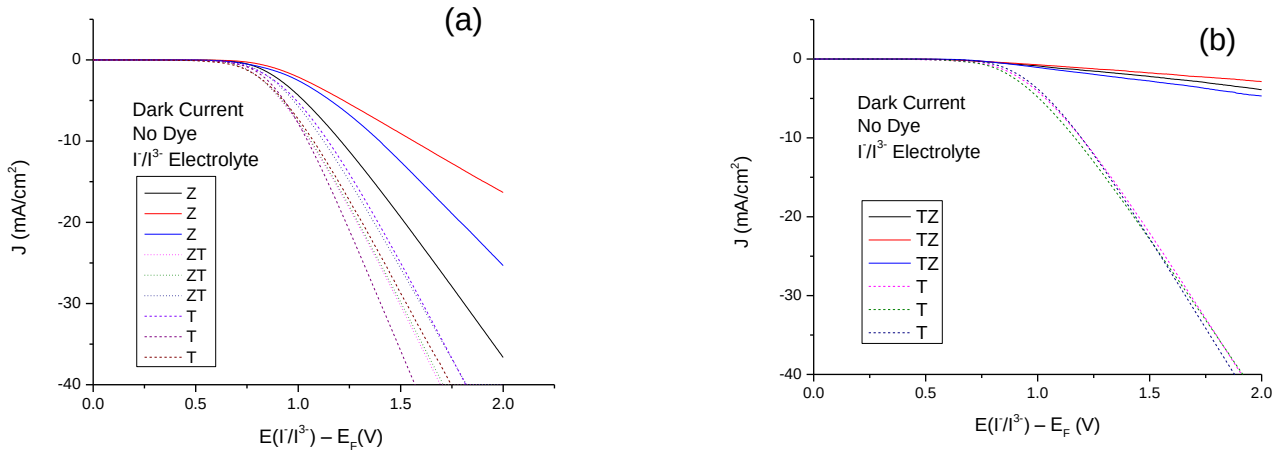

Figure 4. 10 Dark currents of dye-free films: (a) Z, ZT, and T and (b) TZ and T.

In this measurement, electrons flow from the FTO into the semiconductor and reduce triiodide to iodide, which is opposite in sense to a photocurrent at voltages below V_{OC}. As TiO_2 nanoparticles are added to ZnO nanorods, if the CBM of ZnO is more negative than that of TiO_2, then electrons should transfer easily from ZnO into TiO_2, and the added surface area provided by the TiO_2 nanoparticles should increase the dark current. On the other hand, if TiO_2 has the more negative CBM, electron transfer into TiO_2 should be impeded, and the TiO_2 should reduce the dark current by reducing the ZnO surface area that is in contact with the electrolyte. The result shown in Figure 4. 10(a) is that the ZT film has more dark current than the Z film, which is consistent with ZnO having the more negative CBM. The dark current from ZT is close to that of a TiO_2-only film (T) of comparable surface area, based on the above dye desorption measurements. We note that some of the differences seen in Figure 4. 10 may reflect different reactivities of ZnO and TiO_2 toward I_3^-, as suggested by the longer electron lifetime observed in ZnO.[6]

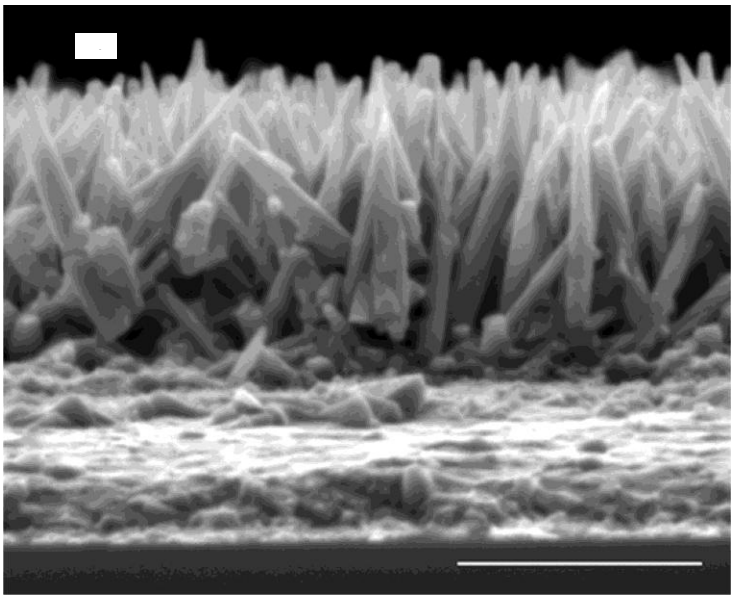

Figure 4. 11 ZnO nanorods (1 µm) grown atop a 30-layer LbL TiO_2 nanoparticulate film. Scale bar: 1 µm.

For the reverse experiment, we grew short (1-μm) ZnO nanorods on a TiO_2 film by adding two layers of a standard seed layer (drop-coating 5 mM zinc acetate in ethanol, allowing to evaporate, and heating at 350 °C) to a TiO_2 film followed by immersion in a ZnO CBD solution (the same as for the longer rods) at 90 °C for 4 h (Figure 4. 11). This TZ hybrid film should have more dark current than a plain T film if and only if ZnO has the more positive CBM. On the contrary, the addition of ZnO significantly reduces the dark current (Figure 4. 10 b). Both sets of results, then, are consistent with a more negative CBM for ZnO, which would tend to pose a barrier to the desired electron transfer from TiO_2 to ZnO (Figure 4. 12). Given the good TiO_2 coverage in the ZT films (see Figure 4. 4), it is likely that electrons photoinjected into TiO_2 can travel to the conducting glass substrate along a purely TiO_2 path on the outside of the nanorod. This allows high current in ZT samples in an I^-/I_3^- electrolyte, where electron diffusion lengths[31] are much longer than the nanorods in these samples (about 5 μm). However, in the presence of Fc/Fc^+, recombination claims many of these electrons, reducing the benefit of the TiO_2 nanoparticulate coating. The fact that ZT still outperforms Z (and T) in a Fc/Fc^+ electrolyte suggests that some electrons are able to transfer from TiO_2 to ZnO, perhaps due to a small energy barrier that can be thermally overcome by a fraction of the conduction band electrons at room temperature, resulting in slow transfer kinetics. Our laboratory is currently at work on strategies to eliminate this energy barrier.

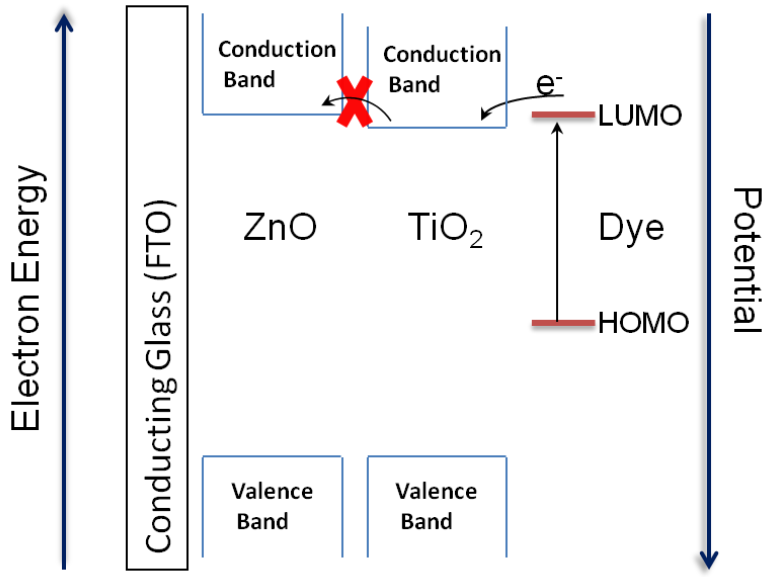

Figure 4. 12 Energy level schematic of the ZT hybrid film showing the energetics of the individual components used in the cell.

4.4 Conclusion

We have successfully synthesized a composite nanostructure consisting of ZnO nanorods coated with TiO_2 nanoparticles, using facile wet-chemical methods. A coating of three monolayers of TiO_2 nanoparticles increased the dye uptake of the film by a factor of 4 compared to ZnO nanorods only. Although a TiO_2-only film of similar dye loading outperforms the ZnO–TiO_2 film with I^-/I_3^- electrolyte, the nanocomposite film dramatically outperforms the TiO_2 film when using the fast-recombining Fc/Fc^+ electrolyte and modestly outperforms the ZnO nanorod-only film. Transfer of electrons from the TiO_2 to the ZnO is impeded by an energy barrier, as the conduction band minimum of ZnO lies at a slightly more negative potential than that of TiO_2, and more work is needed to remove this barrier. This nanocomposite photoanode points to a class of structures that can provide both fast transport and high surface area, enabling DSSCs that are tolerant of electrolytes with higher recombination rates than are found with the conventional iodide/triiodide couple.

4.5 References

1. B. O'Regan and M. Gratzel, "A low-cost, high-efficiency solar cell based on dye-sensitized colloidal TiO_2 films," *Nature,* 353[6346] 737-40 (1991).
2. G. Boschloo and A. Hagfeldt, "Characteristics of the Iodide/Triiodide Redox Mediator in Dye-Sensitized Solar Cells," *Accounts of Chemical Research,* 42[11] 1819-26 (2009).
3. J. Bisquert, D. Cahen, G. Hodes, S. Rühle, and A. Zaban, "Physical Chemical Principles of Photovoltaic Conversion with Nanoparticulate, Mesoporous Dye-Sensitized Solar Cells," *The Journal of Physical Chemistry B,* 108[24] 8106-18 (2004).
4. J. Nissfolk, K. Fredin, A. Hagfeldt, and G. Boschloo, "Recombination and Transport Processes in Dye-Sensitized Solar Cells Investigated under Working Conditions," *The Journal of Physical Chemistry B,* 110[36] 17715-18 (2006).
5. N. Kopidakis, K. D. Benkstein, J. van de Lagemaat, and A. J. Frank, "Transport-Limited Recombination of Photocarriers in Dye-Sensitized Nanocrystalline TiO_2 Solar Cells," *The Journal of Physical Chemistry B,* 107[41] 11307-15 (2003).
6. M. Quintana, T. Edvinsson, A. Hagfeldt, and G. Boschloo, "Comparison of Dye-Sensitized ZnO and TiO_2 Solar Cells: Studies of Charge Transport and Carrier Lifetime," *The Journal of Physical Chemistry C,* 111[2] 1035-41 (2006).
7. K. Keis, C. Bauer, G. Boschloo, A. Hagfeldt, K. Westermark, H. Rensmo, and H. Siegbahn, "Nanostructured ZnO electrodes for dye-sensitized solar cell applications," *Journal of Photochemistry and Photobiology A: Chemistry,* 148[1-3] 57-64 (2002).
8. F. Xu and L. Sun, "Solution-derived ZnO nanostructures for photoanodes of dye-sensitized solar cells," *Energy & Environmental Science,* 4[3] 818-41 (2011).

9. K. Keis, E. Magnusson, H. Lindström, S.-E. Lindquist, and A. Hagfeldt, "A 5% efficient photoelectrochemical solar cell based on nanostructured ZnO electrodes," *Solar Energy Materials and Solar Cells,* 73[1] 51-58 (2002).

10. M. Saito and S. Fujihara, "Large photocurrent generation in dye-sensitized ZnO solar cells," *Energy & Environmental Science,* 1[2] 280-83 (2008).

11. P. O'Brien, T. Saeed, and J. Knowles, "Speciation and the nature of ZnO thin films from chemical bath deposition," *Journal of Materials Chemistry,* 6[7] 1135-39 (1996).

12. L. Vayssieres, K. Keis, A. Hagfeldt, and S.-E. Lindquist, "Three-Dimensional Array of Highly Oriented Crystalline ZnO Microtubes," *Chemistry of Materials,* 13[12] 4395-98 (2001).

13. T. Yoshida, M. Tochimoto, D. Schlettwein, D. Wöhrle, T. Sugiura, and H. Minoura, "Self-Assembly of Zinc Oxide Thin Films Modified with Tetrasulfonated Metallophthalocyanines by One-Step Electrodeposition," *Chemistry of Materials,* 11[10] 2657-67 (1999).

14. B. O'Regan, V. Sklover, and M. Gratzel, "Electrochemical Deposition of Smooth and Homogeneously Mesoporous ZnO Films from Propylene Carbonate Electrolytes," *Journal of The Electrochemical Society,* 148[7] C498-C505 (2001).

15. L. Xu, Q. Chen, and D. Xu, "Hierarchical ZnO Nanostructures Obtained by Electrodeposition," *The Journal of Physical Chemistry C,* 111[31] 11560-65 (2007).

16. R. R. Bacsa, J. Dexpert-Ghys, M. Verelst, A. Falqui, B. Machado, W. S. Bacsa, P. Chen, S. M. Zakeeruddin, M. Graetzel, and P. Serp, "Synthesis and Structure–Property Correlation in Shape-Controlled ZnO Nanoparticles Prepared by Chemical Vapor Synthesis and their

Application in Dye-Sensitized Solar Cells," *Advanced Functional Materials,* 19[6] 875-86 (2009).

17. M. H. Huang, Y. Wu, H. Feick, N. Tran, E. Weber, and P. Yang, "Catalytic Growth of Zinc Oxide Nanowires by Vapor Transport," *Advanced Materials,* 13[2] 113-16 (2001).
18. L. Vayssieres, "Growth of Arrayed Nanorods and Nanowires of ZnO from Aqueous Solutions," *Advanced Materials,* 15[5] 464-66 (2003).
19. P. Wang, S. M. Zakeeruddin, P. Comte, R. Charvet, R. Humphry-Baker, and M. Grätzel, "Enhance the Performance of Dye-Sensitized Solar Cells by Co-grafting Amphiphilic Sensitizer and Hexadecylmalonic Acid on TiO_2 Nanocrystals," *The Journal of Physical Chemistry B,* 107[51] 14336-41 (2003).
20. A. G. Agrios, I. Cesar, P. Comte, M. K. Nazeeruddin, and M. Grätzel, "Nanostructured Composite Films for Dye-Sensitized Solar Cells by Electrostatic Layer-by-Layer Deposition," *Chemistry of Materials,* 18[23] 5395-97 (2006).
21. M. K. Nazeeruddin, S. M. Zakeeruddin, R. Humphry-Baker, M. Jirousek, P. Liska, N. Vlachopoulos, V. Shklover, C.-H. Fischer, and M. Grätzel, "Acid−Base Equilibria of (2,2‘-Bipyridyl-4,4‘-dicarboxylic acid)ruthenium(II) Complexes and the Effect of Protonation on Charge-Transfer Sensitization of Nanocrystalline Titania," *Inorganic Chemistry,* 38[26] 6298-305 (1999).
22. T. W. Hamann, O. K. Farha, and J. T. Hupp, "Outer-Sphere Redox Couples as Shuttles in Dye-Sensitized Solar Cells. Performance Enhancement Based on Photoelectrode Modification via Atomic Layer Deposition," *The Journal of Physical Chemistry C,* 112[49] 19756-64 (2008).

23. T. Daeneke, T.-H. Kwon, A. B. Holmes, N. W. Duffy, U. Bach, and L. Spiccia, "High-efficiency dye-sensitized solar cells with ferrocene-based electrolytes," *Nat Chem,* 3[3] 211-15 (2011).

24. R. Vijayalakshmi and V. Rajendran, "Synthesis and characterization of nano-TiO_2 via different methods," *Arch. Appl. Sci. Res.*, 4 (2012).

25. J.-A. He, R. Mosurkal, L. A. Samuelson, L. Li, and J. Kumar, "Dye-sensitized Solar Cell Fabricated by Electrostatic Layer-by-Layer Assembly of Amphoteric TiO_2 Nanoparticles," *Langmuir,* 19[6] 2169-74 (2003).

26. E. Dell'Orto, L. Raimondo, A. Sassella, and A. Abbotto, "Dye-sensitized solar cells: spectroscopic evaluation of dye loading on TiO_2," *Journal of Materials Chemistry,* 22[22] 11364-69 (2012).

27. X. Xin, M. Scheiner, M. Ye, and Z. Lin, "Surface-Treated TiO_2 Nanoparticles for Dye-Sensitized Solar Cells with Remarkably Enhanced Performance," *Langmuir,* 27[23] 14594-98 (2011).

28. L. M. Peter, A. B. Walker, G. Boschloo, and A. Hagfeldt, "Interpretation of Apparent Activation Energies for Electron Transport in Dye-sensitized Nanocrystalline Solar Cells," *The Journal of Physical Chemistry B,* 110[28] 13694-99 (2006).

29. E. Galoppini, J. Rochford, H. Chen, G. Saraf, Y. Lu, A. Hagfeldt, and G. Boschloo, "Fast Electron Transport in Metal Organic Vapor Deposition Grown Dye-sensitized ZnO Nanorod Solar Cells," *The Journal of Physical Chemistry B,* 110[33] 16159-61 (2006).

30. V. O. Williams, N. C. Jeong, C. Prasittichai, O. K. Farha, M. J. Pellin, and J. T. Hupp, "Fast Transporting ZnO–TiO_2 Coaxial Photoanodes for Dye-Sensitized Solar Cells Based on ALD-Modified SiO2 Aerogel Frameworks," *ACS Nano,* 6[7] 6185-96 (2012).

31. H. K. Dunn and L. M. Peter, "How Efficient Is Electron Collection in Dye-Sensitized Solar Cells? Comparison of Different Dynamic Methods for the Determination of the Electron Diffusion Length," *The Journal of Physical Chemistry C*, 113[11] 4726-31 (2009).

Chapter 5
Facile Synthesis of $Zn_{1-x}Co_xO$/ZnO Core/Shell Nanostructures and Their Application to Dye-Sensitized Solar Cells

Abstract

Heterostructures consisting of Co-doped ZnO nanorod cores encased in an undoped ZnO shell and MgO were successfully synthesized to serve as photoanodes for dye-sensitized solar cells (DSSCs) by a two-step chemical bath deposition (CBD) technique in water at 90 °C. Doping ZnO with Co^{2+} has been shown to reduce its bandgap, and our photoelectrochemical characterization indicates a ca. 0.1 V positive shift in the conduction band edge potential of the Co-doped ZnO compared to pure ZnO. Adding a shell of undoped ZnO, followed by dye sensitization, results in a highly favorable structure in which electrons injected from the dye into the ZnO then step down in energy into the Co-doped core, where the electron is transported to the collector while the ZnO shell acts as a barrier to recombination with the electrolyte. MgO shell increases the dye loading preventing the formation of the Zn^{2+}- dye complex. Incorporation of the core/shell nanostructures into the DSSCs resulted in large improvements in photocurrent and photovoltage in comparison to the pure ZnO nanorod-based DSSCs. SEM and XRD characterization indicate incorporation of the Co^{2+} into the ZnO matrix, without separation of the Co into other phases, providing no energy barriers. In addition, device performance of DSSCs based on these films has been compared using a standard iodide/triiodide electrolyte versus ferrocene/ferrocenium as a model alternative redox couple with fast recombination kinetics, to

probe the potential for heterostructures of this type to cope with such redox couples by reducing recombination rates.

5.1 Introduction

Dye sensitized solar cells (DSSCs)[1] are low-cost alternatives to silicon photovoltaics. The conventional DSSC consists of two sandwiched pieces of conducting glass, one of them coated with mesoporous layer of nanoparticulate TiO_2 with a self-assembled monolayer of chemisorbed dye molecules, filled with an electrolyte for dye regeneration. The dye is a transition metal complex or organic chromophore that harvests sunlight by absorbing strongly in visible region of the solar spectrum. The principal photovoltaic losses in the DSSCs are due to incomplete light harvesting, recombination of the photoinjected electrons with the electrolyte and the overpotential required for dye regeneration. Ruthenium complex dyes like N719, N3 and the black dye exhibit high efficiency with the I^-/I_3^- redox couple, but there is little room for improvement in light harvesting in the visible range.

ZnO, TiO_2 and SnO_2 nanoparticles are commonly used photoanode materials in DSSCs. In a 10 μm thick nanoparticulate film an electron visits about 10^6 nanoparticles on average before reaching the FTO surface.[2] If the electron transport is not fast enough, electrons will recombine with the redox species decreasing the efficiency of the DSSCs. One dimensional ZnO nanorods are promising alternative to nanparticlulate film due to fast electron transport and decrease in the recombination.[3] However, the main disadvantage of nanorods is lower surface area than a nanoparticle film for adsorption of light-harvesting molecules. In addition, dyes partially dissolve the ZnO, forming a deleterious Zn^{2+}–dye surface complex.[4]

Cobalt doped ZnO nanostructures with longer electron lifetime are synthesized and applied in the DSSCs for the first time, but found increase in the recombination of the electrons due to the presence of the cobalt. Cobalt doped ZnO nanorods have higher electron mobility of 75 cm^2 /V-s when compared to 8.85 cm^2 /V.s $_{of}$ ZnO.[5, 6] The two ways to improve the efficiency of the CoZnO based DSSCs is by adding a protective layer on the CoZnO and improve the stability of the ZnO nanorods. ZnO nanorod based core shell nanostructures of ZnO/TiO_2[7, 8, 9], ZnO/ZnS[10, 11], ZnO/CdSe[12], ZnO/ZSe[13], ZnO/ZnO[14] and Cu doped ZnO/ZnS[15] are synthesized. ZnO-TiO_2 core-shell nanostructures are synthesized for fast electron transport and high surface area, but there exist energy barrier between the ZnO and TiO_2.[8] Other core-shell nanostructures of TiO_2/NbO_5[16], TiO_2/SnO_2 [17]and TiO_2/ZnO[18] are synthesized but with limited success due to difficulty in ideal coverage, thickness and crystalinity of the shell material.

The morphology evolution of the ZnO coated on the ZnCoO nanorod and its effect on the performance of the DSSCs were followed by varying the reaction time during the shell deposition by CBD. The optimum thickness of the shell was evaluated based on the photocurrent density. The results show that the compact ZnO shell can effectively relay photogenerated electrons from the excited dye molecules to the conduction band of the $Zn_{1-x}Co_xO$, suppressing recombination of the injected electrons with the redox couple in the electrolyte.

Incorporation of the core/shell nanostructures into the DSSCs resulted in large improvements in photocurrent and photovoltage in comparison to the pure ZnO nanorod-based DSSCs. SEM and XRD characterization indicate incorporation of the Co^{2+} into the ZnO matrix, without separation of the Co into other phases, providing no energy barriers. In addition, device performance of DSSCs based on these films has been compared using a standard iodide/triiodide electrolyte versus ferrocene/ferrocenium as a model alternative redox couple with fast recombination

kinetics, to probe the potential for heterostructures of this type to cope with such redox couples by reducing recombination rates.

MgO a wide band gap oxide (6.0-7.8 eV) is used as a shell for the CoZnO nanorods. MgO is deposited on the CoZnO nanorods using low temperature chemical bath deposition. Previous reports indicate the increase in dye loading and decrease in recombination after MgO deposition.[19] The presence of MgO increased the dye loading due to the coarse surface of the MgO. The effect of the ZnO shell deposition time on the performance of the CoZnO nanorods will be presented.

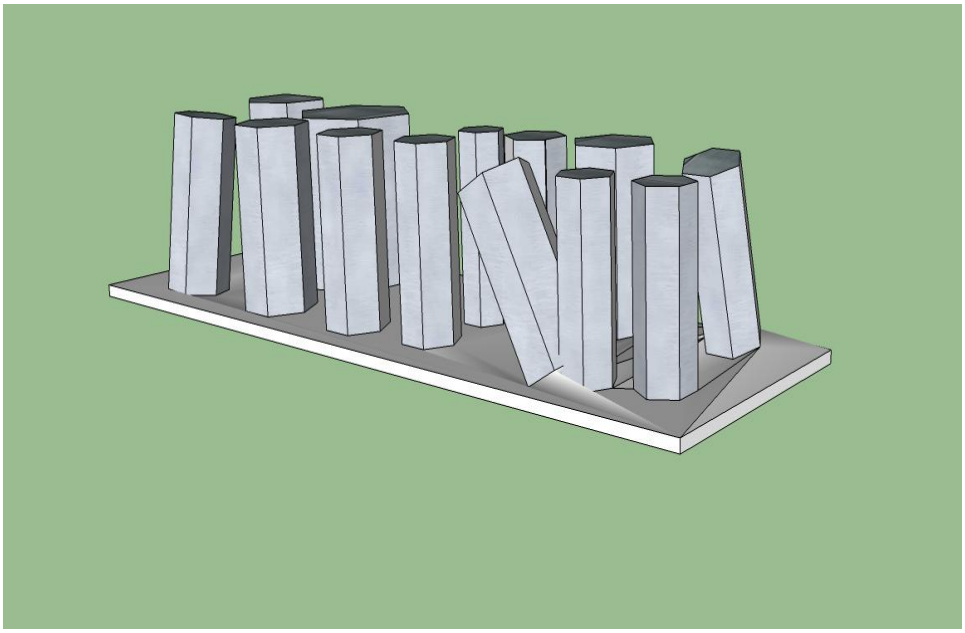

Figure 5. 1 Schematic of core-shell nanostructures

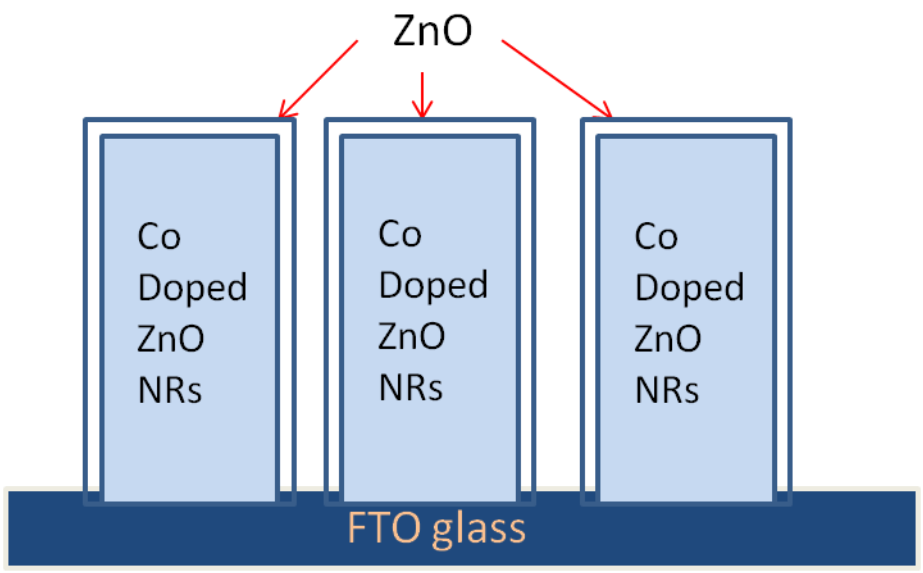

Figure 5. 2 Schematic of Core-shell nanostructures cross-section.

5.2 Experimental

Reagents and Materials. Zinc nitrate hexahydrate, hexamethylenetetramine (HMTA), polyethyleneimine and ethanol were purchased from Sigma-Aldrich (USA) and were ACS grade. N719 was purchased from Dyesol (Australia). SnO_2: F glass (FTO, transmission> 80% in the visible spectrum; sheet resistance 8 Ω /□) was purchased from Hartford Tec Glass (USA).

ZnO Seed Crystal Preparation. The formation of ZnO seeds began with the dissolution of 5 mM zinc acetate dihydrate in ethanol by stirring for 3 hours at room temperature.[20] Varying amounts of deionized water were added. The solution was stirred for another 3.5 hours and then transferred into preheated furnace at 80˚C for 12 hours. After cooling to room temperature, this finished seed precursor solution was drop-cast on a precleaned FTO substrate and allowed to dry. The substrate was then heated on a titanium hot plate at 350°C for 20 minutes to form the ZnO seed layer. After cooling, the drop-casting, air-drying and heating were repeated to increase the number of seeds on the substrate.

$Zn_{0.9}Co_{0.1}O$ Nanorod Synthesis. Nanorods were grown from the ZnO seeds by chemical bath deposition. The seeded FTO substrates were placed in an aqueous solution of 45 mM zinc nitrate hexahydrate, 5mM cobalt nitrate hexahydrate, 50mM hexamethylenetetramine and 6mM polyethyleneimine in a 100-ml glass bottle at 90°C for 24 hours.

ZnO Shell Synthesis. ZnO shell is grown on $Zn_{0.9}Co_{0.1}O$ Nanorods by chemical bath deposition. FTO substrates with $Zn_{0.9}Co_{0.1}O$ nanorods were placed in an aqueous solution of 50 mM zinc nitrate hexahydrate and hexamethylenetetramine and 6mM polyethyleneimine in a 100-ml glass bottle at 90°C for 3 hours.

MgO Shell Synthesis. MgO shell is grown on $Zn_{0.9}Co_{0.1}O$ Nanorods by chemical bath deposition. FTO substrates with $Zn_{0.9}Co_{0.1}O$ nanorods were placed in an aqueous solution of 50 mM magnesium nitrate hexahydrate and hexamethylenetetramine and 6mM polyethyleneimine in a 100-ml glass bottle at 99°C for 40 minutes.

Sensitization. After sintering, films were allowed to cool to 100°C then immediately immersed in 0.3 mM N719 in ethanol. After 12 hours they were removed and rinsed in acetonitrile and dried in air.

Solar Cell Assembly. Each sensitized electrode was sealed against a counter electrode on a hot plate at 120°C using a hot-melt plastic frame (Solaronix, Meltonix 1170, 25 μm thick), applying light pressure with a glass rod. The assembled cell was filled with electrolyte through two holes in the counter electrode. The holes were then sealed using hot-melt plastic and a thin glass cover slide. The exposed conducting glass leads of each electrode were coated with copper tape (3M) for improved electrical conductivity.

Electrolyte Composition. Minimal electrolyte recipes were used to exclude complications due to interactions with the various additives that are commonly used. Iodide/triiodide (I^-/I_3^-) electrolyte was prepared with 0.5 M tetrabutylammonium iodide and 0.05 M iodine (I_2) in 3-methoxypropionitrile. The ferrocene/ferrocenium (Fc/Fc^+) electrolyte contained 0.1 M ferrocene and 0.05 M ferrocenium hexafluorophosphate (Aldrich) in 3-methoxypropionitrile. The Fc/Fc^+ electrolyte was prepared fresh and deoxygenated by bubbling nitrogen 10 minutes prior to cell fabrication to minimize reaction of ferrocene with oxygen.

Transient Measurements. Measurements of electron transport time were made using a set of National Instruments components in a PXIe chassis capable of high-resolution analog voltage output and digitized input. A square-wave modulation was applied to a white-light LED that was used to illuminate a DSSC. The modulation amplitude produced a <10% change in DSSC current, which is linear with light intensity. The DSSC was operated in series with a 65-Ω resistor and the voltage across this resistor was measured. The current is determined by $I=V/R$. We refer to this as a "quasi-short-circuit" mode, as the small voltages measured (<20 mV) were close to the short-circuit condition, compared to open circuit voltages of hundreds of millivolts. At least 50 transients were averaged for noise reduction.

Solar Cell Characterization. Current–voltage (*J*–*V*) measurements were made using Keithley 2400 source/meter controlled by a PC, while irradiating at 100 mW/cm^2 (1 sun) with AM 1.5G simulated sunlight produced by a solar simulator (Newport 91160), calibrated against a silicon reference cell with KG5 filter (PV Measurements, Inc., Boulder, CO). The DSSC active area was 1 cm^2.

Characterization. The morphology and elemental distribution of CoZnO nanorods was investigated by scanning electron microscopy (FEI Quanta FEG250 SEM in High vacuum mode)

attached with Energy dispersive X-ray spectroscopy(EDS) and characterized by X-ray powder diffraction (XRD) using a Bruker D8 Advance X-ray diffractometer using Cu K_radiation (λ = 0.154178 nm) at a scanning rate of 0.04˚ s^{-1} in the 2θ range from 10˚ to 90˚. Photoluminescence measurements were performed using a Horbia Jobin Yvon Fluorolog-3 spectroflourometer with an excitation wavelength of 350 nm and a scan rate of 1 nm/s.

5.3 Results and discussion

5.3.1 $Zn_{0.9}Co_{0.1}O$ nanorods

Cobalt doped ZnO nanostructures with fast electron transport are synthesized and applied in the DSSCs for the first time, but found increase in the recombination of the electrons due to the presence of the cobalt. ZnO has low recombination when compared to TiO_2[18]. Core-shell nanostructures of $Zn_{0.9}Co_{0.1}O$ – ZnO have been synthesized to reduce the recombination and take advantage of the fast electron transport of the cobalt doped ZnO. For an ideal core-shell nanostructure to block the recombination the conduction band edge of the shell material should be more negative than the core material, and less than the LUMO of the dye to efficient electron injection. Complete coverage of the shells is needed for reducing the recombination. Figure 5. 3 below show the change in the coverage with the deposition time from 1 hour to 3 hours.

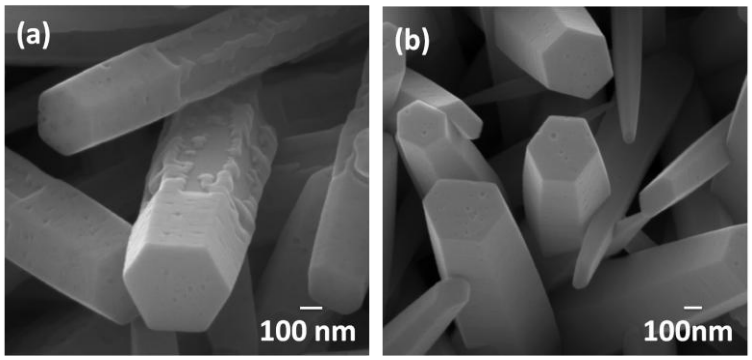

Figure 5. 3 Cobalt doped ZnO nanorods with (a) non-uniform (b) uniform ZnO shell growth.

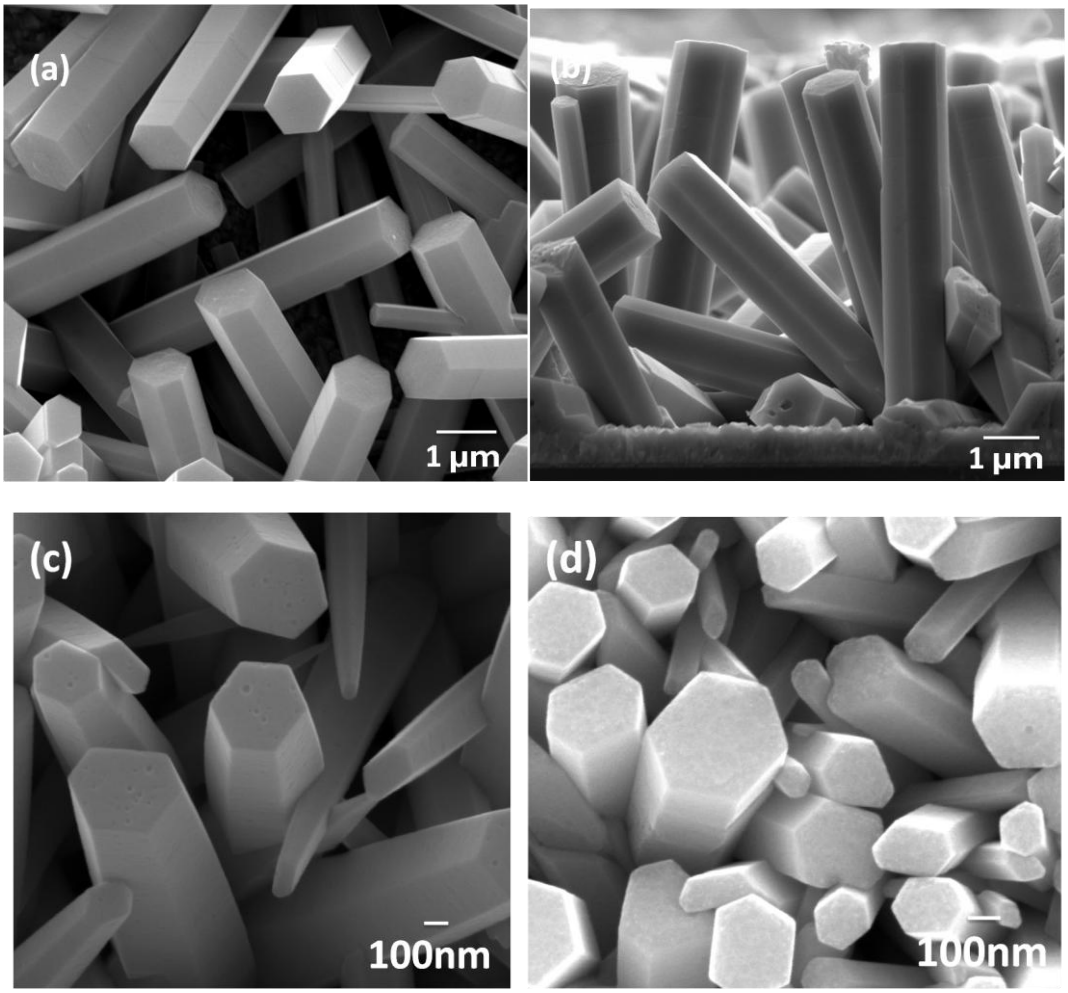

Figure 5. 4 SEM Image of (a) 10% cobalt doped ZnO nanorods, (b) Cross section of 10% cobalt doped ZnO nanorods (c) 10% cobalt doped ZnO nanorod coated with ZnO and (d) 10% cobalt doped ZnO nanorods coated with MgO.

5.5.2 Electron Lifetime. Figure 5. 5 shows representative transients for intensity modulated photovoltage spectroscopy. Each transient is well fit by a single exponential decay of the form $y = y_0 + Aexp(-t/\tau_{tr})$, where τ_{tr} is the characteristic time for electron transport. The fitted time constants τ_n over a range of light intensities are plotted against the corresponding voltages.

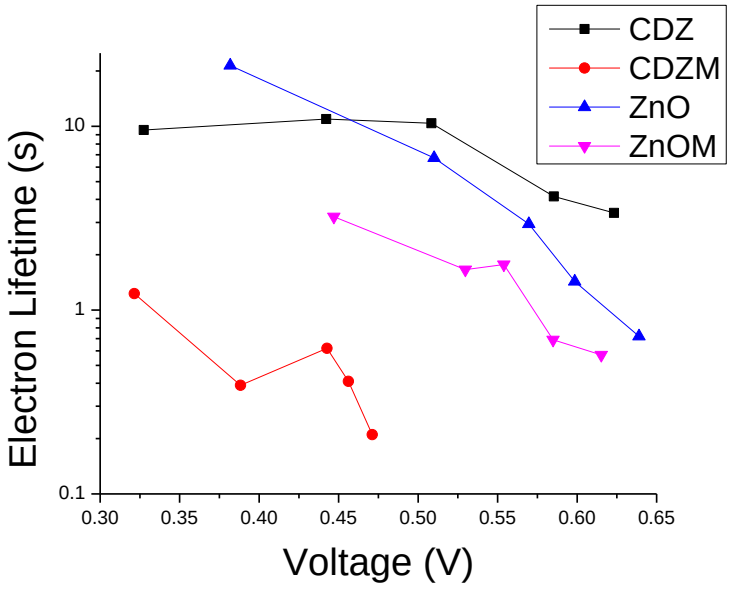

Figure 5. 5 Electron lifetime measurements of core-shell structures.

From the Figure 5. 5 the electron lifetime of the ZnO increased after cobalt doping. The increase in electron lifetime indicates better electron collection before they can recombine. The presence of cobalt in the ZnO matrix increased the lifetime. The decrease of the lifetime with the increase of the forward bias is due to depletion region on the ZnO nanorods. The electron transport occurs in the core of the ZnO nanorods.[21, 22] The potential across the depletion regions decreases and radius of the neutral region increases as the forward bias increases resulting in the surface get involved in the transport processes.

Once the surface gets involved in the electron transport the surface related defects will increase the recombination of the electrons with the electrolyte.[23]

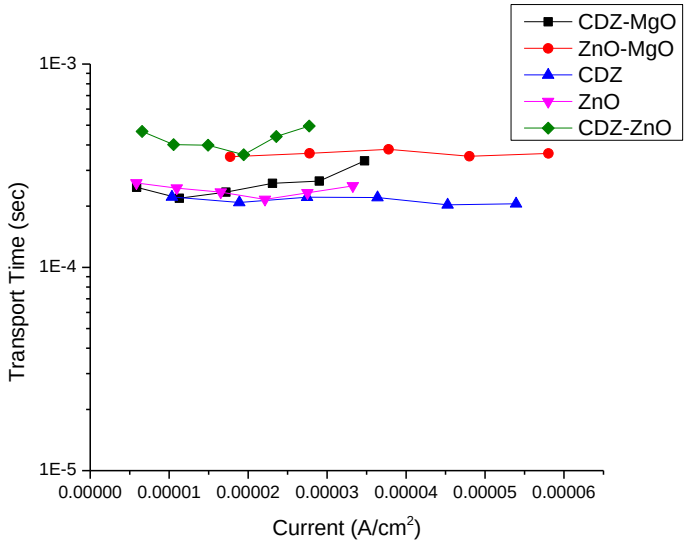

Figure 5. 6 Electron transport Measurements of core-shell nanostructures.

5.3.4 Device Performance

The presence of MgO shell increased the short circuit current from 0.4 mA/cm^2 to 1.35 mA/cm^2 in I^-/I_3^- electrolyte and from 0.59 mA/cm^2 to 1.0 mA/cm2 in Fc/Fc^+ electrolyte. Cobalt doped ZnO nanorods and ZnO have higher short circuit current in fast recombining Fc/Fc^+ electrolyte than in $I^-I_3^-$ electrolyte. The lower photocurrent than expected is due to lower injection rate after the MgO shell.[24] The dye loading after MgO coating have negligible influence in the DSSC.[24] The photocurrent of $Co_{0.1}Zn_{0.9}O$/MgO core-shell nanostructures is higher in Fc/Fc^+ is due to longer electron lifetime of the $Co_{0.1}Zn_{0.9}O$ nanorods. The lower voltage of the $Co_{0.1}Zn_{0.9}O$ nanorods is due to decrease of the conduction band edge after doping pure ZnO.

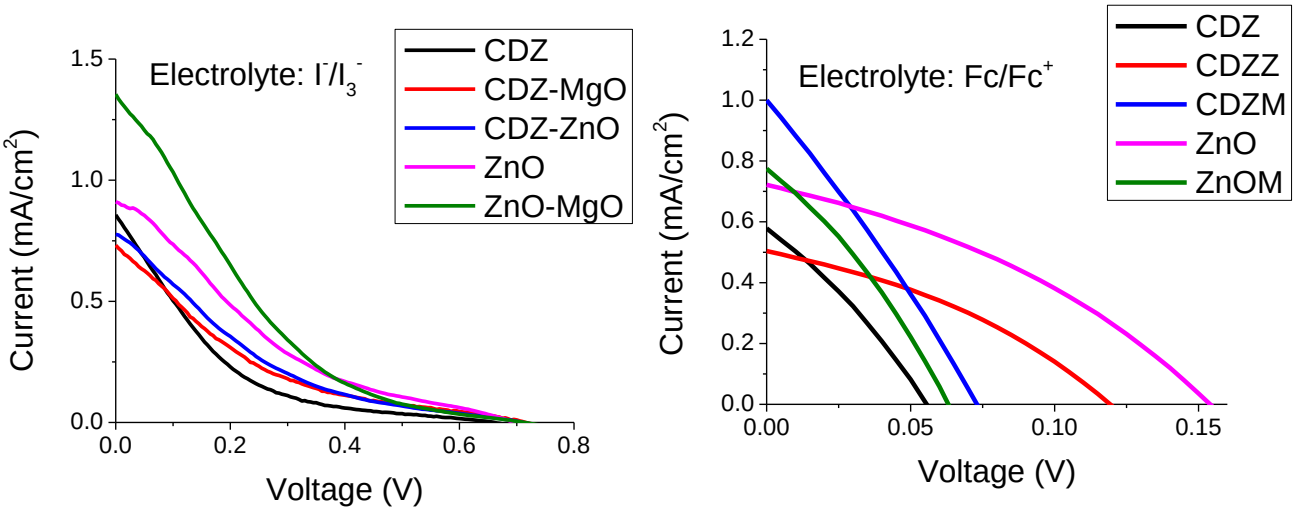

Figure 5. 7 I-V Measurements CS structures with ZnO and MgO shell in (a) I^-/I_3^- electrolyte (b) Fc/Fc^+ electrolyte.

5.3.5 Effect of Shell Thickness

The thickness of the shell is varied from 50 to 200 nm by changing the shell growth time from 3 hrs to 6 hrs for analyzing the ideal shell thickness. The CS structures with shell thickness of 100 nm performed better in Fc/Fc^+ electrolyte, whereas in I^-/I_3^- electrolyte CS structures with 50 nm thickness performed better than 100 nm thick shell films. In Fc/Fc^+ fast recombining electrolyte ideal coverage and shell thickness plays an important role, uncovered $Co_{0.1}Zn_{0.9}O$ can increase the recombination and decrease the photocurrent.

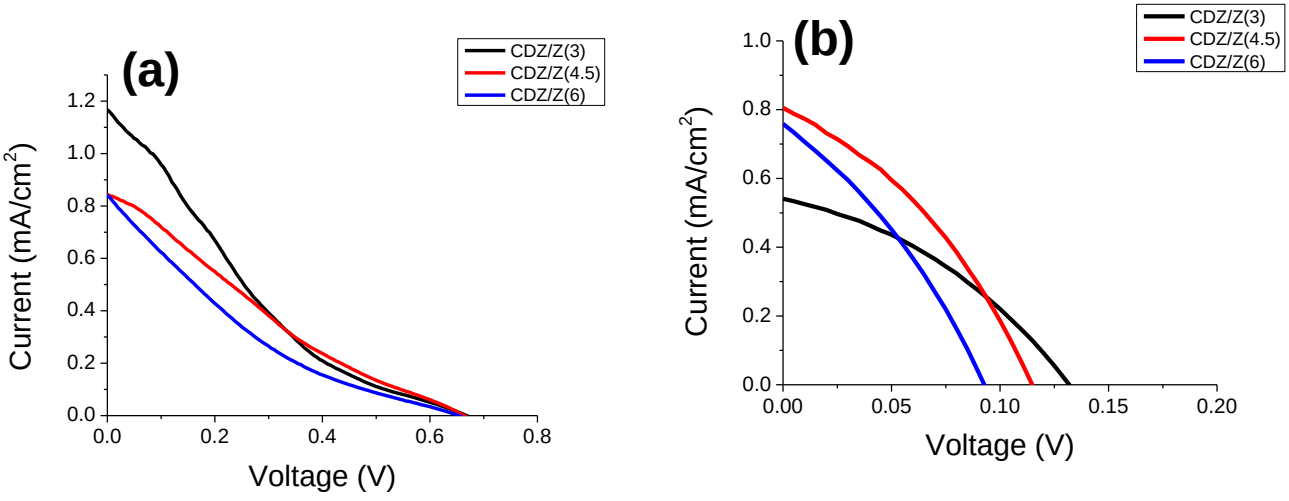

Figure 5. 8 Effect of shell thickness (a) I^-/I_3^- electrolyte (b) Fc/Fc^+ electrolyte.

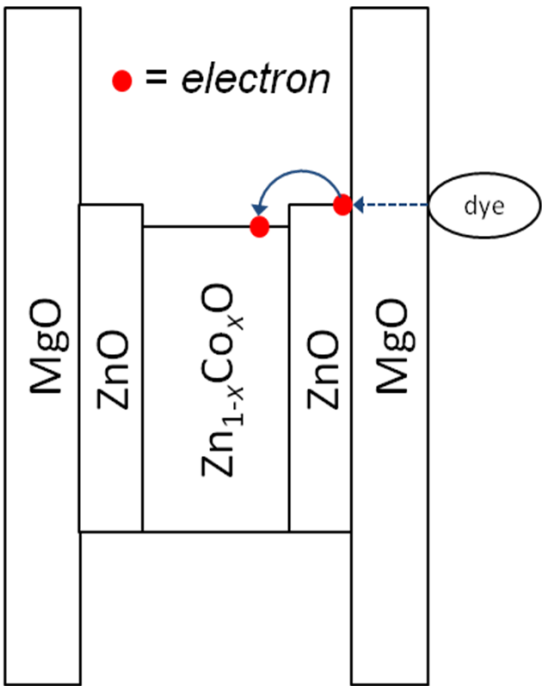

Figure 5. 9 Band diagram of the core-shell nanostructures.

5.4 Conclusions

Core-Shell nanostructures of Co doped ZnO with ZnO and MgO shells are successfully synthesized using low temperature chemical bath deposition. Co doped ZnO nanorods have longer lifetime and photocurrent in fast recombining Fc/Fc^+ electrolyte and conventional I^-/I_3^- electrolyte. Co-doped ZnO nanorod arrays were prepared and their structure, morphology, and electrochemical properties were studied. We have successfully fabricated cylindrical core-shell nanostrucres of CoZnO/ZnO. The decrease in the current of the DSSC with Co doped ZnO nanorod as photo anode is due to Co acting as recombination site, thus increasing the recombination. Photoelectrochemical measurements indicate the decrease of the band gap of Co doped ZnO. The positive movement of the conduction band of the Co doped ZnO decreased the open circuit photovoltage. The DSSC with the CoZnO/ZnO core/shell nanowires exhibited a significant increase in cell performance compared with that with nanowires without a shell

structure. The increase in photocurrent in core-shell nanostructures is due to prevention of the contact of the electrolyte and the electron transporting core-material, which suppresses recombination of injected electrons.

5.5 References

1. B. O'Regan and M. Gratzel, "A low-cost, high-efficiency solar cell based on dye-sensitized colloidal TiO_2 films," *Nature*, 353[6346] 737-40 (1991).
2. N. Kopidakis, K. D. Benkstein, J. van de Lagemaat, and A. J. Frank, "Transport-Limited Recombination of Photocarriers in Dye-Sensitized Nanocrystalline TiO_2 Solar Cells," *The Journal of Physical Chemistry B*, 107[41] 11307-15 (2003).
3. M. Law, L. E. Greene, J. C. Johnson, R. Saykally, and P. Yang, "Nanowire dye-sensitized solar cells," *Nat Mater*, 4[6] 455-59 (2005).
4. H. Horiuchi, R. Katoh, K. Hara, M. Yanagida, S. Murata, H. Arakawa, and M. Tachiya, "Electron Injection Efficiency from Excited N3 into Nanocrystalline ZnO Films: Effect of ($N3-Zn^{2+}$) Aggregate Formation," *The Journal of Physical Chemistry B*, 107[11] 2570-74 (2003).
5. C. Xu, P. Shin, L. Cao, and D. Gao, "Preferential Growth of Long ZnO Nanowire Array and Its Application in Dye-Sensitized Solar Cells," *The Journal of Physical Chemistry C*, 114[1] 125-29 (2009).
6. Z. Y. Zhang, C. H. Jin, X. L. Liang, Q. Chen, and L. M. Peng, "Current-voltage characteristics and parameter retrieval of semiconducting nanowires," *Applied Physics Letters*, 88[7] 073102-3 (2006).

7. L. E. Greene, M. Law, B. D. Yuhas, and P. Yang, "ZnO−TiO_2 Core−Shell Nanorod/P3HT Solar Cells," *The Journal of Physical Chemistry C,* 111[50] 18451-56 (2007).

8. V. Manthina, J. P. Correa Baena, G. Liu, and A. G. Agrios, "ZnO–TiO_2 Nanocomposite Films for High Light Harvesting Efficiency and Fast Electron Transport in Dye-Sensitized Solar Cells," *The Journal of Physical Chemistry C,* 116[45] 23864-70 (2012).

9. M. Law, L. E. Greene, A. Radenovic, T. Kuykendall, J. Liphardt, and P. Yang, "ZnO−Al2O3 and ZnO−TiO_2 Core−Shell Nanowire Dye-Sensitized Solar Cells," *The Journal of Physical Chemistry B,* 110[45] 22652-63 (2006).

10. L. Liu, Y. Chen, T. Guo, Y. Zhu, Y. Su, C. Jia, M. Wei, and Y. Cheng, "Chemical Conversion Synthesis of ZnS Shell on ZnO Nanowire Arrays: Morphology Evolution and Its Effect on Dye-Sensitized Solar Cell," *ACS Applied Materials & Interfaces,* 4[1] 17-23 (2011).

11. S. Saha, S. Sarkar, S. Pal, and P. Sarkar, "Tuning the Energy Levels of ZnO/ZnS Core/Shell Nanowires To Design an efficient Nanowire-Based Dye-Sensitized Solar Cell," *The Journal of Physical Chemistry C,* 117[31] 15890-900 (2013).

12. Y. Chen, L. Wei, G. Zhang, and J. Jiao, "Open structure ZnO/CdSe core/shell nanoneedle arrays for solar cells," *Nanoscale Research Letters,* 7[1] 516 (2012).

13. Y. Zhang, D. Li, Z. Wu, J. Zheng, X. Lin, H. Zhan, S. Li, J. Kang, J. Bleuse, L. Grenet, D. Rapisarda, and H. Mariette, "ZnO/ZnSe Type II Core-Shell Nanowire Array Solar Cell," *MRS Online Proceedings Library,* 1396 null-null (2012).

14. E. Guillén, E. Azaceta, A. Vega-Poot, J. Idígoras, J. Echeberría, J. A. Anta, and R. Tena-Zaera, "ZnO/ZnO Core–Shell Nanowire Array Electrodes: Blocking of Recombination

and Impressive Enhancement of Photovoltage in Dye-Sensitized Solar Cells," *The Journal of Physical Chemistry C,* 117[26] 13365-73 (2013).

15. C. Liu, Z. Liu, J. Li, Y. Li, J. Han, Y. Wang, Z. Liu, and J. Ya, "Cu-doping ZnO/ZnS nanorods serve as the photoanode to enhance photocurrent and conversion efficiency," *Microelectronic Engineering,* 103[0] 12-16 (2013).
16. K. Sayama, H. Sugihara, and H. Arakawa, "Photoelectrochemical Properties of a Porous Nb2O5 Electrode Sensitized by a Ruthenium Dye," *Chemistry of Materials,* 10[12] 3825-32 (1998).
17. S. Chappel, S.-G. Chen, and A. Zaban, "TiO_2-Coated Nanoporous SnO_2 Electrodes for Dye-Sensitized Solar Cells," *Langmuir,* 18[8] 3336-42 (2002).
18. N. G. Park, M. G. Kang, K. M. Kim, K. S. Ryu, S. H. Chang, D. K. Kim, J. van de Lagemaat, K. D. Benkstein, and A. J. Frank, "Morphological and Photoelectrochemical Characterization of Core−Shell Nanoparticle Films for Dye-Sensitized Solar Cells: Zn−O Type Shell on SnO_2 and TiO_2 Cores," *Langmuir,* 20[10] 4246-53 (2004).
19. H. S. Jung, J.-K. Lee, M. Nastasi, S.-W. Lee, J.-Y. Kim, J.-S. Park, K. S. Hong, and H. Shin, "Preparation of Nanoporous MgO-Coated TiO_2 Nanoparticles and Their Application to the Electrode of Dye-Sensitized Solar Cells," *Langmuir,* 21[23] 10332-35 (2005).
20. L. Spanhel and M. A. Anderson, "Semiconductor clusters in the sol-gel process: quantized aggregation, gelation, and crystal growth in concentrated zinc oxide colloids," *Journal of the American Chemical Society,* 113[8] 2826-33 (1991).
21. C. He, Z. Zheng, H. Tang, L. Zhao, and F. Lu, "Electrochemical Impedance Spectroscopy Characterization of Electron Transport and Recombination in ZnO Nanorod Dye-Sensitized Solar Cells," *The Journal of Physical Chemistry C,* 113[24] 10322-25 (2009).

22. J. Bisquert, "Theory of the Impedance of Electron Diffusion and Recombination in a Thin Layer," *The Journal of Physical Chemistry B,* 106[2] 325-33 (2001).

23. Y. Xie, P. Joshi, S. B. Darling, Q. Chen, T. Zhang, D. Galipeau, and Q. Qiao, "Electrolyte Effects on Electron Transport and Recombination at ZnO Nanorods for Dye-Sensitized Solar Cells," *The Journal of Physical Chemistry C,* 114[41] 17880-88 (2010).

24. P. Docampo, P. Tiwana, N. Sakai, H. Miura, L. Herz, T. Murakami, and H. J. Snaith, "Unraveling the Function of an MgO Interlayer in Both Electrolyte and Solid-State SnO_2 Based Dye-Sensitized Solar Cells," *The Journal of Physical Chemistry C,* 116[43] 22840-46 (2012).

Chapter 6
Band edge engineering of semiconductors for Dye-sensitized solar cells

Abstract

Cobalt doped ZnO nanorods with 10% doping have been synthesized by low temperature chemical bath deposition technique successfully without phase separation on fluorine doped tin oxide (FTO) glass. Zr doped TiO_2 is synthesized using the hydrolysis technique. The materials are characterized optically using photoluminescence and diffuse reflectance and photoelecrochemically using three-electrode measurement setup to verify the shift in the conduction band edge of the doped ZnO and TiO_2. The core-shell nanostructures combining these two materials is synthesized and characterized. DSSC fabricated with the core-shell nanostructures using fast recombining Fc/Fc^+ electrolyte show faster electron transport, better electron injection and reduced recombination. Band edge engineering improved the electron transport and decreased the recombination.

6.1 Introduction

The application of the 1-D nanostructures of metal oxides is very promising in dye sensitized solar cells[1] and water splitting[2] where electron transport is principal in these applications. ZnO is introduced[3, 4, 5] as a highly favorable material for application in DSSCs since it can be grown in monocrystalline nanorods using facile methods, its electron mobility is high,[6] and its band edge energies are very close to those of TiO_2.[7] ZnO-TiO_2 core-shell nanostructures[8, 9, 10] are synthesized to utilize fast electron transport of ZnO and high surface area of TiO_2 nanoparticles, but there exists an energy barrier preventing electron injection from TiO_2 nanoparticles to ZnO nanorods.[11] Difficulty in synthesis of shells ideal thickness and coverage is also preventing the progress in core-shell nanostructures. For an ideal core-shell nanostructure the conduction band potential of the shell material should be more negative than that of the core material. In DSSCs the conduction band potential of the shell should be in between the core material and excited state of the dye. For preventing the energy barrier in the ZnO-TiO_2 core-shell nanostructures either the conduction band edge of the TiO_2 should be raised or that of the ZnO has to be lowered as shown in Figure 6. 1.

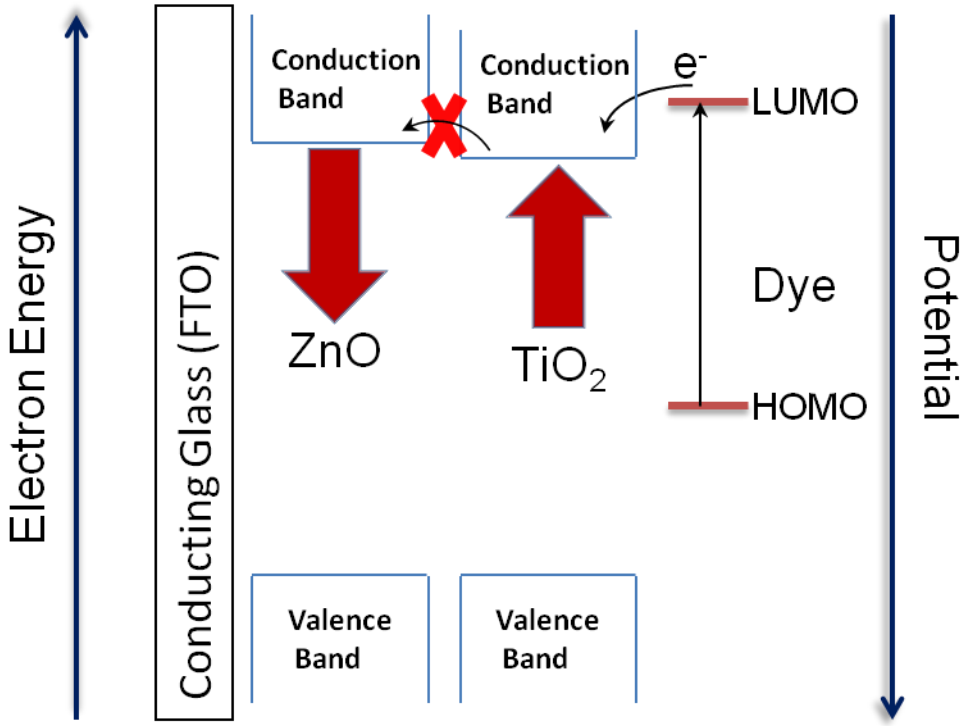

Figure 6. 1 Band energy level schematic at photoanode.

For lowering the conduction band edge of the ZnO we doped with cobalt and doped TiO_2 with zirconium to raise the conduction band edge. In this report we will discuss the effect of doping on the performance of the DSSCs in I^-/I_3^- electrolyte and fast recombining Fc/Fc^+ electrolyte.

6.2 Experimental

Reagents and Materials. Except where noted all chemicals were purchased from Sigma-Aldrich and were ACS grade or better. N719 was purchased from Dyesol (Australia). SnO_2: F glass (FTO, transmission> 80% in the visible spectrum; sheet resistance 8 Ω /□) was purchased from Hartford Glass Co (U.S.A).

Electrode Fabrication. Cobalt doped ZnO nanorods were synthesized by a two-step chemical bath deposition (CBD) technique.[12]A modified seed solution was used for the growth of nanorods optimized for subsequent TiO_2 deposition. ZnO seeds were synthesized by dissolving 5mM Zinc acetate dihydrate in ethanol by stirring on hotplate for 3 hours at room temperature. After 3 hours of dissolving ZnO seeds were hydrolyzed by adding 0.8M of deionized water to the seed solution. The solution was stirred for 3 hours on the hotplate and then transferred into preheated oven at 80˚C for 12 hours. The modified seed layer solution and its effect on ZnO nanorod growth is explained in detail in our future publication. Slides of borosilicate glass with a conducting SnO_2:F (FTO) layer were cut into 25 x 50 mm pieces and cleaned by 10 min sonication in a detergent solution (5% RBS-25 in water) followed by ethanol. The seed solution was drop-coated on precleaned FTO. Immediately after ethanol visibly evaporated from the substrate, the substrate was rinsed with reagent ethanol and dried with nitrogen. The seed layer process was repeated twice. Subsequently, the seeded FTO glass was heated at 350°C on a titanium hot plate for 30 min. CBD followed by preparing an aqueous solution of 45 mM zinc nitrate hexahydrate, 5mM cobalt nitrate hexahydrate, 50 mM hexamethylenetetramine and 6 mM polyethyleneimine in an ice bath. Initially zinc nitrate hexahydrate and hexamethylentetramine were dissolved in deionized water, stirred for 10 min. Then cobalt nitrate hexahydrate is added to the solution turning into pink increasing the color intensity based on the amount of the dopant. The solution is stirred for 10 min and PEI is added, this changes the color of the solution to orange. The solution is stirred for 10 more minutes and transferred to glass bottle. The seeded substrates were placed at an angle of 60° in a 100-mL glass bottle with the seeds facing the bottom of the bottle. The temperature of the oven was maintained at 90°C for 24-h. Finally the substrates were removed from the growth solution rinsed with ethanol, and dried with nitrogen.

Surface/Structure Characterization. The morphology of Cobalt doped ZnO nanorods and TiO_2 nanoparticles was investigated by scanning electron microscopy (FEI Quanta FEG250 SEM in High vacuum mode). The elemental analysis of the cobalt and zinc is done using the EDX attached to the SEM. The ZnO nanorods and TiO_2 nanoparticles were additionally characterized by X-ray powder diffraction (XRD) using a Bruker D8 Advance X-ray diffractometer using Cu K_radiation (λ = 0.154178 nm) at a scanning rate of 0.04˚ s^{-1} in the 2θ range from 10˚ to 90˚.

Transient Measurements. Measurements of electron transport time were made using a set of National Instruments components in a PXIe chassis capable of high-resolution analog voltage output and digitized input. A square-wave modulation was applied to a white-light LED that was used to illuminate a DSSC. The modulation amplitude produced a <10% change in DSSC current, which is linear with light intensity. The DSSC was operated in series with a 65-Ω resistor and the voltage across this resistor was measured. The current is determined by I = V/R. We refer to this as a "quasi-short-circuit" mode, as the small voltages measured (<20 mV) were close to the shortcircuit condition, compared to open circuit voltages of hundreds of millivolts. At least 50 transients were averaged for noise reduction.

Photo electrochemical Characterization. Illuminated Open circuit potential to find the flat band potential over a 150 sec period(30 dark , 60 light, 60 dark).Illuminated electrode surface with UV-light at 300nm in 3 electrode cell setup with Ag/AgCl reference electrode and Pt wire counter electrode. The electrolyte was 0.1M $LiclO_4$ in H_2O pH=11 maintained with NaOH buffer, this electrolyte was chosen because of its inertness. To avoid reaction of photogenerated electrons with oxygen in the electrolyte, which would decrease the photovoltage, the solution is

purged with nitrogen gas. The position of the CB is approximated by the flat band potential, E_{fb}, which is a good approximation of the Fermi level, $E_{F.}$ All solutions were purged with nitrogen for at least 20 min before experiments. Samples were kept in air and illuminated from the front side.

Optical Characterization

The UV-Vis spectrum of doped and undoped TiO_2 and ZnO is obtained by using Cary 50 UV-Vis spectrophotometer. The diffuse reflectance spectrum is obtained using Shimadzu 2450 UV-Vis spectrophotometer with ISR-240A Integrating Sphere Attachment with barium sulphate as the standard. The optical absorption was measured in the 200–800 nm range.

Sensitization. After sintering, films were allowed to cool to 100°C then immediately immersed in 0.3 mM N719 in ethanol. After 12 hours they were removed and rinsed in acetonitrile and dried in air.

Solar Cell Assembly. Each sensitized electrode was sealed against a counter electrode on hot plate at 120°C using a hot-melt plastic frame (Solaronix, Meltonix 1170, 25 µm thick) applying light pressure with a glass rod. The assembled cell was filled with electrolytes through two holes in the counter electrode. The holes were then sealed using hot-melt plastic and a thin glass cover slide. The exposed conducting glass leads of each electrode were coated with copper tape (3M) for improved electrical conductivity.

Electrolyte Composition. Iodide/triiodide (I^-/I_3^-) electrolyte was prepared with 0.5 M tetrabutylammonium iodide and 0.05 M iodine (I_2) in 3-methoxypropionitrile. The ferrocene/ferrocenium (Fc/Fc^+) electrolyte contained 0.1 M ferrocene and 0.05 M ferrocenium hexafluorophosphate (Aldrich) in 3-methoxypropionitrile.

The Fc/Fc^+ electrolyte was deoxygenated by bubbling, nitrogen 10 minutes prior to cell fabrication to minimize reaction of ferreocene with oxygen.[13, 14]

Solar Cell Characterization. Current –Voltage **(** J- V) measurements were made using Keithley 2400 source/meter controlled by a PC, while irradiating at 1000 W/m^2 with AM 1.5G simulated sunlight produced by a solar simulator (Newport 91160). The DSSCs photo current and photo voltage were measured with an active area of 1 cm^2.

6.3 Results and Discussion

6.3.1 Synthesis of Cobalt doped ZnO nanorods.

Cobalt doped ZnO nanorods were fabricated on FTO. A typical example is shown in Figure 6. 2, having nanorod dimensions of about 5 μm length and 600 nm diameter, and a number density of 1.2×10^8 rods per cm^2 of FTO after 24 h deposition.

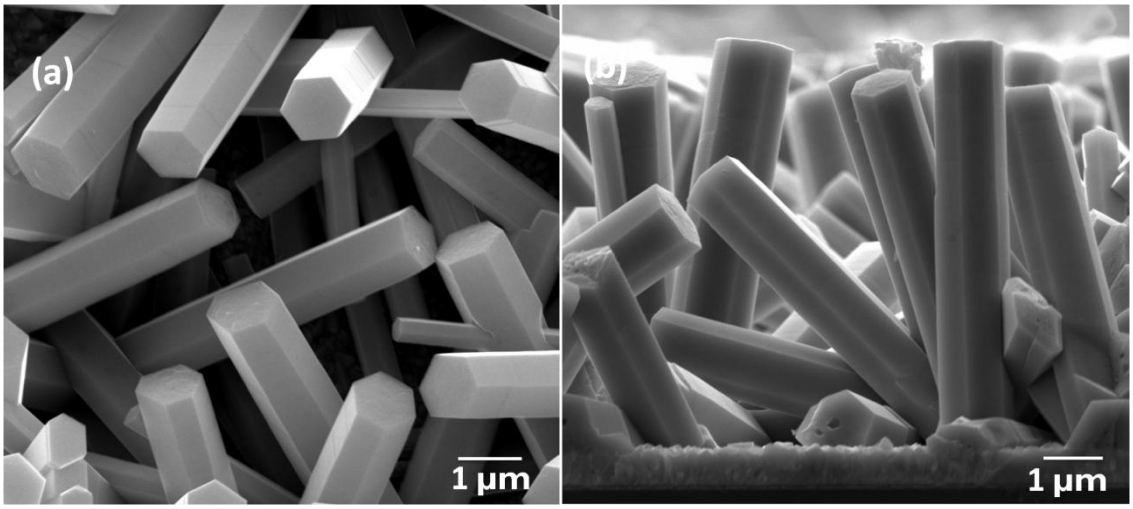

Figure 6. 2 10% Co doped ZnO nanorods SEM images (a) top view (b) cross section.

From the SEM images Fig 6.2 from surface morphology we can see that there is no phase separation and a solid solution of ($Zn_{0.9}Co_{0.1}$) O is formed. Dopant elements affect the growth kinetics of nanorods as they can introduce a thermodynamic barrier to crystal growth. The presence of Co^{2+} in solution changed the growth kinetics in the two principal directions (a- and c-axes).The average diameter and length of the $Zn_{1-0.1}Co_{0.1}O$ increased and average density of the nanorods decreased when compared to undoped ZnO nanorods. The average diameter of the nanorods increased from 600 nm to 1100 nm, while the average length increased from 5 µm to 6 µm.

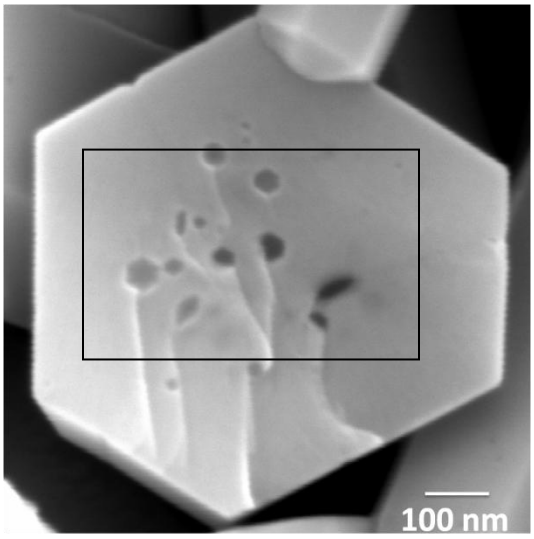

Figure 6. 3 10% Co doped ZnO nanorods SEM images (cut to half for EDX Analysis).

The EDS pattern is consistent with the XRD pattern showing the presence of the Co^{2+} in the ZnO matrix. The composition analysis shows the presence of Co, Zn, O and C. The presence of the carbon is due to conductive adhesives of the copper tape used for sticking the sample on the stage. EDX pattern indicates that Co is present in the ZnO matrix and the estimated concentration of Co in the ZnO is 3 at. % which is consistent with the 5 at. % initial precursor

concentration. From Figure 6. 4 (b) the EDX analysis indicates 9.9 at. wt % of ZnO is present for 10 mol % doping of zirconium added during the TiO_2 synthesis.

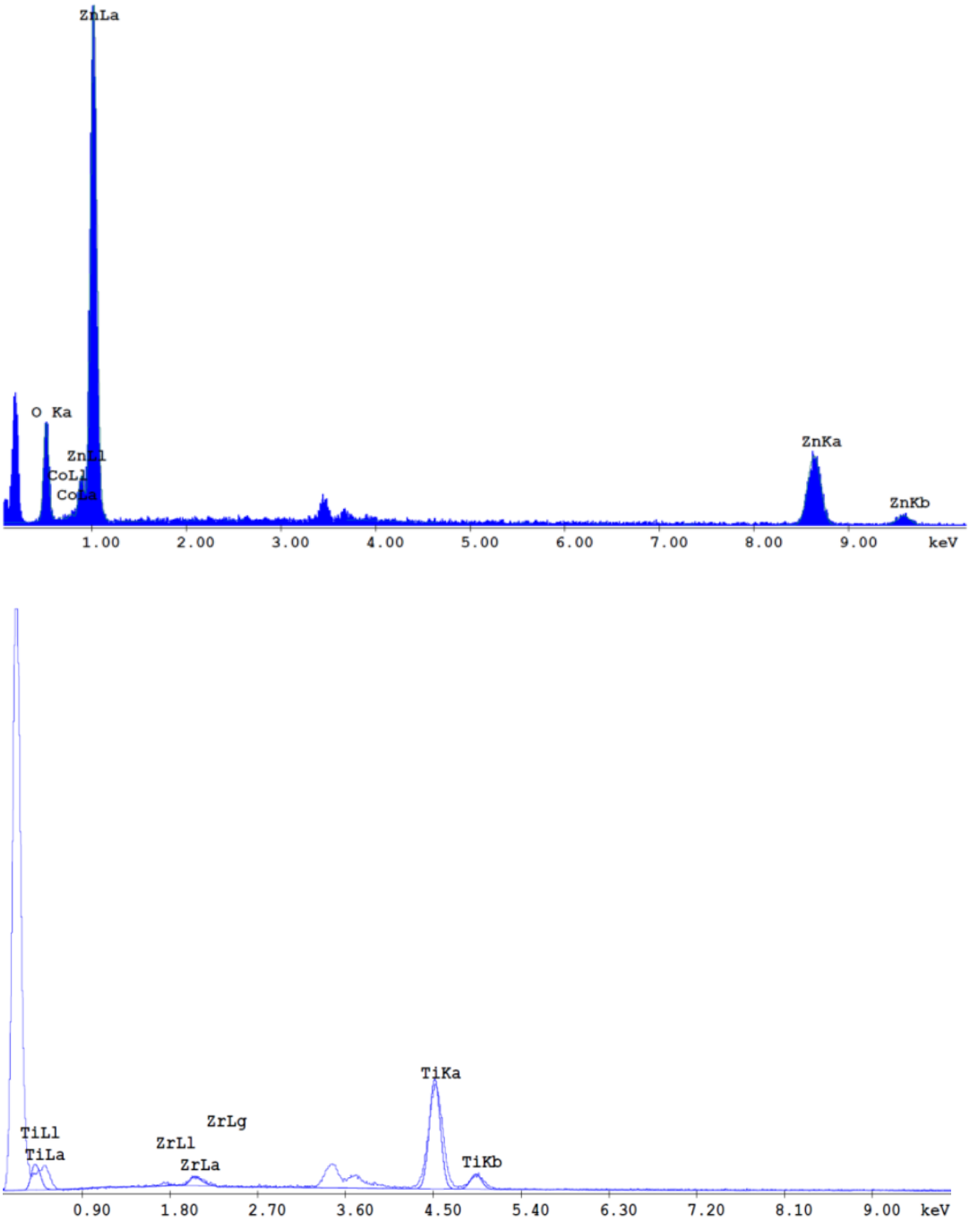

Figure 6. 4 EDX pattern of (a) 10% Cobalt doped ZnO nanorods (b) 10% Zr doped TiO_2 on fluorine doped tin oxide (FTO) substrate.

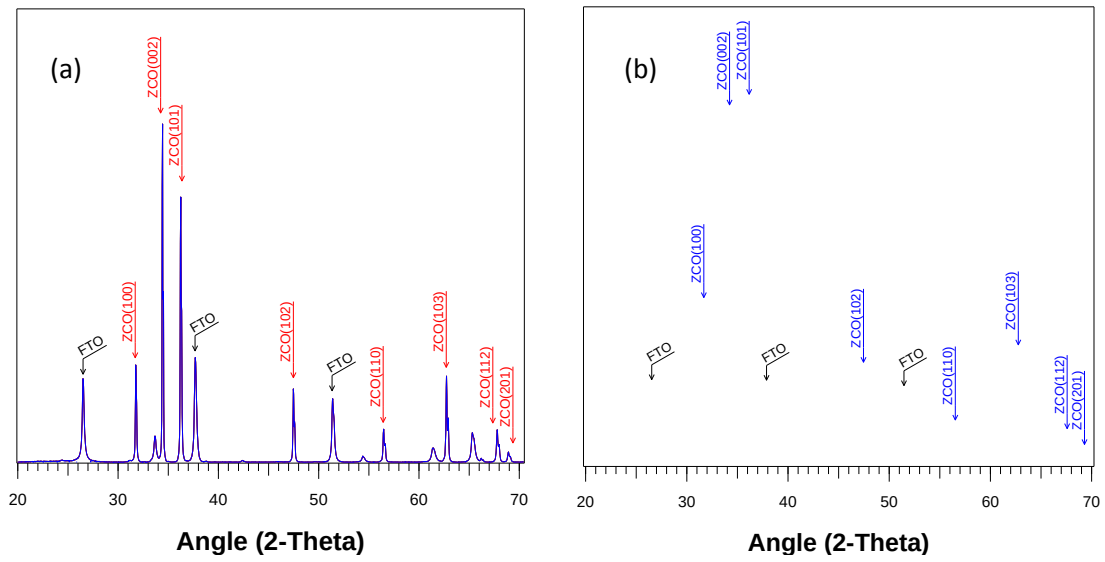

Figure 6. 5 X-ray diffraction pattern of Cobalt doped ZnO nanorods on fluorine doped tin oxide (FTO) substrate (a) 10% and (b) 5%.

The XRD θ–2θ scan data show that, for well-aligned nanorods on FTO intensity of the peak assigned to the (002) plane of ZnO was clearly revealing that Cobalt doped ZnO nanorods were formed through elongation along the *c*-axis perpendicularly to the substrate. Figure 6. 5 shows the XRD pattern of cobalt doped ZnO nanorods recorded in the range of 20-70° with a scanning step of 0.02°. All diffraction peaks can be attributed to crystalline ZnO with the hexagonal wurtzite structure (space group: P63*mc*(186); *a*) 0.3249 nm, *c*) 0.5206 nm). All the patterns have hexagonal wurtzite structure, without any additional impurity phases indicating that the wurtzite structure might have not affected due to the substitution of Cobalt. No excess peaks were detected indicating that all the starting organic precursors might have been completely decomposed. No peaks corresponding to the Cobalt oxide or cobalt precursor is detected indicating the incorporation of Co^{2+} in the ZnO matrix. The 2θ values of the (101) peak have been observed in the range of 36.15◦–36.27◦. The addition of Co does not alter the diffraction

angle and the full width at half maximum (FWHM) value of the any observed peak, suggests the incorporation of Co ions into the ZnO matrix. Sharp XRD peaks imply that there is a high degree of crystallization developed. The data are in agreement with the Joint Committee on Powder Diffraction Standards (JCPDS) card for Zinc cobalt oxide (JCPDS 072-8025). However, it should be noted that these are nominal compositions of cobalt, based on the atomic percentage of Co with respect to Zn in the initial reagents. Figure 6. 5 shows representative X-ray powder diffraction patterns of films deposited directly onto a glass sample-holder. The patterns showed no detectable peak shifts in 0%, 2% to 10% Co which indicates a substitution doping as expected.

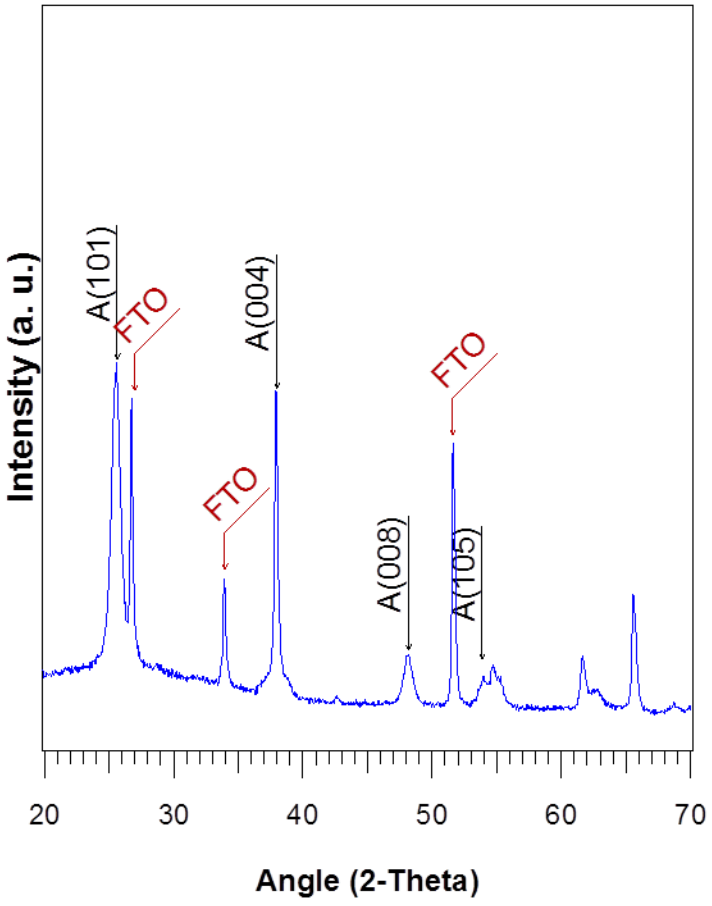

Figure 6. 6 XRD pattern of $Zr_{0.1}Ti_{0.9}O_2$

TiO_2 and $Zr_{0.1}Ti_{0.9}O_2$[15] was synthesized by using thermal hydrolysis. The ratios of the precursors are varied to change the doping percent of the zirconium in the TiO_2 at atomic scale. Figure 6. 7 show the porous $Zr_{0.1}Ti_{0.9}O_2$ synthesized by hydrolysis. From Figure 6. 4 b the ratio of Zr to Ti is determined by using energy dispersive X-ray analysis (EDX) was found to be 9.9% compatible with 10% molar doping. X-ray diffraction (XRD) measurements from Figure 6. 6 indicate the presence of the anatase phase without any mixed oxides. The increase in the size of the particle from 16 nm to 20 nm after zirconium doping was found by using Scherer equation from the XRD pattern. The increase in the Zr content not only accounted for increase in particle size but also band gap, characterized by flat band measurements shown in Figure 6. 8.

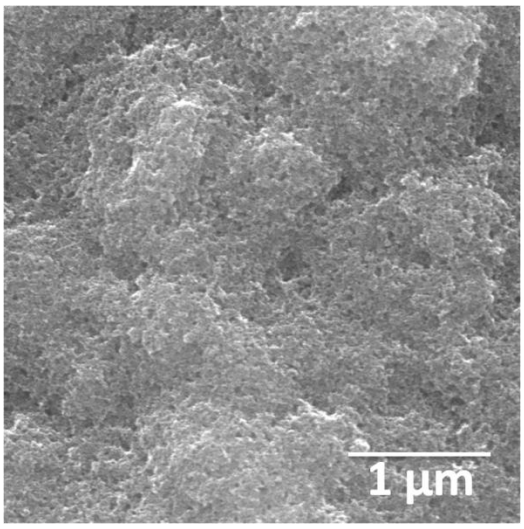

Figure 6. 7 SEM image of $Zr_{0.1}Ti_{0.9}O_2$

We propose that the morphological and structural change induced by Co-doping play a pivotal role in the electron transport. As discussed previously, the morphology and structure of ZnO nanorods vary as a function of the Co content and the ZnO nanorod arrays of samples doped exhibit the largest diameter. The appropriate increase in the nanorod diameter is considered

favorable due to a reduction in electron transport resistance, which further speeds up electron transport in the ZnO nanorod arrays.

6.3.2 E_{fb} Measurements.

We measured E_{fb} using the photocurrent onset potential for films. The bands are not flat and they bend updwards or downward depending on the experimental conditions. Figure 6. 8 shows measurements of E_{fb} in aqueous solution.

Figure 6. 8 shows the photovoltage of Co doped ZnO and undoped ZnO in 0.1M $LiclO_4$ in H_2O pH=11 maintained with NaOH buffer with the light from a 200 W Hg lamp being illuminated.

The E_{fb} of Co doped ZnO is consistently more positive than that of ZnO by ca. 0.15 V. Figure 6. 8 is constructed by combining the information of E_{fb} and E_g for both materials and includes the traps that account for our optical and photoelectrochemical measurements of E_g and E_{fb}. This diagram was drawn assuming Efb=Ecb, although Efb is a good approximation of EF. The difference between Ecb and Efb is set by the free carrier density, Nsc. Under open-circuit conditions, the photogenerated holes can accumulate at the surface, which with increasing light intensity lowers the barrier, for electrons until the electrons can reach the surface at the same rate as holes. At the same time, the quasi-Fermi level (measured as EOC) rises because of the higher occupancy of the conduction band. Accordingly, at sufficiently high-intensity, EOC becomes constant and this value is very close to the potential of the conduction band edge. In order to avoid reaction of photogenerated electrons with oxygen in the electrolyte, which would decrease the photovoltage we purged the electrolyte with nitrogen gas.

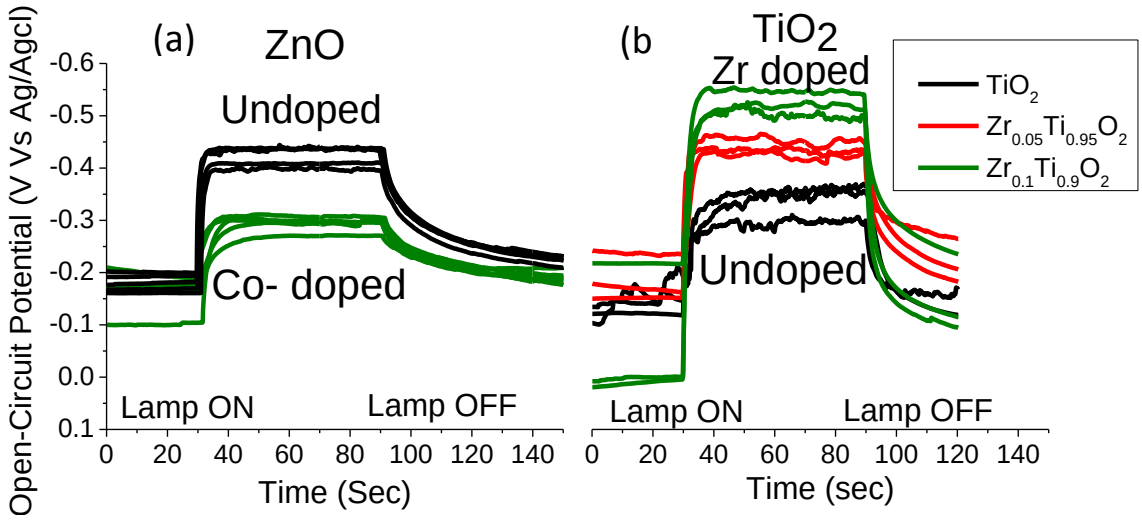

Figure 6. 8 Illuminated open circuit photovoltage of (a) Co0.1Zn0.9O nanorods and undoped ZnO nanorods (b) $Zr_{0.1}Ti_{0.9}O_2$, $Zr_{0.05}Ti_{0.95}O_2$, TiO_2 on fluorine doped tin oxide (FTO) substrate.

6.3.3 Photoluminescence.

The photoluminescence(PL) spectra of the films at room temperature are presented in Figure 6.9 . The spectrum of the nanorods is characterized by an intense UV emission (386 nm) due to exciton recombination. No visible emission due to the radiative recombination at material defects is found and the layer is of high structural quality.

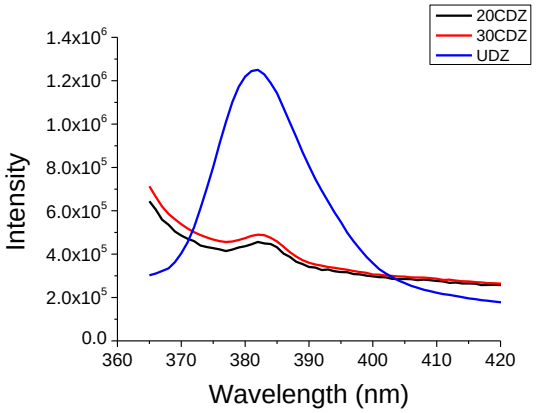

Figure 6.9 PL measurement of cobalt doped ZnO nanorods(20CDZ- 20%Co doped ZnO nanorods, 30CDZ-30% Co doped ZnO nanorods and UDZ-undoped ZnO nanorods).

6.3.4 Diffuse Reflectance.

The Kubelka-Munk model is used for the analysis of the band gap of the doped and undoped TiO_2 and ZnO. Kubelka –Munk[16] model is given by eguation: $F(R) = (1-R)^2 / 2R$

$$F(R) = (1-R)^2 / 2R$$

where R is the reflectance and F(R) is proportional to excitation coefficient(α)

Modified Kubelka–Munk function can be obtained by multiplying the F(R) function by hv, using the corresponding coefficient (n) associated with an electronic transition as follows

$$(F(R) \times \mathrm{h}\nu)^n$$

By ploting the above function as a function of eV, the band gap of the semiconductor is obtained. This technique is used due to high light scattering materials and absorbing nature of the nanorods. From we can see the blue shift of the doped TiO_2, clearly indicating an incarese in the band gap. The clear difference in the band gap of the 5% Zr doping and 10% Zr doping is obtained. In the case of 10% Co doped ZnO no change in the band gap is observed.

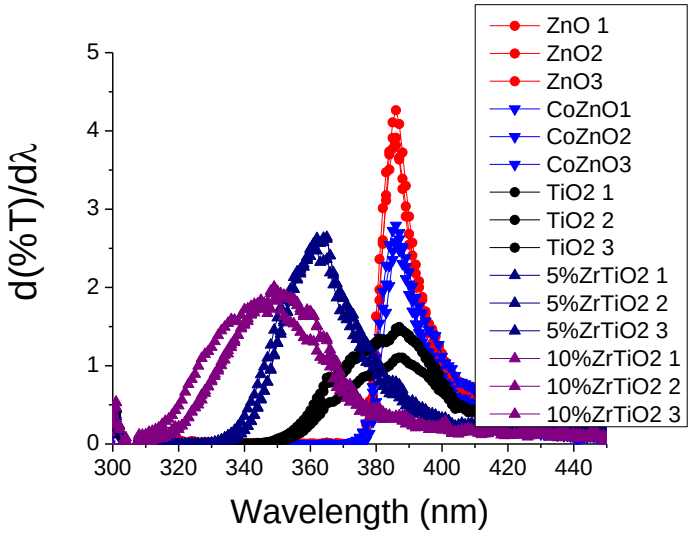

Figure 6. 10 Band gap of the doped and undoped ZnO and TiO_2.

6.3.5 Device Performance.

The benefit of the hybrid structure is revealed when using ferrocene/ferrocenium as a model alternative redox couple with high recombination rates (Figure 6. 12). We focus here on the changes in the short circuit current (J_{SC}), as these report on the electron collection efficiency. We note that faster electron transport can improve J_{SC} due to higher electron collection efficiency, but it cannot improve the open-circuit voltage (V_{OC}) since no electron transport occurs at open circuit.

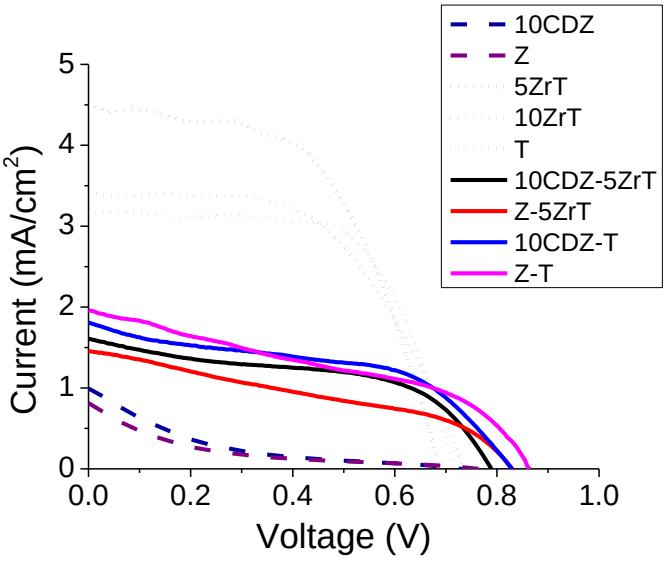

Figure 6. 11 Current-voltage (J–V) characteristics for solar cells using electrolyte based on I^-/I_3^-, under illumination with 100 mW/cm2 AM1.5G simulated sunlight.

The short circuit photocurrent density (Jsc) of the 10% Co-doped cells is slightly higher than that of the pure ZnO nanorod cell; but that of the CS structure is six times than the pure ZnO nanorods. . We confirmed that this reduction of photocurrent did not result from a difference in the amount of adsorbed dye. The reduction of the photocurrent for 10% Co doped ZnO nanorods than CS nanostructures would result from excess scattering centers introduced into the lattice due

to the high amount of dopant ions. This suggests that the electron transport is much slower in ZnO with high doping levels of cobalt without the shell.

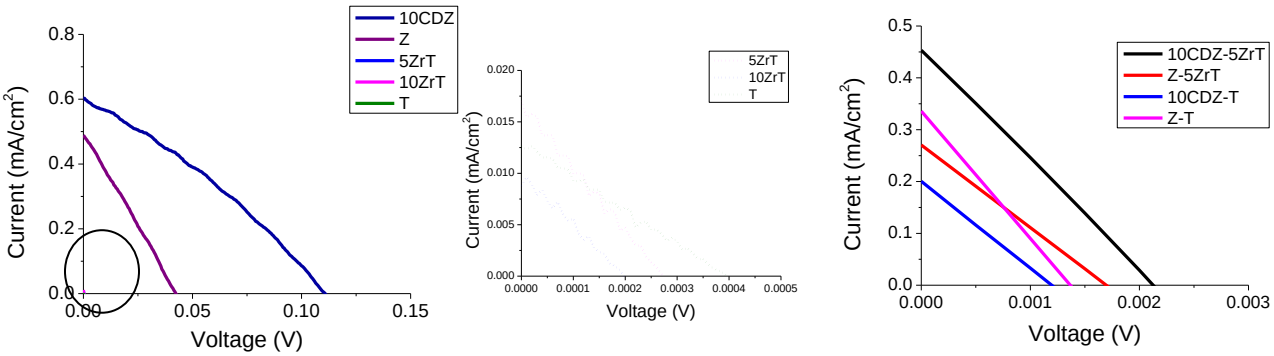

Figure 6. 12 Current-voltage (J–V) characteristics for solar cells using electrolyte based on Fc/Fc^{+}, under illumination with 100 mW/cm2 AM1.5G simulated sunlight.

After 5% Zr doping we have seen an increase in the photocurrent 3.4mA/cm^2 to 4.5 mA/cm^2, but for 10% Zr doping we have seen decrease in the current to 3.2 mA/cm^2 may be due to non alignment of the dye LUMO and the conduction band edge of the 10% Zr doped TiO_2 because of the upward shift of the conduction band preventing electron injection resulting in decrease of photocurrent.

6.3.6 Transport Measurements.

Figure 6. 13 b shows representative current transients at quasi-short circuit conditions for Z, CDZ and CS films. Each transient is well fit by a single exponential decay of the form $y = y_0 + Aexp(-t/\tau_{tr})$, where τ_{tr} is the characteristic time for electron transport. The fitted time constants τtr over a range of light intensities are plotted against the corresponding shortcircuit

current J_{SC} in Figure 6. 13b. For TiO_2, the power-law decrease of τ_{tr} with increasing *J*SC is typical of DSSCs and is well described by a trapping–detrapping model. Time constants for the other samples are relatively constant at about 0.29 ms for ZnO nanorods and 0.46 ms for ZT nanorods coated with TiO2 nanoparticles. The invariability of τ_{tr} with J_{SC} for the Z and 10CDZ nanorod samples strongly suggests that a limit of the measurement has been reached, most likely due to an *RC* time based on the resistance of the cell and resistor connected in series and the capacitance of the semiconductor/electrolyte interface. These time constants should therefore be taken as an upper limit on the electron transport time of the ZnO nanorod-based materials. Since the *RC* time may differ for different samples, the results shown in Figure 6. 13 cannot differentiate between the τtr value of Z, CDZ and core-shell films, but they do demonstrate that electron transport in these samples is close to two orders of magnitude faster than transport through nanoparticulate TiO_2.

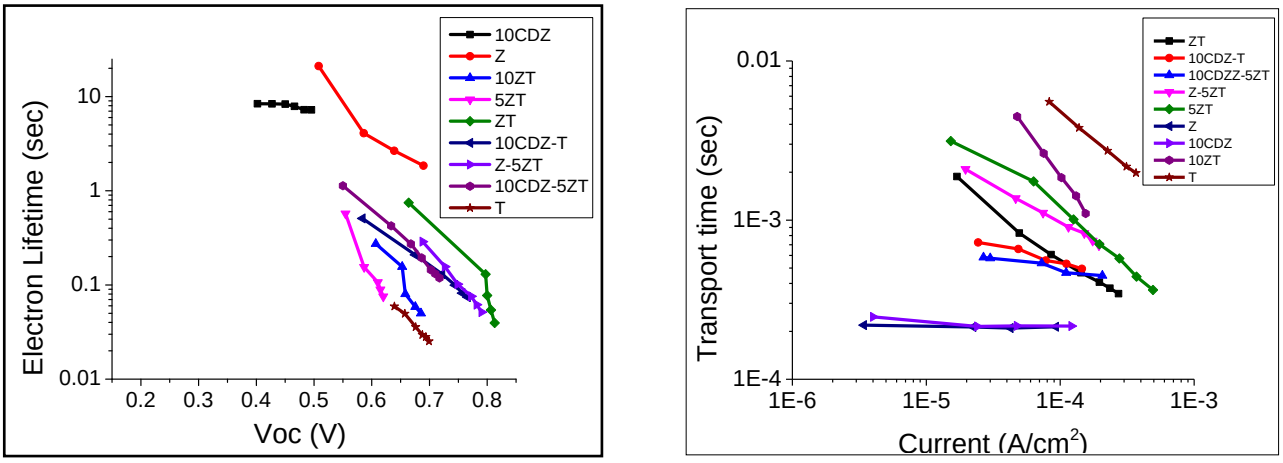

Figure 6. 13 (a) Fitted electron lifetime versus open circuit photovoltage (b) Fitted electron transport time constants versus quasi-short-circuit current for hybrid films and undoped films.

Dark current.

Dark current in DSSCs cannot be related directly to the recombination current since the electrolyte concentration in the porous film and the potential distribution across the nanoporous electrode in dark are different than those under illumination. However a comparison between two similar cells can provide information regarding the relative recombination rates.

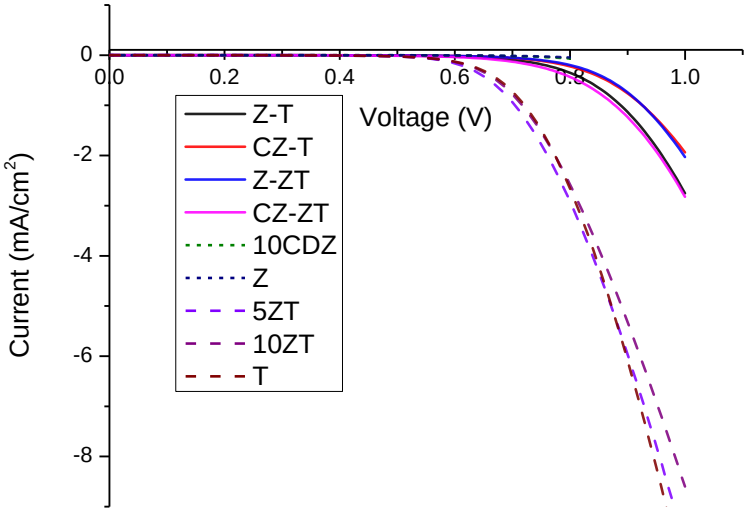

Figure 6. 14 Dark current measurements of the solar cells using I /I3- electrolyte (dash line for nanoparticulate films, solid lines for core-shell nanostructures, short dash for nanorods).

The dark current measuresurements in Figure 6. 14 indicate lower electron recombination in the core-shell films when compared to nanoparticulate films due to fast electron transport. There is negligible change in the dark current for the nanorods and core-shell nanostructures.

Better electron transport within the nanowire photoanode is a product of both its higher crystallinity and an internal electric field that can assist carrier collection by separating injected electrons from the surrounding electrolyte and sweeping them towards the collecting electrode. The Debye–Hückel screening length of ZnO (roughly one-third of the thickness of the space-

charge layer in the semiconductor at the semiconductor–electrolyte junction) is about 4 nm for a carrier concentration of 10^{18} cm-3, making our nanowires thick enough to support the sort of radial electric field (depletion layer) that is impossible in smaller TiO_2 or ZnO nanoparticles with fewer carriers. This upward band bending at the nanowire surface should suppress recombination by corralling injected electrons within the wire cores. At the same time, an axial field along each nanowire encourages carrier motion towards the external circuit. These macroscopic fields should act synergistically to increase electron transport relative to nanoparticle cells, which lack such fields. Ambipolar diffusion is consequently a less dominant mechanism in the nanowire devices[5].

These core-shell nanostructures prevent the contact of the electrolyte and the electron transporting core-material. The contact between the dye-sensitized ZnO and the electron transfer material becomes better at the inner side. This structure should be helpful in improving the charge separation efficiency of the electrode and the electrolyte, suppressing the dark current and the efficiency of carrier collection[17]. Nanowire structures allow for the presence of an interfacial electric field that is otherwise absent in nanoparticle-based dye sensitized solar cells (DSSCs). This electric field enhances charge transport by inducing potential gradient migration. This mechanism does not occur in nanoparticle-based devices, which are limited to charge transport by only diffusion. Furthermore, the use of conductive core/semiconductive shell nanowire structures decouples the length a photogenerated charge must travel to be collected from the photoanode thickness (thus overall photoactive surface area).

6.4 Conclusions

Conduction band edge of the ZnO and TiO_2 are engineered to remove the energy barrier and provide effective electron transport. The 5%Zr doping increased the photocurrent of DSSC due to faster electron transport, where as 10% Zr doping decreased the photocurrent probably due to unfavorable conduction band edge for electron injection. The core-shell with 10CDZ-5ZT has better efficiency in Fc/Fc^+ due to fast electron transport and favorable electron injection of the 5% Zr doped TiO_2. The recombination is much lower for core-shell nanostructures when compared to nanoparticulate TiO_2 films. These band edge engineered nanostructures might be promising for application in cobalt complex electrolyte and ionic liquids based electrolytes where diffusion is limited due to bulky ions.

6.5 References

1. B. O'Regan and M. Gratzel, "A low-cost, high-efficiency solar cell based on dye-sensitized colloidal TiO_2 films," *Nature*, 353[6346] 737-40 (1991).
2. O. Varghese, M. Paulose, T. LaTempa, and C. Grimes, "High-Rate Solar Photocatalytic Conversion of CO_2 and Water Vapor to Hydrocarbon Fuels," *Nano Lett*, 9 31 (2009).
3. K. Tennakone, G. R. R. A. Kumara, I. R. M. Kottegoda, and V. P. S. Perera, "An efficient dye-sensitized photoelectrochemical solar cell made from oxides of tin and zinc," *Chemical Communications*[1] 15-16 (1999).
4. K. Keis, J. Lindgren, S.-E. Lindquist, and A. Hagfeldt, "Studies of the Adsorption Process of Ru Complexes in Nanoporous ZnO Electrodes," *Langmuir*, 16[10] 4688-94 (2000).
5. M. Law, L. E. Greene, J. C. Johnson, R. Saykally, and P. Yang, "Nanowire dye-sensitized solar cells," *Nat Mater*, 4[6] 455-59 (2005).

6. M. Quintana, T. Edvinsson, A. Hagfeldt, and G. Boschloo, "Comparison of Dye-Sensitized ZnO and TiO_2 Solar Cells: Studies of Charge Transport and Carrier Lifetime," *The Journal of Physical Chemistry C,* 111[2] 1035-41 (2006).

7. K. Keis, C. Bauer, G. Boschloo, A. Hagfeldt, K. Westermark, H. Rensmo, and H. Siegbahn, "Nanostructured ZnO electrodes for dye-sensitized solar cell applications," *Journal of Photochemistry and Photobiology A: Chemistry,* 148[1-3] 57-64 (2002).

8. M. Law, L. E. Greene, A. Radenovic, T. Kuykendall, J. Liphardt, and P. Yang, "ZnO−Al2O3 and ZnO−TiO_2 Core−Shell Nanowire Dye-Sensitized Solar Cells," *The Journal of Physical Chemistry B,* 110[45] 22652-63 (2006).

9. R. Zhao, L. Zhu, F. Cai, Z. Yang, X. Gu, J. Huang, and L. Cao, "ZnO/TiO_2 core–shell nanowire arrays for enhanced dye-sensitized solar cell efficiency," *Appl. Phys. A* 1-7 (2013).

10. Y. Feng, X. Ji, J. Duan, J. Zhu, J. Jiang, H. Ding, G. Meng, R. Ding, J. Liu, A. Hu, and X. Huang, "Synthesis of ZnO@TiO_2 core–shell long nanowire arrays and their application on dye-sensitized solar cells," *Journal of Solid State Chemistry,* 190[0] 303-08 (2012).

11. V. Manthina, J. P. Correa Baena, G. Liu, and A. G. Agrios, "ZnO–TiO_2 Nanocomposite Films for High Light Harvesting Efficiency and Fast Electron Transport in Dye-Sensitized Solar Cells," *The Journal of Physical Chemistry C,* 116[45] 23864-70 (2012).

12. L. Vayssieres, "Growth of Arrayed Nanorods and Nanowires of ZnO from Aqueous Solutions," *Advanced Materials,* 15[5] 464-66 (2003).

13. T. W. Hamann, O. K. Farha, and J. T. Hupp, "Outer-Sphere Redox Couples as Shuttles in Dye-Sensitized Solar Cells. Performance Enhancement Based on Photoelectrode Modification via Atomic Layer Deposition," *The Journal of Physical Chemistry C,* 112[49] 19756-64 (2008).

14. T. Daeneke, T.-H. Kwon, A. B. Holmes, N. W. Duffy, U. Bach, and L. Spiccia, "High-efficiency dye-sensitized solar cells with ferrocene-based electrolytes," *Nat Chem,* 3[3] 211-15 (2011).

15. M. Dürr, S. Rosselli, A. Yasuda, and G. Nelles, "Band-Gap Engineering of Metal Oxides for Dye-Sensitized Solar Cells," *The Journal of Physical Chemistry B,* 110[43] 21899-902 (2006).

16. M. F. Kubelka P *Ein Beitrag zur Optik der Farbanstriche Z. Tech. Phys.*, 12 (1931).

17. J. Yu, D. Wang, Y. Huang, X. Fan, X. Tang, C. Gao, J. Li, D. Zou, and K. Wu, "A cylindrical core-shell-like TiO_2 nanotube array anode for flexible fiber-type dye-sensitized solar cells," *Nanoscale Research Letters*, 6[1] 94 (2011).

Chapter 7
Blocking layer effect on Dye sensitized solar cells

7.1 Introduction

In DSSC charge recombination at semiconductor/electrolyte interface is a major loss path way, and particularly dominant at low light intensities.[1] The I^-/I_3^- electrolyte has slow recombination kinetics, but due to large over potential loss, complex chemistry and corrosive nature. The I^-/I_3^- replaced by other electrolytes like Fc/Fc^+, Co^{2+}/Co^{3+} and Mn^{3+}/Mn^{4+} due to less to less toxicity, single electron transfer and minimized overpotential loss, but have higher recombination rate.[2] Recently the best efficiencies reported are with cobalt a complex electrolyte due to lower overpotential, but have higher recombination rate.[3] Blocking layers are widely used in DSSC to prevent recombination of the electron in the semiconductor/FTO with the electrolyte. Blocking layers are often thin insulating layers of TiO_2[4], ZnO[5, 6], ZrO_2[7, 8], SiO_2[7], Al_2O_3[7, 9], MgO[10, 11], HfO_2[12], CdO[13], polysiloxane[14] deposited on working electrode by various techniques like spray pyrolysis[15], sputtering[16], spin coating, dip coating[17], chemical vapor deposition[18], sol-gel deposition[7], $TiCl_4$ treatment[4], chemical bath deposition[19] and atomic layer deposition[20].

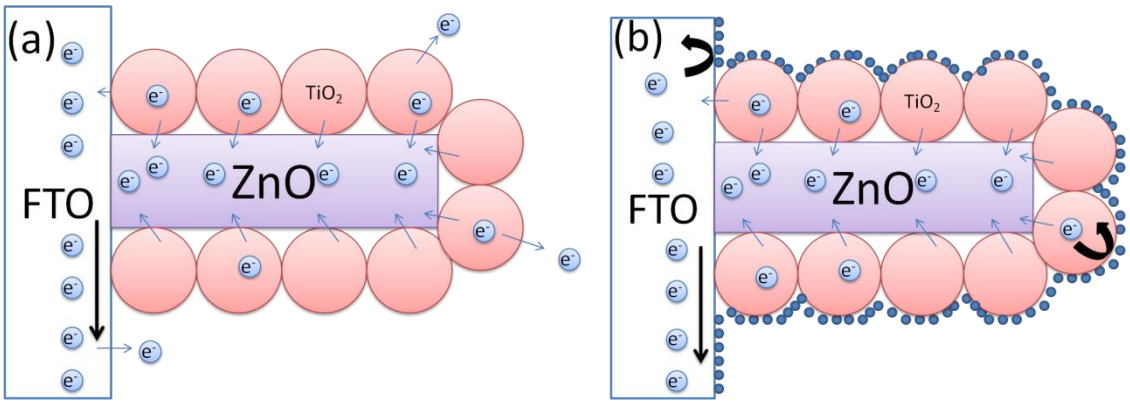

Figure 7. 1 Schematic of (a) ZnO-TiO_2 film and (b) ZnO-TiO_2 film with blocking layer.

The ideal blocking layer should cover the entire surface of the FTO and TiO_2 to prevent recombination and should not prevent electron injection. Chemical bath deposition barrier layers often increased the performance of the DSSC, but non uniform growth of barrier layers and lower thickness control in 1 nm precision is observed. This led to growth of atomic layer deposition as alternative to chemical bath deposition. ALD offers precision thickness control in angstrom range and uniform coating. The thickness of the barrier layer is important as it can prevent electron injection overshadow the effect of reducing recombination or improving voltage of cell due to conduction band raise.[21] In this report we used two simple techniques for the synthesis of the blocking layers on the ZnO-TiO_2 films. Atomic layer deposition and $TiCl_4$ was used due to low temperature and large area synthesis. We analyzed the effect of the thickness of the blocking layers on performance of DSSC in conventional I^-/I_3^- electrolyte and the fast recombining Fc/Fc^+ electrolyte. The results provide understanding of the role of blocking layer thickness and insight for optimizing DSSC and other electrochemical processes like water splitting.

7.2 Experimental

Reagents and Materials. All chemicals were purchased from Sigma-Aldrich (USA) and were ACS grade. N719 was purchased from Dyesol (Australia). SnO_2: F glass (FTO, transmission> 80% in the visible spectrum; sheet resistance 8 Ω /□) was purchased from Hartford Tec Glass (USA).

Electrode Fabrication. ZnO-TiO_2 (ZT) films are synthesized as reported previously.[22] $TiCl_4$ treatment is carried by immersing the ZT films in 40 mM $TiCl_4$ solution[4] at 4°C for 30 minutes and rinsed in deionized water and ethanol.[23] ALD of TiO_2 on the ZnO-TiO_2 films is carried on ALD instrument (Cambridge Nanotech savannah S100). The deposition is carried out using successive pulses of titanium ispopropoxide (75°C) and deionized water (25°C) and using nitrogen as the carrier gas inside the vaccum chamber with base pressure of 2 mtorr. The substrate is hold at 200°C temperature inside the ALD reactor. After the pulse of titanium ispopropoxide and water the precursors are confined in the reactor to 30 ms to ensure complete coverage of the TiO_2 inside the mesopores of the ZT films. The films are sintered on titanium hot plate at 500ºC.

Sensitization. After sintering at 500ºC, films were allowed to cool to 100°C then immediately immersed in 0.3 mM N719 in ethanol. After 12 hours they were removed and rinsed in acetonitrile and dried in air.

Solar Cell Assembly. Each sensitized electrode was sealed against a counter electrode on a hot plate at 120°C using a hot-melt plastic frame (Solaronix, Meltonix 1170, 25 μm thick), applying light pressure with a glass rod. The assembled cell was filled with electrolyte through two holes in the counter electrode. The holes were then sealed using hot-melt plastic and a thin glass cover

slide. The exposed conducting glass leads of each electrode were coated with copper tape (3M) for improved electrical conductivity.

Electrolyte Composition. The electrolyte composition is the same as used in the previous chapters.

Solar Cell Characterization. Current–voltage (*J*–*V*) measurements were made using Keithley 2400 source/meter controlled by a PC, while irradiating at 100 mW/cm2 (1 sun) with AM 1.5G simulated sunlight produced by a solar simulator (Newport 91160), calibrated against a silicon reference cell with KG5 filter (PV Measurements, Inc., Boulder, CO). The DSSC active area was 1 cm^2.

Characterization. The morphology of ZnO-TiO_2 films treated with $TiCl_4$ and ALD was investigated by scanning electron microscopy (FEI Quanta FEG250 SEM in High vacuum mode) attached with EDX and characterized by X-ray powder diffraction (XRD) using a Bruker D8 Advance X-ray diffractometer using Cu K_radiation (λ = 0.154178 nm) at a scanning rate of 0.04˚ s^{-1} in the 2θ range from 10˚ to 90˚.

7.3 Results and Discussion

7.3.1 ALD Deposition and $TiCl_4$ treatment

The thickness of the ALD deposited TiO_2 film is found to be 0.03nm/cycle at 200℃ synthesis temperature.[20] From the SEM images we observed the clogging of the pores with the increase in the number of cycles of ALD. The clogging of pores reduces the surface area leading to reduced dye loading and efficiency.

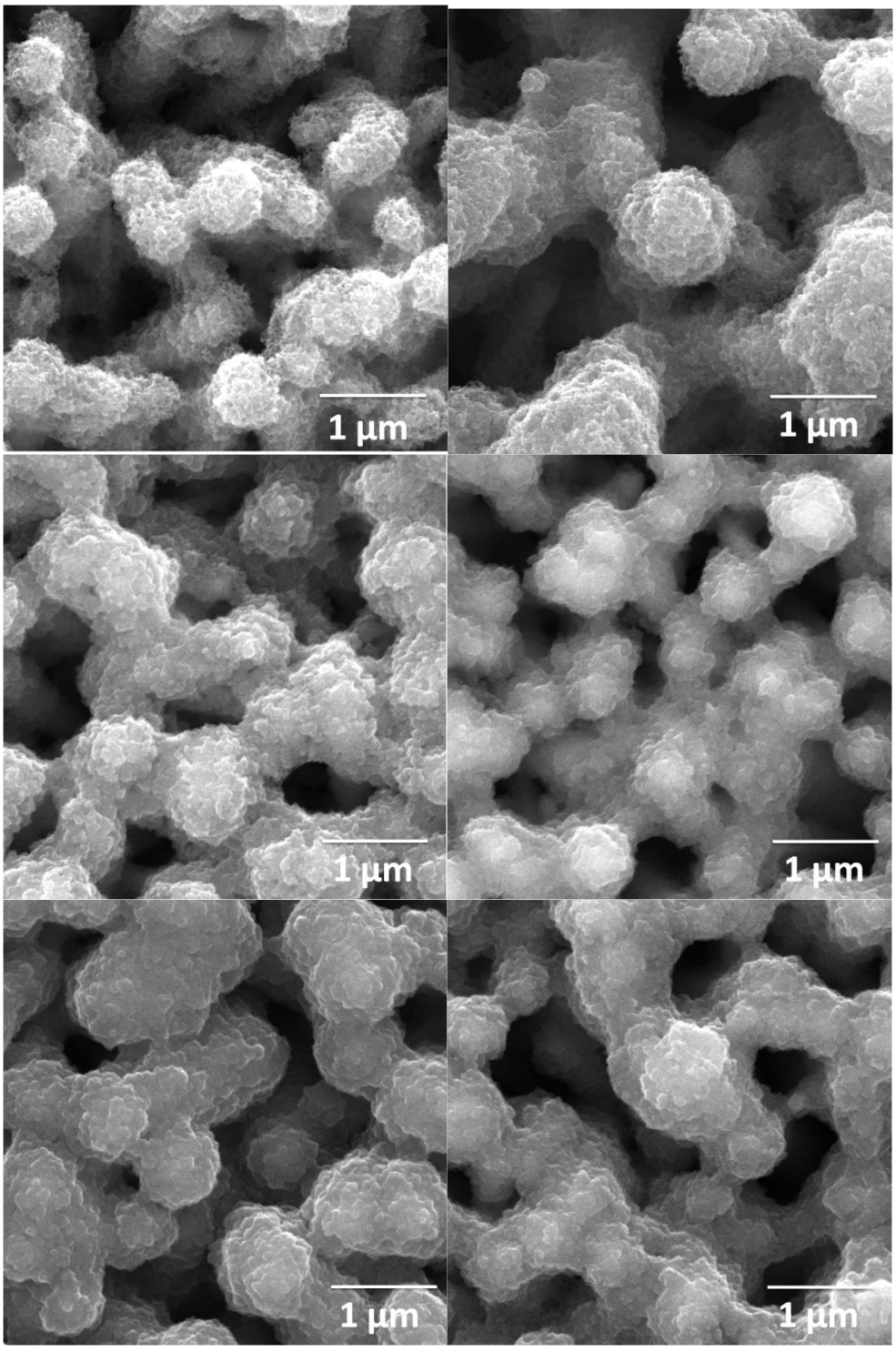

Figure 7. 2 ALD on ZnO-TiO_2(ZT) films (a) 40, (b) 100, (c) 200, (d) 300, (e) 400 and (f) 500

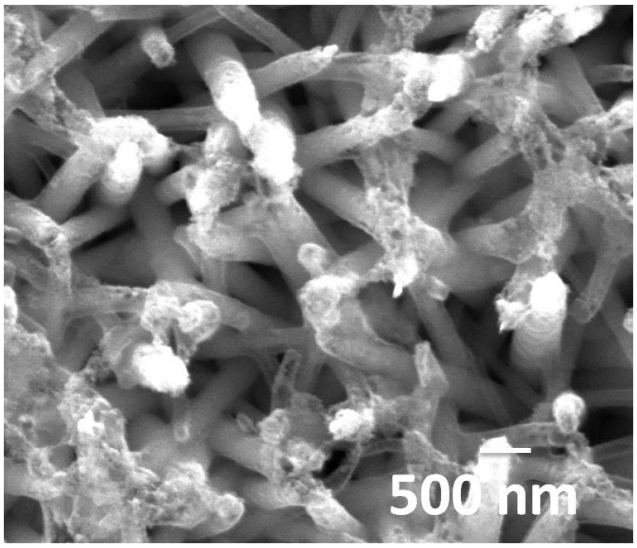

Figure 7. 3 SEM image of $TiCl_4$ treated ZT Film.

From the SEM image (see Figure 7. 3) we observed deposition of TiO_2 on the surface of the ZT films. From the EDX spectrum we see 2.24% of TiO_2 by weight on the ALD deposited film and 3.22% on the $TiCl_4$ treated ZT films.

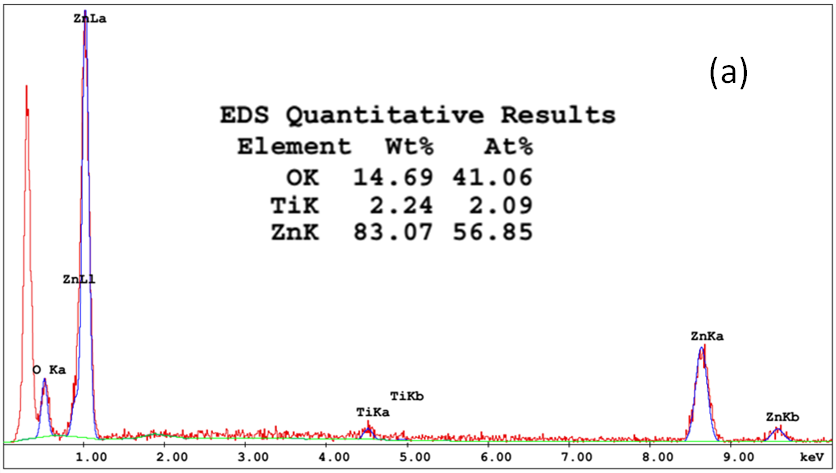

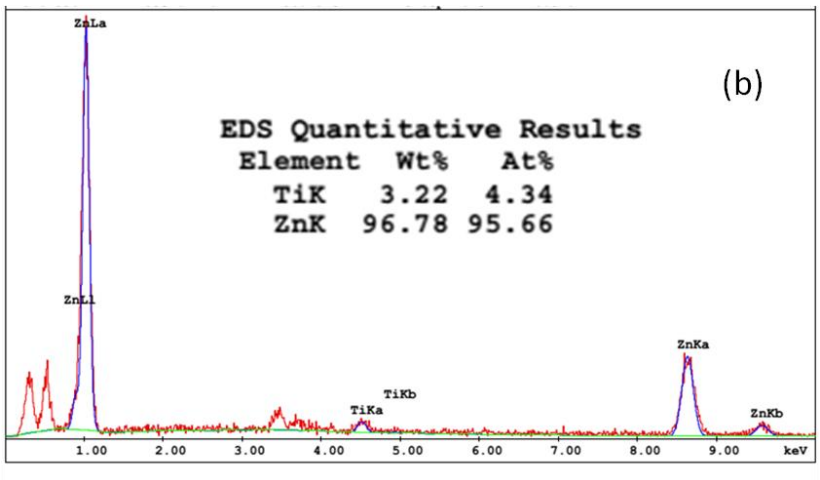

Figure 7. 4 EDX spectrum of (a) 100 layers of ALD (b) $TiCl_4$ treated ZT films.

7.3.2 Effect of number of ALD cycles.

Thin blocking layers performed better due to better transmittance of light and better tunneling effect. Thicker layers cannot have tunneling and prevent electron injection. From the Figure 7. 6 we observed decrease in the dye loading with the increase of the number of cycles and the trend reverses after 300 cycles. This phenomenon indicates complete blockage of the pores after 300 cycles, where it acts like a solid substrate. This can be explained by Figure 7. 5 where the maximum efficiency is observed at ALD TiO_2 300 cycles in fast recombining Fc/Fc^+ electrolyte. This phenomenon is observed as the recombination is directly proportional to the surface area. After 300 cycles of TiO_2 ALD we see an increase in the surface area therefore reducing the performance of the DSSC. In I^-/I_3^- electrolyte where recombination is slow we observed maximum efficiency at 100 cycles of ALD due to optimized blocking layer effect preventing recombination. When the TiO_2 film is too thick (100 to 500 cycles of ALD) we observed a decrease in the DSSC performance due to reduction in electron mobility.

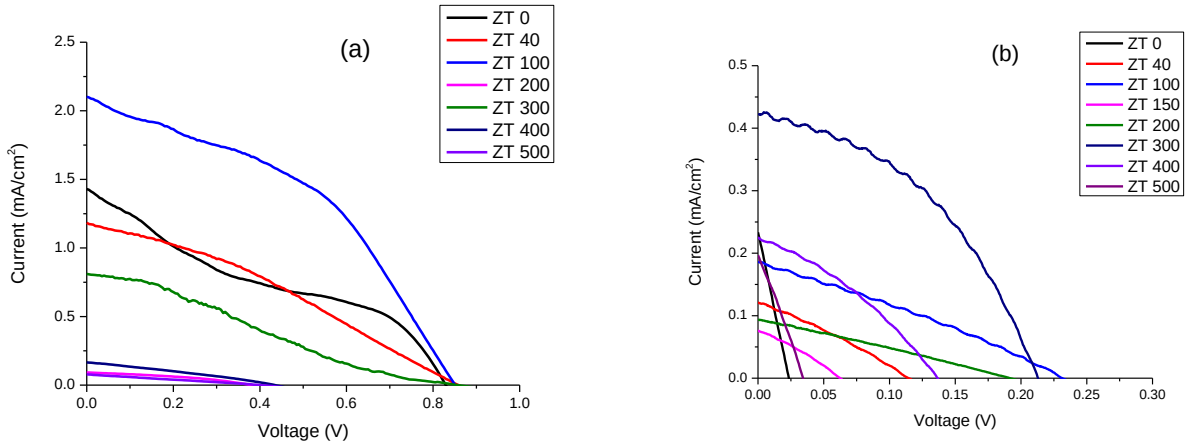

Figure 7. 5 Current-voltage (J–V) characteristics for solar cells using ZT films with 0-500 cycles of ALD (a) I-/I3- and (b) Fc/Fc+ under illumination with 100 mW/cm2 AM1.5G simulated sunlight.

The decrease in the current may be due to poor electron injection from the dye to the conduction band of TiO_2 nanoparticle. The poor electron injection is due to higher conduction band of the ALD deposited TiO_2 nanoparticles due to quantum confinement.[24] The band gap of the TiO_2 increases with the decrease of the particle size. After the ALD deposition the particle size of the TiO_2 is 0.03 nm. As in our case the particles size is less than 1 nm the band gap of the TiO_2 nanoparticles is more than 5 eV[24], resulting in poor electron injection. At low ALD cycles upto 100 cycles (3 nm) the phenomena of tunneling occur, resulting in electron injection. The tunneling process occurs on the TiO_2 surface even though it has large band gap due to strong electric field between the dyes excited state and the conduction band of the semiconductor.[25]

7.3.3 Dye loading

From Figure 7. 6 we see an increase in the dye loading by 7 % after $TiCl_4$ treatment when compared to untreated ZT films. We observed the current increased by a factor of 2 after $TiCl_4$ treatment indicating dye loading is not responsible for the increase in the current.

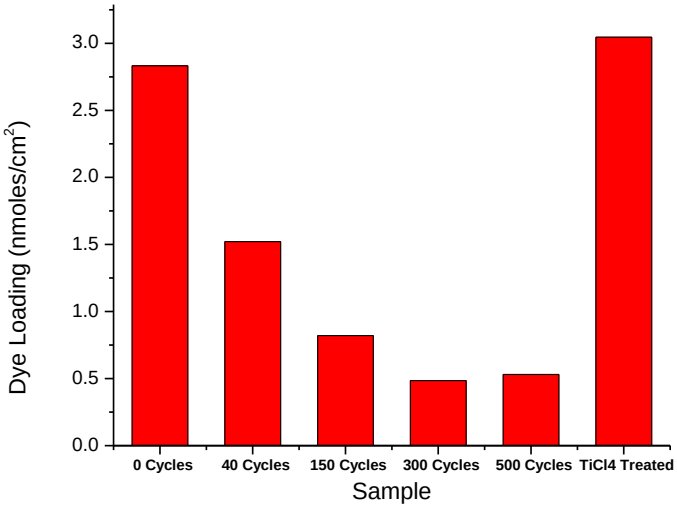

Figure 7. 6 Uptake of N719 by a ZnO nanorod array coated with three layers of TiO_2 with 0-500 cycles of ALD and $TiCl_4$ treatment.

In Figure 7. 7 we compared the performance of the $TiCl_4$ treated film and the best TiO_2 ALD (100 cycles) films. Interesting the $TiCl_4$ treated film has better performance with an increase the current from 2 mA/cm^2 to 4.4 mA/cm^2 with 90 mV decrease in the voltage. The increase in V_{OC} over 0.8V might be due to reduced recombination, smaller dark current shown in

Figure 7. 8. The increase in the efficiency of the $TiCl_4$ treated ZT film is due to reduction of the defects on the surface of the TiO_2 nanoparticles.[26] Various defects can take place on the surface of the TiO_2 nanoparticles due to the presence of the oxygen vacancies, bridge bonded oxygen, hydroxyl groups and fivefold coordinated Ti atoms.[27, 28] $TiCl_4$ treatment reducing the surface defects is observed using photoluminescence by Knorr et al and Seo et al.[29, 30] The reduction in the defects after $TiCl_4$ treatment is due to growth of TiO_2 at the surface states like oxygen vacancies and dangling bonds.[31] The band gap of the TiO_2 is does not change after the $TiCl_4$ treatment was reported by Zhang et al, thus does not prevent electron injection.[32] From Figure 7. 7 we observed the higher voltage in ALD deposition as it prevents electron recombination with

the electrolyte, moving fermi level in negative direction. The reduction in the voltage after $TiCl_4$ treatment is due to recombination of electrons with the electrolyte as observed in Figure 7. 7.

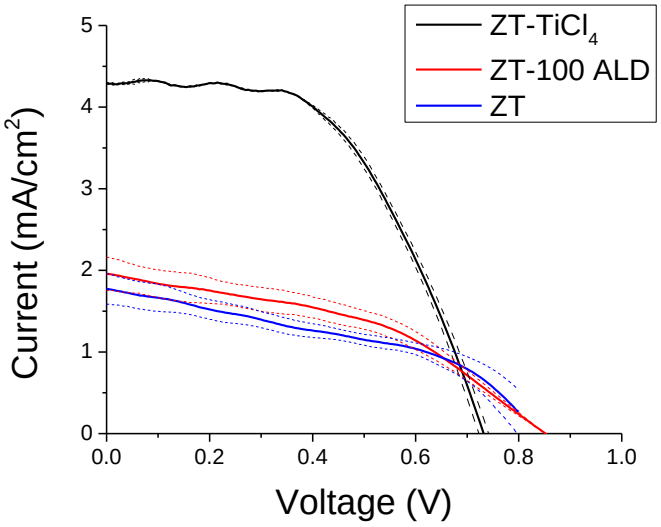

Figure 7. 7 I-V Measurements of $TiCl_4$ treated, ALD coated ZT films and pure ZT nanocomposites.

The results show that $TiCl_4$ treatment passivates the surface defects and reduces the recombination resulting better fill factor and photocurrent improving the performance of the DSSC. The dark currents in

Figure 7. 8 Darkcurrent measurements of $TiCl_4$ treated and ALD coated ZT films. show that TiO_2 ALD prevents the contact of electrolyte with ZT film therefore we have less dark current. After $TiCl_4$ treatment the dark current does not change due to the recombination on the surface of the TiO_2. Thus indication reducing the surface defects is more important factor than blocking layer.

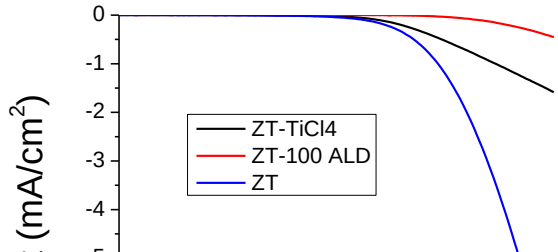

Figure 7. 8 Darkcurrent measurements of $TiCl_4$ treated and ALD coated ZT films.

7.4 Conclusions

$TiCl_4$ treatment reduces the surface defects reducing the recombination at the surface. ALD barrier layers prevent the recombination with the electrolyte. Thick ALD layers prevent electron injection, reducing the photocurrent and efficiency of DSSC. The recombination at the surface defect recombination centers is more compared to recombination with the electrolyte. $TiCl_4$ treated ZT films perform better than TiO_2 ALD ZT films. Combining both the ALD and $TiCl_4$ treatment can improve the efficiency much higher than individual treatments.

7.5 References

1. P. J. Cameron, L. M. Peter, and S. Hore, "How Important is the Back Reaction of Electrons via the Substrate in Dye-Sensitized Nanocrystalline Solar Cells?," *The Journal of Physical Chemistry B,* 109[2] 930-36 (2004).

2. L. Spiccia, U. Bach, A. Gupta, w. xiang, T. Daeneke, R. A. Evans, C. A. Ohlin, and I. R. Perera, "Introducing Manganese Complexes as Redox Mediators for Dye-sensitized Solar Cells," *Physical Chemistry Chemical Physics* (2013).

3. A. Yella, H.-W. Lee, H. N. Tsao, C. Yi, A. K. Chandiran, M. K. Nazeeruddin, E. W.-G. Diau, C.-Y. Yeh, S. M. Zakeeruddin, and M. Grätzel, "Porphyrin-Sensitized Solar Cells with Cobalt (II/III)–Based Redox Electrolyte Exceed 12 Percent Efficiency," *Science,* 334[6056] 629-34 (2011).

4. S. Ito, P. Liska, P. Comte, R. Charvet, P. Pechy, U. Bach, L. Schmidt-Mende, S. M. Zakeeruddin, A. Kay, M. K. Nazeeruddin, and M. Gratzel, "Control of dark current in photoelectrochemical (TiO_2/I^-/I_3^-) and dye-sensitized solar cells," *Chemical Communications*[34] 4351-53 (2005).

5. E. Guillén, E. Azaceta, A. Vega-Poot, J. Idígoras, J. Echeberría, J. A. Anta, and R. Tena-Zaera, "ZnO/ZnO Core–Shell Nanowire Array Electrodes: Blocking of Recombination and Impressive Enhancement of Photovoltage in Dye-Sensitized Solar Cells," *The Journal of Physical Chemistry C,* 117[26] 13365-73 (2013).

6. S.-J. Roh, R. S. Mane, S.-K. Min, W.-J. Lee, C. D. Lokhande, and S.-H. Han, "Achievement of 4.51% conversion efficiency using ZnO recombination barrier layer in TiO_2 based dye-sensitized solar cells," *Applied Physics Letters,* 89[25] - (2006).

7. E. Palomares, J. N. Clifford, S. A. Haque, T. Lutz, and J. R. Durrant, "Control of Charge Recombination Dynamics in Dye Sensitized Solar Cells by the Use of Conformally Deposited Metal Oxide Blocking Layers," *Journal of the American Chemical Society,* 125[2] 475-82 (2002).

8. T. C. Li, M. r. S. Góes, F. Fabregat-Santiago, J. Bisquert, P. R. Bueno, C. Prasittichai, J. T. Hupp, and T. J. Marks, "Surface Passivation of Nanoporous TiO_2 via Atomic Layer Deposition of ZrO_2 for Solid-State Dye-Sensitized Solar Cell Applications," *The Journal of Physical Chemistry C,* 113[42] 18385-90 (2009).

9. K. E. Roelofs, T. P. Brennan, J. C. Dominguez, C. D. Bailie, G. Y. Margulis, E. T. Hoke, M. D. McGehee, and S. F. Bent, "Effect of Al2O3 Recombination Barrier Layers Deposited by Atomic Layer Deposition in Solid-State CdS Quantum Dot-Sensitized Solar Cells," *The Journal of Physical Chemistry C,* 117[11] 5584-92 (2013).

10. A. Kay and M. Grätzel, "Dye-Sensitized Core−Shell Nanocrystals: Improved Efficiency of Mesoporous Tin Oxide Electrodes Coated with a Thin Layer of an Insulating Oxide," *Chemistry of Materials,* 14[7] 2930-35 (2002).

11. P. Docampo, P. Tiwana, N. Sakai, H. Miura, L. Herz, T. Murakami, and H. J. Snaith, "Unraveling the Function of an MgO Interlayer in Both Electrolyte and Solid-State SnO_2 Based Dye-Sensitized Solar Cells," *The Journal of Physical Chemistry C,* 116[43] 22840-46 (2012).

12. P. Ramasamy, M.-S. Kang, H.-J. Cha, and J. Kim, "Highly efficient dye-sensitized solar cells based on HfO_2 modified TiO_2 electrodes," *Materials Research Bulletin,* 48[1] 79-83 (2013).

13. M.-H. Kim and Y.-U. Kwon, "Semiconductor CdO as a Blocking Layer Material on DSSC Electrode: Mechanism and Application," *The Journal of Physical Chemistry C,* 113[39] 17176-82 (2009).

14. D. Jiang, Y. Hao, R. Shen, S. Ghazarian, A. Ramos, and F. Zhou, "Effective Blockage of the Interfacial Recombination Process at TiO_2 Nanowire Array Electrodes in Dye-Sensitized Solar Cells," *ACS Applied Materials & Interfaces,* 5[22] 11906-12 (2013).

15. B. Peng, G. Jungmann, C. Jäger, D. Haarer, H.-W. Schmidt, and M. Thelakkat, "Systematic investigation of the role of compact TiO_2 layer in solid state dye-sensitized TiO_2 solar cells," *Coordination Chemistry Reviews,* 248[13–14] 1479-89 (2004).

16. S. M. Waita, B. O. Aduda, J. M. Mwabora, G. A. Niklasson, C. G. Granqvist, and G. Boschloo, "Electrochemical characterization of TiO_2 blocking layers prepared by reactive DC magnetron sputtering," *Journal of Electroanalytical Chemistry,* 637[1–2] 79-83 (2009).

17. H. Yu, S. Zhang, H. Zhao, G. Will, and P. Liu, "An efficient and low-cost TiO_2 compact layer for performance improvement of dye-sensitized solar cells," *Electrochimica Acta,* 54[4] 1319-24 (2009).

18. M. Thelakkat, C. Schmitz, and H. W. Schmidt, "Fully Vapor-Deposited Thin-Layer Titanium Dioxide Solar Cells," *Advanced Materials,* 14[8] 577-81 (2002).

19. J. Guo, C. She, and T. Lian, "Effect of Insulating Oxide Overlayers on Electron Injection Dynamics in Dye-Sensitized Nanocrystalline Thin Films†," *The Journal of Physical Chemistry C,* 111[25] 8979-87 (2007).

20. A. K. Chandiran, A. Yella, M. Stefik, L.-P. Heiniger, P. Comte, M. K. Nazeeruddin, and M. Grätzel, "Low-Temperature Crystalline Titanium Dioxide by Atomic Layer Deposition for Dye-Sensitized Solar Cells," *ACS Applied Materials & Interfaces,* 5[8] 3487-93 (2013).

21. T. P. Brennan, J. R. Bakke, I. K. Ding, B. E. Hardin, W. H. Nguyen, R. Mondal, C. D. Bailie, G. Y. Margulis, E. T. Hoke, A. Sellinger, M. D. McGehee, and S. F. Bent, "The importance of dye chemistry and $TiCl_4$ surface treatment in the behavior of Al2O3 recombination barrier layers deposited by atomic layer deposition in solid-state dye-sensitized solar cells," *Physical Chemistry Chemical Physics,* 14[35] 12130-40 (2012).

22. V. Manthina, J. P. Correa Baena, G. Liu, and A. G. Agrios, "ZnO–TiO_2 Nanocomposite Films for High Light Harvesting Efficiency and Fast Electron Transport in Dye-Sensitized Solar Cells," *The Journal of Physical Chemistry C,* 116[45] 23864-70 (2012).

23. N. Sakai, T. Miyasaka, and T. N. Murakami, "Efficiency Enhancement of ZnO-Based Dye-Sensitized Solar Cells by Low-Temperature $TiCl_4$ Treatment and Dye Optimization," *The Journal of Physical Chemistry C,* 117[21] 10949-56 (2013).

24. H. S. Lee, C. S. Woo, B. K. Youn, S. Y. Kim, S. T. Oh, Y. E. Sung, and H. I. Lee, "Bandgap Modulation of TiO_2 and its Effect on the Activity in Photocatalytic Oxidation of 2-isopropyl-6-methyl-4-pyrimidinol," *Top Catal,* 35[3-4] 255-60 (2005).

25. A. K. Chandiran, N. Tetreault, R. Humphry-Baker, F. Kessler, E. Baranoff, C. Yi, M. K. Nazeeruddin, and M. Grätzel, "Subnanometer Ga2O3 Tunnelling Layer by Atomic Layer Deposition to Achieve 1.1 V Open-Circuit Potential in Dye-Sensitized Solar Cells," *Nano Letters,* 12[8] 3941-47 (2012).

26. J. Kim, H. Choi, C. Nahm, C. Kim, S. Nam, S. Kang, D.-R. Jung, J. I. Kim, J. Kang, and B. Park, "The role of a $TiCl_4$ treatment on the performance of CdS quantum-dot-sensitized solar cells," *Journal of Power Sources,* 220[0] 108-13 (2012).

27. S. Wendt, P. T. Sprunger, E. Lira, G. K. H. Madsen, Z. Li, J. Ø. Hansen, J. Matthiesen, A. Blekinge-Rasmussen, E. Lægsgaard, B. Hammer, and F. Besenbacher, "The Role of

Interstitial Sites in the Ti3d Defect State in the Band Gap of Titania," *Science,* 320[5884] 1755-59 (2008).

28. S. M. Prokes, J. L. Gole, X. Chen, C. Burda, and W. E. Carlos, "Defect-Related Optical Behavior in Surface Modified TiO_2 Nanostructures," *Advanced Functional Materials,* 15[1] 161-67 (2005).
29. F. J. Knorr, D. Zhang, and J. L. McHale, "Influence of $TiCl_4$ Treatment on Surface Defect Photoluminescence in Pure and Mixed-Phase Nanocrystalline TiO_2," *Langmuir,* 23[17] 8686-90 (2007).
30. H. O. Seo, S.-Y. Park, W. H. Shim, K.-D. Kim, K. H. Lee, M. Y. Jo, J. H. Kim, E. Lee, D.-W. Kim, Y. D. Kim, and D. C. Lim, "Ultrathin TiO_2 Films on ZnO Electron-Collecting Layers of Inverted Organic Solar Cell," *The Journal of Physical Chemistry C,* 115[43] 21517-20 (2011).
31. X.-s. Wang and X.-w. Guo, "Synthesis, characterization and catalytic properties of low cost titanium silicalite," *Catalysis Today,* 51[1] 177-86 (1999).
32. Z. Zhang, S. M. Zakeeruddin, B. C. O'Regan, R. Humphry-Baker, and M. Grätzel, "Influence of 4-Guanidinobutyric Acid as Coadsorbent in Reducing Recombination in Dye-Sensitized Solar Cells," *The Journal of Physical Chemistry B,* 109[46] 21818-24 (2005).

Chapter 8
Final Conclusions and Outlook

The work conducted during this thesis aimed at improving the DSSC using two different strategies: developing fast electron transport nanocomposites with high surface area and band edge engineering of the nanocomposites. As discussed in the respective chapters, valuable contributions have been made to fast electron transport field ; in brief:

ZnO-TiO_2 nanostructures- ZnO nanorods with density control have been synthesized and coated uniformly with TiO_2 nanoparticles. We demonstrated that these structures have fast electron transport when compared to conventional TiO_2 nanoparticulate films. We also found there is energy barrier between ZnO and TiO_2 for electron transport.

$Co_{0.1}Zn_{0.9}O$ nanorods - was synthesized with reduced conduction band edge for efficient electron transport. The long electron lifetime of $Co_{0.1}$ $Zn_{0.9}$ O nanorods gives better performance than pure ZnO nanorods in fast recombining Fc/Fc^+ electrolyte.

$Zr_{0.1}Ti_{0.9}O_2$- was synthesized with higher band gap than ZnO for efficient electron transport in the novel core-shell nanostructures. The optimizing of the dopant Zr content increased the performance of the DSSC.

Blocking Layers- were synthesized using the conventional $TiCl_4$ treatment and novel ALD deposition. $TiCl_4$ treated ZT films performed better than TiO_2 ALD deposited films due to reduction of the defects on the TiO_2 surface, decreasing the recombination centers on the surface of the TiO_2.

The defect related recombination is the dominant recombination when compared to semiconductor electrolyte interface recombination.

For the future development and commercialization of inexpensive and high efficiency DSSC, I see a large potential in the combined effort of these fields.

To conclude the fast electron transport core-shell nanostructures are synthesized using low cost large area applied techniques. I want to stress once more the knowledge one obtains from a comprehensive view of the DSSC on one side, and a detailed understanding of its device physics on the other side. Still, many aspects of the DSSC are not well understood. Nevertheless, the findings of this thesis, and the developed tools, pave the way for a systematic analysis and reduction of losses as well as a better fundamental understanding of the DSSC.

The core-shell nanostructures synthesized are applied to the field of LEDs and water splitting applications.

In the field of LEDs these core-shell nanostructures are applied to reduce the auger recombination causing the efficiency droop.

In water splitting the fast electron transport with larger surface area can improve the efficiency of water splitting.

COPY RIGHTS AND PERMISSIONS

Title: $ZnO–TiO_2$ Nanocomposite Films for High Light Harvesting Efficiency and Fast Electron Transport in Dye-Sensitized Solar Cells

Author: Venkata Manthina, Juan Pablo Correa Baena, Guangliang Liu, and Alexander G. Agrios

Publication: The Journal of Physical Chemistry C

Publisher: American Chemical Society

Date: Nov 1, 2012

PERMISSION/LICENSE IS GRANTED FOR YOUR ORDER AT NO CHARGE

This type of permission/license, instead of the standard Terms & Conditions, is sent to you because no fee is being charged for your order. Please note the following:

- Permission is granted for your request in both print and electronic formats, and translations.
- If figures and/or tables were requested, they may be adapted or used in part.
- Please print this page for your records and send a copy of it to your publisher/graduate school.
- Appropriate credit for the requested material should be given as follows: "Reprinted (adapted) with permission from (V. Manthina, J. P. Correa Baena, G. Liu, and A. G. Agrios, "$ZnO–TiO_2$ Nanocomposite Films for High Light Harvesting Efficiency and Fast Electron Transport in Dye-Sensitized Solar Cells," *The Journal of Physical Chemistry C,* 116[45] 23864-70 (2012)). Copyright (2012) American Chemical Society."
- One-time permission is granted only for the use specified in your request. No additional uses are granted (such as derivative works or other editions). For any other uses, please submit a new request.

Title:	Number Density and Diameter Control of Chemical Bath Deposition of ZnO Nanorods on FTO by Forced Hydrolysis of Seed Crystals
Author:	Venkata Manthina,Tulsi Patel,Alexander G. Agrios
Publication:	Journal of the American Ceramic Society
Publisher:	John Wiley and Sons
Date:	Jan 31, 2014

Order Completed

Thank you very much for your order.

This is a License Agreement between Venkata Manthina ("You") and John Wiley and Sons ("John Wiley and Sons"). The license consists of your order details, the terms and conditions provided by John Wiley and Sons, and the payment terms and conditions.

Get the printable license.

License Number	3319401459452
License date	Jan 31, 2014
Licensed content publisher	John Wiley and Sons
Licensed content publication	Journal of the American Ceramic Society
Licensed content title	Number Density and Diameter Control of Chemical Bath Deposition of ZnO Nanorods on FTO by Forced Hydrolysis of Seed Crystals
Licensed copyright line	© 2014 The American Ceramic Society
Licensed content author	Venkata Manthina,Tulsi Patel,Alexander G. Agrios
Licensed content date	Jan 31, 2014
Start page	n/a
End page	n/a
Type of use	Dissertation/Thesis
Requestor type	Author of this Wiley article
Format	Print and electronic
Portion	Full article
Will you be	No

translating?	
Title of your thesis / dissertation	Solution Processed Semiconductor Nanostructures and Nanocomposites for Dye-Sensitized Solar Cells
Expected completion date	Jan 2014
Expected size (number of pages)	164
Total	0.00 USD